NTNU
Norwegian University of
Science and Technology

Tapping of FeSi Furnaces

Hanne Mette Hustad

Chemical Engineering and Biotechnology
Submission date: June 2018
Supervisor: Merete Tangstad, IMA

Norwegian University of Science and Technology
Department of Materials Science and Engineering

Preface

This thesis investigates temperatures in the tapping area in ferrosilicon production and how it relates to furnace operations, tapping conditions, properties of FeSi, and slag and FeSi compositions. This thesis has been funded by the KPN project Controlled Tapping (267621). I gratefully acknowledge the financial support from the Research Council of Norway and the partners of the KPN Controlled Tapping.

I would like to thank my supervisor, Merete Tangstad, for giving me the opportunity to write this thesis that greatly increased my knowledge of ferrosilicon production which will come in handy in the future ahead. Secondly, I would like to thank Finnfjord AS for their cooperation and support during our visits to their plant in Finnfjordbotn. Thirdly, I would like to thank operator Steinar at Finnfjord AS that did all the measuring work and sampling under our guidance. His experience also gave valuable inputs during tapping sessions. Finally, I would like to thank my study hall buddies, Fatbardha and Martin, who have supported me through ups and downs during the last years here at NTNU.

Trondheim, June 2018
Hanne Mette Hustad

Summary

Ferrosilicon is usually produced in an electric arc furnace. During the tapping of the furnace solidification of FeSi and slag in the runner and ladle are a major issue because it lowers the ferrosilicon yield and causes hazardous situations for operators who cleans the runner for solidified materials. This study investigates how temperature in the runner and ladle is affected by furnace operations, conditions during tapping, properties of FeSi, and slag and FeSi compositions. This is done by measuring temperatures in the runner and ladle during tapping of FeSi in a ferrosilicon production plant, chemical analysis of FeSi and slag samples, and heat transfer modelling.

There were two campaigns at ferrosilicon producer Finnfjord AS that had the goal of measure temperatures in the runner and ladle during tapping sessions, and collecting FeSi and slag samples in a 19 MW furnace that tapped discontinuously. The temperature of FeSi in the runner was measured continuously with C-type thermocouples during some tapping session. Two K-type thermocouples were also embedded inside the runner in the last campaign, one close to the furnace and another close to the end of the runner, that measured the temperature in the runner continuously for the duration of the campaign. The temperatures in the ladle were point measured with both C-type thermocouples and S-type thermocouples. Point measurements with S type thermocouples were done every 5 minutes when conditions allowed it. FeSi samples where also collected every 5 minutes during the first tapping sessions when conditions allowed it. The frequency of the FeSi sampling was decreased to 1-3 samples per tapping sessions after that. Observations during tapping sessions were also noted, and operational data was collected and normalized.

FeSi samples were crushed and milled to fine FeSi powder. The powder was pressed to pellets and analyzed for chemical composition with X-ray fluorescence (XRF). The slag samples were cut, molded in epoxy, and polished. The slag samples were than analyzed for chemical composition with electron-dispersive spectroscopy (EDS) in a scanning electron microscope (SEM).

The heat transfer model calculated the temperature difference caused by heat convection and thermal radiation in the runner, when FeSi is in free fall between runner and ladle, and in the ladle during simulated tapping sessions. Heat capacity of FeSi, emissivity of FeSi, diameter of FeSi flow, and mass flow rate was chosen to vary over several cases run on the model.

Measurements with S-type thermocouples in the ladle showed that FeSi temperatures varied between 1650-1465°C throughout tapping sessions. The measurements can be characterized into four groups based on trends, events during tapping, and furnace operations. The temperature in the runner was measure to be around 1760-1920°C, and it was found that variations may depend on movements of the electrode closest to the tapping hole.

The estimation of heat transfer coefficient, h_c, used in the modeling varied greatly from 7.8 W/(m^2K) to 38 373 W/(m^2K). The reason for this can be assumptions made during calculations that requires a low heat transfer coefficient. The heat transfer coefficient calculated based on own measurements was used for further calculations. The model showed that the emissivity of FeSi plays a large part for the total heat loss during the simulated tapping sessions, but previous works suggests that emissivity of FeSi can be as low as 0.2. Slag on top of liquid metal, however, can increase the emissivity. It is possible that heat capacity of FeSi does not vary as greatly with temperature in reality, and it is therefore possible that the change of heat capacity with temperature does not play a large role in the total heat loss during tapping. It was also found through modelling that the velocity of metal flow may play a larger part in the total heat loss during tapping than the diameter of FeSi flow when the mass flow rate is held constant. The mass flow rate was also found to play a major role in supplying heat to the ladle during tapping.

It was found that aluminum and calcium impurities in the FeSi samples varied very little during a tapping session. It was also found that they do not correlate with neither ladle nor runner temperatures, which contradicts previous works. There were some trends suggesting that low ladle temperatures gives low concentrations of aluminum and calcium and high temperatures gives high concentrations. It was found that aluminum and calcium concentrations in FeSi depends on both temperature and added carbon materials in excess of the normal recipe.

Four slag samples were also collected after some tapping sessions and it was found that high viscosity slag with high amounts of silicon was found just around the tapping hole and stuck to the equipment used by operators. Low viscosity slag was found further down the runner, and it seems that only this type of slag can find its way down to the ladle. However, further studies are needed to fully understand the interaction between slag and FeSi during tapping of ferrosilicon furnaces.

Table of Contents

List of Tables

List of Figures

Chapter 1

Introduction

Ferrosilicon, or FeSi, is an alloy made out of iron and silicon. It is mostly used as deoxidization agent in steel-making where dissolved oxygen reacts with the dissolved silicon in the steel melt to form a silicon oxide slag, which is removed afterwards. FeSi can also be added to other ferroalloys to increase the alloys strength or magnetic properties. The most common compositions of produced ferrosilicon have 15 %, 45 %, 75 %, or 90 % silicon. The production process for FeSi is much the same as silicon, except that iron oxide is also added as a source for iron. FeSi is produced in an electric arc furnace where quartz (SiO_2) and iron oxides (Fe_xO_y) are reduced to silicon and iron respectively with different carbon materials as reducing agents. Liquid FeSi is then tapped either continuously or discontinuously at the bottom of the furnace from a runner and into a ladle. In this tapping process a lot of heat is lost from FeSi, which results in temperatures decreasing below freezing point, and frozen FeSi will accumulate in the runner and ladle. This can lower the mass flow rate and create hazardous situations for the operators, who have to remove the frozen FeSi. The production of FeSi is also considered a slag free process because of the high purity of the raw materials, but some minor amounts of slag is formed which either accumulates in the furnace or tapped together with FeSi. This slag can also freeze in the runner and ladle, and can contribute to the same problems mentioned earlier. More about the FeSi production process will be presented later in this chapter.

This study will investigate the temperatures around the tapping zone during tapping sessions in an electric arc furnace that produces ferrosilicon to see if there are any connections between temperature, aluminum and calcium content in the metal, furnace operations, and conditions during tapping. During two measuring campaigns at Finnfjord AS temperatures will be measured in the ladle, metal flow, and in the runner during tapping sessions at a 19 MW furnace. There will be used three different thermocouples for measuring the temperatures. Metal and slag samples will also be collected and analyzed for chemical composition. Modelling of temperature reduction in the runner and ladle will also be performed, and the results will be compared with that of the temperature measurements.

During tapping sessions between 1 and 6 metal samples will be collected and dip measurements of the temperature in the ladle with an S-type thermocouple will be performed. During some tapping session the temperature measurements in the metal flow will be taken together with ladle temperatures for comparison. The temperature will also be measured across the ladle to see if there are any temperature gradients within the ladle. C-type thermocouples will be used to measure the temperature of FeSi continuously in the runner and ladle during tapping sessions. Two K-type thermocouples will be embedded in the front and back of the runner, and will measure temperatures in the runner right underneath the FeSi flow.

A heat transfer model will be made to calculate heat transfer and temperature differences in the runner and ladle throughout simulated tapping sessions. The variables that will be investigated are emissivity of FeSi, heat capacity of FeSi, diameter of FeSi flow, and mass flow rate of FeSi. The results will be compared with the temperature measurements.

Metal samples will be analyzed for chemical composition with X-ray fluorescence (XRF). What is of most interest is the aluminum and calcium content in the samples and how it varies throughout tapping sessions, and if there are any correlations with the measured temperatures. Slag samples will also be collected and analyzed for chemical composition in a scanning electron microscope (SEM) with energy-dispersive X-ray spectroscopy (EDS).

Experiments will also be performed that will investigate how slag and FeSi behave during simulated tapping sessions. The experiments will be recorded with one of three cameras: Infrared camera, high speed camera, and a phone camera.

1.1 The ferrosilicon production in general

In this section the production process for ferrosilicon will be presented based on its description by Schei et al. (1998). The most common way of producing FeSi is in an electric arc furnace. Electric energy is fed to the process and creates an electric arc underneath each electrode which heats up the charge. It is around the electrodes that the temperature in the furnace will be at its highest, around 2000°C. The electrodes will adjust themselves to reach an optimal position above the FeSi melt and will produce heat, P, in watts according to

$$P = I^2 \cdot R, \tag{1.1}$$

where I is the electrical current in ampere and R is the electrical resistance of the charge in the furnace in ohms. A high electrical resistance of the raw material in the furnace is therefore desirable. The raw materials used are silicon oxide (SiO_2), iron oxide pellets (Fe_xO_y), and carbon reduction materials. Carbon is added to the process as a mix of different carbon materials such as coal, coke, char, charcoal and woodchips. The ratio between these carbon materials varies from producer to producer. FeSi is tapped at the bottom of the furnace and is then solidified, crushed and shipped. The off-gas contains mostly CO_2 and micro silica (SiO_2) where the latter is filtered out and sold as a by-product. The off-gas can also be treated for energy recovery. An overview of the production process can be seen in figure 1.1.

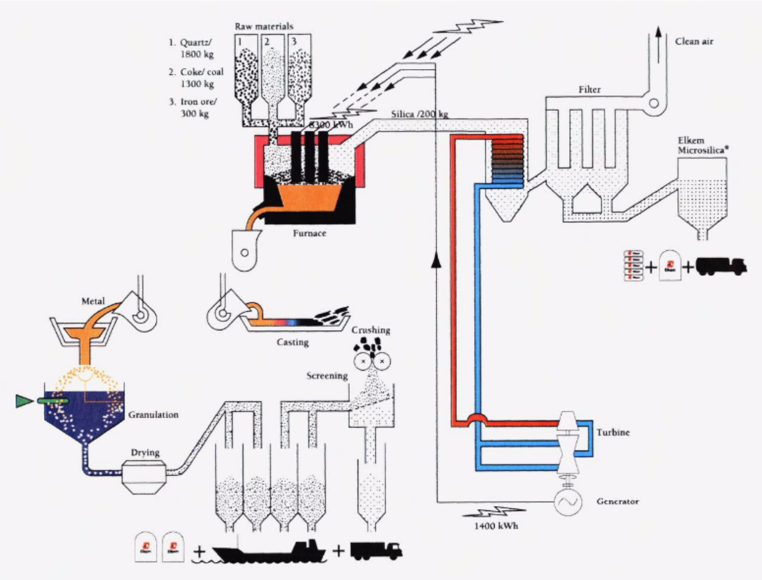

Figure 1.1: Overview of a typical ferrosilicon production process (Schei et al. (1998)).

The raw materials are fed to the furnace around the electrodes and SiO_2 is reduced at temperatures around 2000°C according to reaction equation 1.2. All enthalpy data has been calculated with HSC Chemistry 9.

$$SiO_2 + 2C = Si + 2CO(g) \qquad \Delta H^o_{2000} = 688kJ. \tag{1.2}$$

The reaction mechanism for producing silicon is more complex than what reaction equation 1.2 shows, and will involve the formation of the intermediate compound silicon carbide (SiC). The furnace can be divided into a low temperature zone and a high temperature zone where different reactions dominate. In the low temperature zone, where temperature ranges from 700-1300°C, formation of SiC and condensation of silicon oxide gas (SiO) take place:

$$SiO(g) + 2C = SiC + CO(g) \qquad \Delta H^o_{1300} = -75kJ, \tag{1.3}$$

$$2SiO(g) = SiO_2 + Si \qquad \Delta H^o_{1300} = -673kJ, \tag{1.4}$$

$$2SiO(g) + C = SiO_2 + SiC \qquad \Delta H^o_{1300} = -794kJ. \tag{1.5}$$

The formation of SiC in equation 1.3 is an intermediate step towards producing silicon, and as the SiC particles are formed they descend in the furnace toward the high temperature zone. The condensation reactions 1.4 and 1.5 are crucial for high silicon yield. The silicon yield is defined as silicon tapped over silicon added so it is important that as much SiO gas as possible is captured in the low temperature zone so it does not escape with the off-gas.

In the high temperature zone SiC particles reacts with SiO to form silicon according to reaction equation 1.6. The SiO gas formed here due to reaction 1.7 will flow upwards to the low temperature zone where it will react with carbon as stated earlier.

$$SiO(g) + SiC = 2Si(l) + CO(g) \qquad \Delta H^{o}_{2000} = 171kJ \tag{1.6}$$

$$SiO_2(l) + Si(l) = 2SiO(g) \qquad \Delta H^{o}_{1300} = 591kJ \tag{1.7}$$

In FeSi production reduction of iron oxides also takes place through several steps at temperatures ranging from 200 - 1200°C, which will be in the low temperature zone in the electric arc furnace. The iron oxide pellets mostly contain Fe_2O_3 so the overall reduction reaction is

$$Fe_2O_3 + 3CO(g) = 2Fe + 3CO_2 \qquad \Delta H^{o}_{1200} = -35kJ. \tag{1.8}$$

Liquid FeSi will be tapped at the bottom of the furnace through the runner and in to the ladle. Several problems arises in this part of the process because of solidification of FeSi and slag in the runner, but also because accumulation of SiC at the bottom of the furnace that can block the tapping hole. Blowing of SiO gas out of the tapping hole is also a reported problem because it creates hazardous situations and decreases FeSi yield.

Chapter 2

Theory

This chapter will present theory relevant to results and discussions. This includes basic theory and properties of thermocouples, which is relevant for temperature measurements of liquid metal. It will also include how aluminum and calcium ends up as impurities in FeSi, and the formation of slag in the furnace. Finally, theory about heat transfer mechanisms like conduction, convection and thermal radiation will be presented.

2.1 Basic theory and properties of thermocouples

This section will present basic theory and properties of thermocouples according to Pollock (1991). High temperature materials like liquid metals can be measured by the means of a thermocouple. A thermocouple in general is composed of two conductors where a small electric currents flows between the two when the junction between them experience a temperature difference. The electric energy that occurs is a function of temperature and can thus be a means for temperature measurement. The conductors, or thermoelements, can be metals, alloys, or semiconductors.

When measuring temperature one of the thermoelements is held at a constant reference temperature, which often is the melting point of ice (0°C), and is often called the reference junction. The other conductor is often called the measuring junction where the temperature is allowed to vary. The open-circuit voltage, also called emf, that occur because of the temperature difference is called the Seebeck voltages, which is the parameter that is actually measured during thermocouple temperature measurements. The relationship between the emf and temperature is not always linear so the given temperature differences does not yield a constant emf difference at different ranges of temperature. Because of that, the emf per degree of temperature, also called the relative Seebeck coefficient (RSC), is also not constant at different temperatures. Since RSC is not constant over all temperatures an absolute Seebeck coefficient (ASC) of a thermocouple is needed up to a temperature T in Kelvin, and it is given by

$$S = \oint_0^T \frac{\sigma}{T} dT \tag{2.1}$$

in a closed circuit. The term σ is in this case called the Thomson coefficient for a material, and is considered the specific heat of electricity because it determines the thermal energy change within the thermoelement per unit current flowing in it. For a thermocouple composed of thermoelements A and B the thermoelectric energy, E_{AB}, is given by the difference of the absolute thermoelectric energies of each of its components in a closed circuit:

$$\frac{dE_{AB}}{dT} = \oint_0^T \frac{\sigma_A}{T} dT - \oint_0^T \frac{\sigma_B}{T} dT. \tag{2.2}$$

However, standard thermocouples uses thermoelements that do have a near linear relationship between emf and temperature which makes calculations much easier. One of these standard thermocouples is the S-type which has a platinum reference junction and a platinum-rhodium alloy measuring junction. The ASC slope for standard thermocouple is constant, and is given by

$$\frac{dS}{dT} = -\frac{\pi^2 k_B^2}{6e(E_0 - E_F)}, \tag{2.3}$$

where k_B is the Boltzmann's constant which is 1.38 $\cdot 10^{-23}$ J/K, e is the charge of an electron which is 1.60 $\cdot 10^{-19}$ C, and $(E_0 - E_F)$ is the energy range of unoccupied holes in the d bands for the measuring junction and has a value of 1.0 eV for the S-type thermocouple. From this the ASC slope for the S-type is calculated to be -1.2 $\mu V/^{\circ}C$. The S-type thermocouple can measure temperature from -50°C up to the melting point of platinum at 1767°C.

Another standard thermocouple is the K-type which has a nickel-aluminum alloy reference junction and a nickel-chromium measuring junction. The K-type has also a near linear ASC slope at temperatures above 600°C so equation 2.3 can be applied, but with $(E_0 - E_F)$ at 0.8 eV. The ASC slope for the K-type thermocouple has been calculated to be -1.5 $\mu V/^{\circ}C$. Because the ASC starts to deviate from linearity at temperatures below 600°C the K-type thermocouple is most desirable to measure temperatures above 500°C. Below that the deviation becomes too large to neglect.

A non-standard thermocouple is the C-type which has a 95 at% Tungsten - 5 at% Rhenium measuring junction and a 74 at% Tungsten - 26 at% Rhenium reference junction. Tungsten-Rhenium thermocouples are used for very high temperature measurements to temperatures up to around 2315°C, but short-time measurments can be done up to 3000°C. Since the emf-temperature relationship is not linear for non-standard thermocouples the calculation of the ASC slope is complex and will not be shown here. However, the average ASC slope for the C-type thermocouple for temperatures between 0 and 2315°C was given by Pollock (1991) to be 16.0 $\mu V/°C$. Ceramic insulators around C-type thermocouples can reduce the maximum temperature of use. This is caused by conduction within the insulator which can decrease their electrical resistivity and the themoelement can be short-circuited.

The temperature range and use of thermocouples are often restricted by the melting point for the thermoelements, but also because of effects and phenomenons that occur at high temperatures. Because of this, it is always important that the instruction manual given by the manufacturer of the thermocouple is read and understood before temperature measurements can be started to avoid technical errors and to be certain that the results are as correct as they can be.

2.2 Aluminium and calsium impurities in FeSi metal

The oxide impurities present in raw materials in ferrosilicon production can either be reduced in the furnace to their metal components and end up in the metal phase, or stay as oxides and form a slag phase that is tapped together with the metal. The most abundant oxide impurities in ferrosilicon production is aluminum oxide (Al_2O_3) and calcium oxide (CaO), but other oxides like manganese oxides, titanium oxides, and magnesium oxide are also present in much minor amounts. This chapter, however, will focus on theory on how Al_2O_3 and CaO are reduced on how these reactions relate to temperature based on the work of Rosenqvist (2004).

The oxides ability to be reduced can be explained with an Ellingham diagram like the one showed in figure 2.1. An Ellingham diagram shows the standard Gibbs free energy (ΔG^0) as a function of temperature for different metal producing reactions. When a reaction is at equilibrium ΔG^0 equals zero and the reaction happens spontaneously. The reaction continue to be spontaneous when $\Delta G^0 < 0$, but is not at equilibrium. The ΔG^0 in the Ellingham diagram in figure 2.1 has been calculated with the following equation:

$$\Delta G^0 = \Delta H^0 - T\Delta S^0, \tag{2.4}$$

where ΔH^0 is the change of enthalpy for the reaction in J/mol, T is the temperature in K, and ΔS^0 is the change of entropy for the reaction in J/(Kmol). So from this it can be seen that the lower a reaction is in the Ellingham diagram the higher energy and temperature is required to reduce the oxide. This means that FeO will be reduced before SiO_2, which again will be reduced before Al_2O_3, and so on and so forth. For several of the curves in figure 2.1 a change in entropy can also be observed at different temperatures. This signals a phase change for the component and is either a melting point or a boiling point. At temperatures where there is a large change of entropy is often a boiling point, which is the case for Ca in figure 2.1.

For an oxide to be reduced with carbon the sum of the ΔG for the two reactions needs to be zero or less than zero. That happens at temperatures at and above the intersection point between the oxide curve and the carbon curve, and from figure 2.1 it is shown that is the case for FeO at around 720 °C, and for Al_2O_3 at around 2040 °C.

Because the Ellingham diagram is based on the standard Gibbs energy it is important to notice that it is only valid when all components are in their reference state, which is 100 % purity for each component. That is rarely the case in real life where both the metal phase and slag phase contains several different components in most metallurgical processes. In the ferrosilicon process impurities like Al_2O_3 and CaO are known to be present in FeSi even though very high temperatures are required to reduce them with carbon, but because of the presence of Al_2O_3-CaO-SiO_2 slags in the furnace also suggests that not all impurities in the raw materials are reduced.

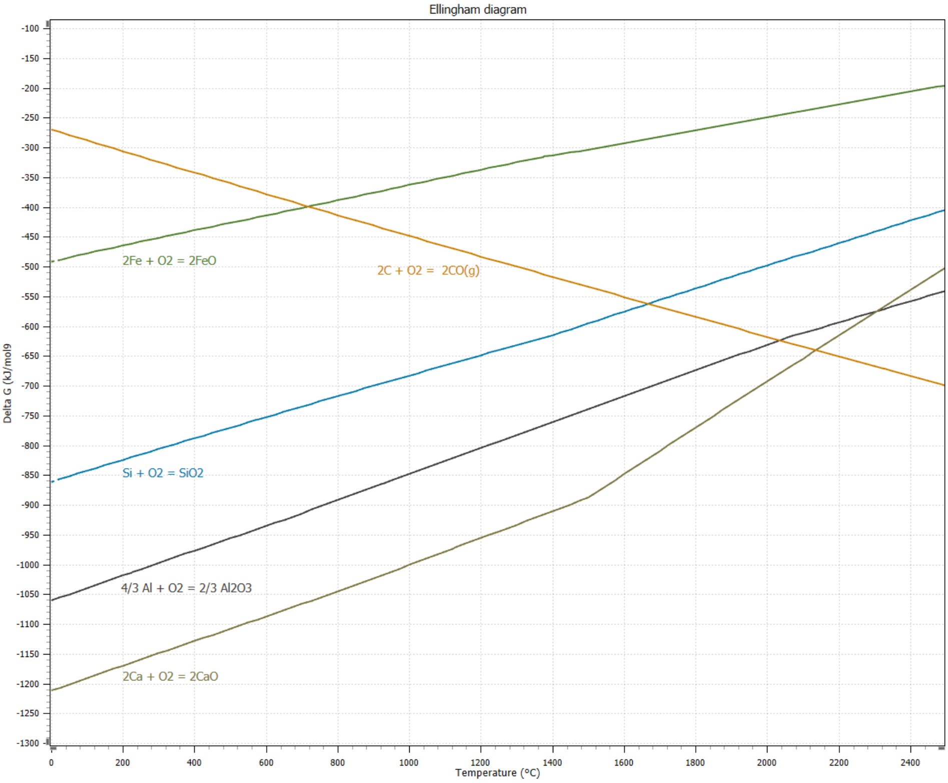

Figure 2.1: An Ellingham diagram that shows the relative stability of oxides. The Gibbs free energy is based on the reaction of 1 mole O_2 with the metal component for each oxide and has been calculated with HSC Chemistry 9.

From figure 2.1 it can be seen that Al_2O_3 and CaO are more stable oxides than SiO_2. It is therefore possible for aluminum and calcium metal to be oxidized by SiO_2 back to their respective oxides through the following reaction equations where the enthalpy and Gibbs free energy has been calculated with HSC Chemical 9:

$$Al + \frac{3}{4}SiO_2 = \frac{1}{2}Al_2O_3 + \frac{3}{4}Si \tag{2.5}$$

where $\Delta H(1500°C) = -262kJ$ and $\Delta G(1500°C) = -214kJ$ for equation 2.5, and

$$Ca + \frac{1}{2}SiO_2 = CaO + \frac{1}{2}Si \tag{2.6}$$

where $\Delta H(1500°C)$ = -342 kJ and $\Delta G(1500°C)$ = -292 kJ for equation 2.6. From the enthalpy and Gibbs free energy it is seen that both reactions are exothermic and spontaneous at 1500°C. The equilibrium constant for equation 2.5 and 2.6 is given as

$$K_{eq.2.5} = \frac{a_{Si}^{3/4} a_{Al_2O_3}^{1/2}}{a_{Al} a_{SiO_2}^{3/4}} \tag{2.7}$$

and

$$K_{eq.2.6} = \frac{a_{Si}^{1/2} a_{CaO}}{a_{Ca} a_{SiO_2}^{1/2}} \tag{2.8}$$

where a$_x$ is the activity for component x. The activity of component x equals the mass percentage of that component x times the activity coefficient for component x, γ_x. With that in mind equation 2.7 and 2.8 can be rewritten with respect to %Al and %Ca respectively:

$$\%Al = \frac{1}{K_{eq.2.5}} \cdot \frac{(\%Si \cdot \gamma_{Si})^{3/4}(\%Al_2O_3 \cdot \gamma_{Al_2O_3})^{1/2}}{\gamma_{Al}(\%SiO_2 \cdot \gamma_{SiO_2})^{3/4}} \tag{2.9}$$

and

$$\%Ca = \frac{1}{K_{eq.2.6}} \cdot \frac{(\%Si \cdot \gamma_{Si})^{1/2}(\%CaO \cdot \gamma_{CaO})}{\gamma_{Ca}(\%SiO_2 \cdot \gamma_{SiO_2})^{1/2}}. \tag{2.10}$$

From equation 2.9 and 2.10 we see that the concentration of aluminum and calcium in ferrosilicon depends on the composition of the metal phase and the slag phase as well as temperature. The last part is true because the equilibrium constant depends on temperature according to van 't Hoff equation which is stated to be

$$\frac{d}{d(1/T)} ln(K_{eq}) = \frac{-\Delta H^0}{R} \tag{2.11}$$

under standard conditions where R is the ideal gas constant given as 8.314 J/(Kmol). Furthermore, the activity coefficients also depends on the components in the phases and whether they are acidic or basic. In ideal solutions the activity coefficient equals 1 and the activity of a component equals the mass percentage of the component. In non-ideal solutions, however, the activity deviates from ideality when the activity coefficient is larger than 1 (positive deviation) or less than 1 (negative deviation). An example of that can be found in figure 2.2 where the activity of silicon in a Fe-Si system deviates negatively from an ideal solution. More about how the basicity of slag affects the activity of the components will be presented in the next chapter.

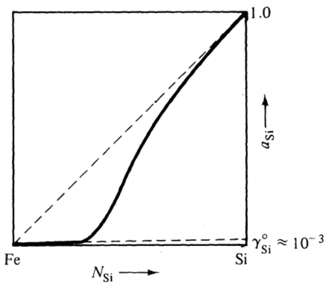

Figure 2.2: The ideal and non-ideal activity of silicon, γ_{Si}, as a function of %Si in a Fe-Si system (Rosenqvist (2004)).

Previous temperature measurements and FeSi analysis have been done by Hustad and Tangstad (2017). Ladle temperatures were measured and metal samples were collected to find correlations between aluminum and calcium content in FeSi and furnace operations. Figure 2.3 shows the general results from that study. From this figure it can be seen that there is no obvious correlation between ladle temperatures and aluminum/calcium content in FeSi, but figure 2.4 shows a good correlation between aluminum and calcium. Equation 2.9 and 2.10 shows that the concentration of aluminum and calcium should correlate with temperature, and since aluminum and calcium correlates with each other also suggests that this is actually the case. This is because the concentration of silicon in FeSi was found in this study to be very stable through time. This leaves only the slag composition and temperature to vary causing different aluminum and calcium concentrations.

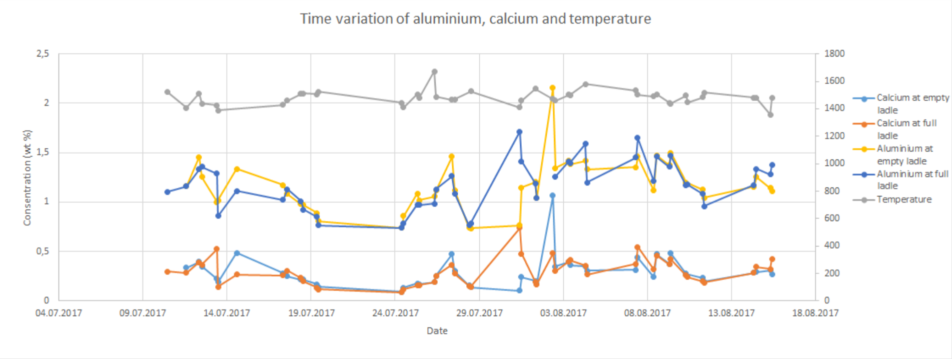

Figure 2.3: The variation of temperature, calcium, and aluminum content over time (Hustad and Tangstad (2017)).

The study concluded that there were no correlations between the temperature in the ladle and the calcium and aluminum content in FeSi, but there were a good correlation between aluminum and calcium content as figure 2.4 shows. From that it was concluded that the temperature measured in the ladle was not representative for the temperature in the furnace where metal producing reactions take place.

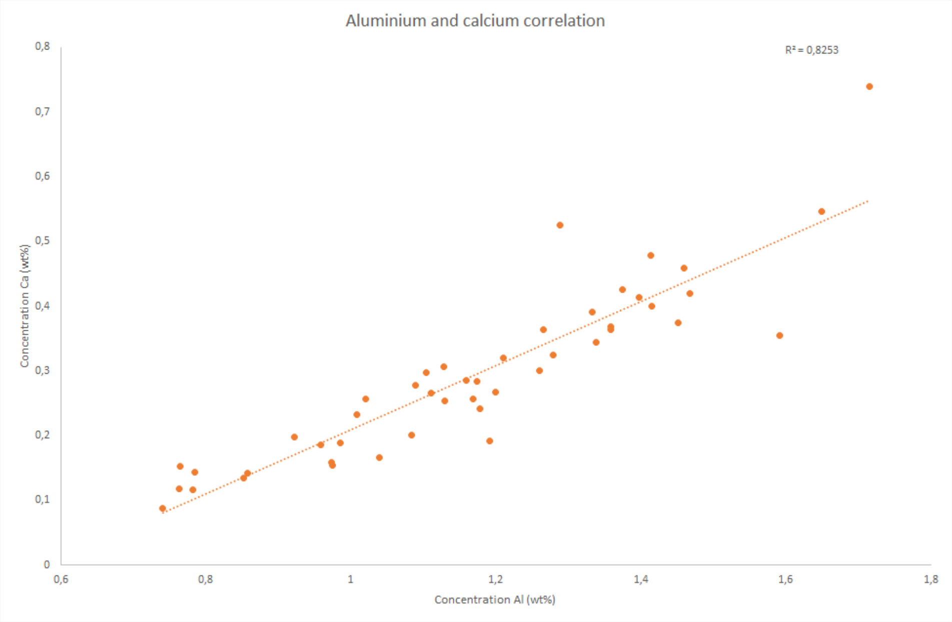

Figure 2.4: The correlation found between aluminum and calcium content in FeSi metal samples (Hustad and Tangstad (2017)).

2.3 The Al_2O_3-CaO-SiO_2 slag system

As mentioned earlier, the ferrosilicon production process is considered a slag free process because of the high purity of the raw materials. However, some slag is formed because of oxide impurities that is not reduced in the furnace, and will either accumulates in the furnace or get tapped together with ferrosilicon. The most abundant oxide impurities are aluminum oxide (Al_2O_3) and calcium oxide (CaO) which forms a slag phase together with SiO_2. This will create a Al_2O_3-CaO-SiO_2 slag system, and this chapter will present how its properties changes with composition based on the work done by VDEh (1981) and Schei et al. (1998).

The Al_2O_3-CaO-SiO_2 slag system can be described by the phase diagram in figure 2.5. The diagram shows a 2D projection of the liquidus surface where the thick solid lines represents the different phases in the system and the lighter lines represents liquidus isotherms. The straight lines in the diagram represents phases that can co-exist together as solids.

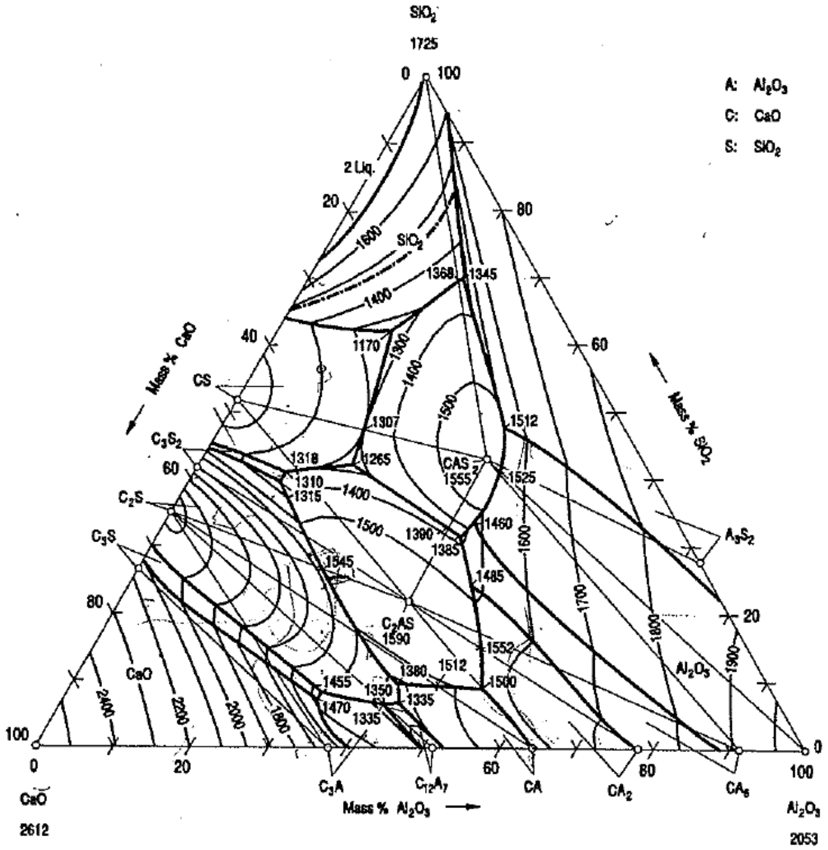

Figure 2.5: The phase diagram for the Al_2O_3-CaO-SiO_2 slag system (VDEh (1981)).

Since metal in silicon and ferrosilicon production is tapped at around 1500 °C it would be useful to know what slag compositions can be in liquid state at that temperature. In the left phase diagram in figure 2.6 the liquidus area at 1500 °C is marked with red lines and shows that every slag composition within that area is in liquid state at that temperature. Chemical analysis of slags from 65FeSi production used in the work of Yefimets et al. (2015) shows that most of the slag compositions fall in the liquidus area with highest SiO_2 content.

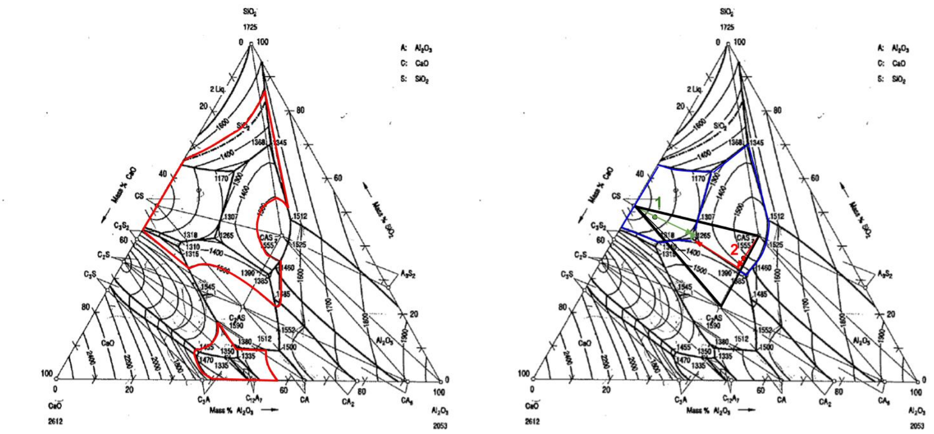

Figure 2.6: In the left phase diagram the liquidus area at 1500°C is marked with red lines. In the right phase diagram the crystallization paths for two slag compositions are marked with red and green arrows, and their primary crystallization fields are marked with blue lines.

Liquid slag in a system do not melt all at once at a specific temperature. It is therefore misleading to refer to a melting point of a slag composition, but rather a liquidus point where at that point all the slag in a system is in a liquid state. This is better shown by the crystallization paths in the right phase diagram in figure 2.6. Here two slag compositions are marked with green and red dots and their primary crystallization fields shown with blue lines. Slag composition 1 is within the CS primary crystallization field, so the first solid that will precipitate as the slag cools down is CS. As temperature decreases to the point where it hits the boundary line between CAS_2 and CS, CAS_2 will start to precipitate. As temperature decreases to eutectic temperature the rest of the liquid slag will solidify with the original composition given by point 1. For slag composition 2 CAS_2 will first precipitate, and then C_2AS before it finally solidifies with composition given by point 2. The liquidus temperature for slag 1 and 2 in this example is 1450 °C and 1490 °C respectively.

Properties of different slag melts are often better described by the slags basicity. Basicity is a concept that describes the ratio between basic and acidic oxides in a slag melt. For an Al_2O_3-CaO-SiO_2 melt CaO is considered a basic oxide and will form Ca^{2+} ions in a slag melt. SiO_2 is considered an acidic oxide and will form networks with SiO_4^- ions. Al_2O_3 can act both as an acidic and basic oxide and can be present in a slag melt as either Al^{3+} or AlO_3^{3-}, but in an Al_2O_3-CaO-SiO_2 melt it can be considered as an acidic oxide. The basicity can thus be defined as

$$B = \frac{\%CaO}{\%SiO_2 + \%Al_2O_3}. \tag{2.12}$$

The viscosity is one of the properties better explained by basicity. As mentioned previously SiO_4^- ions will form networks or chains in a slag melt, which will increase the viscosity.

Basic oxides like CaO that forms cations will break down these network and decrease the viscosity of the melt. It is important to note that this is the case for a completely melted slag, because any presence of solid particles in a slag melt will increase the viscosity considerably.

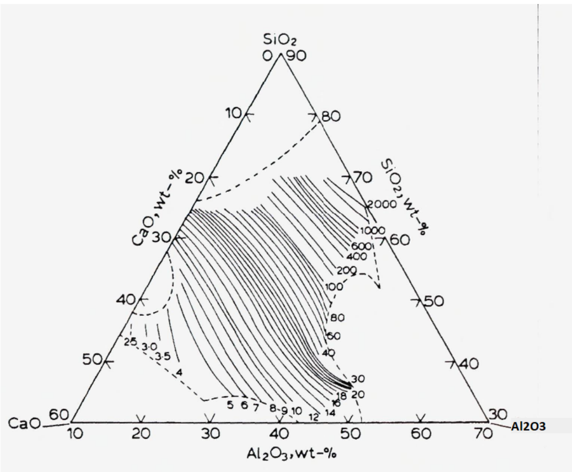

Figure 2.7: Viscosity lines for liquid Al_2O_3-CaO-SiO_2 slags at 1500°C (Schei et al. (1998)).

The viscosity for different Al_2O_3-CaO-SiO_2 slag melts at 1500°C is shown in figure 2.7. The most notable about the viscosity is that the contours are nearly parallel to constant basicity and it increases rapidly when the basicity is below 0.15. A more recent study by Zhang and Chou (2013) also shows that the viscosity of Al_2O_3-CaO-SiO_2 melts increases with increased Al_2O_3/SiO_2 ratio, but decreases at even higher Al_2O_3/SiO_2 ratios. This is due to the fact that more weaker Al-O bonds form in the Si-O network and will play a significant role for the viscosity of the melt. In this study it was also found out that viscosity decreases with increased temperature, which is consistent with literature theory where its is suggested that viscosity is dependent on temperature according to an Arrhenius type equation,

$$\eta = \eta_0 exp(\frac{E_\eta}{RT}), \tag{2.13}$$

where η_0 is a coefficient, E_η is the activation energy for viscous flow, R is the universal gas constant, and T is temperature.

Densities of the slag is an important property that determines if liquid metals will float on top of the slag or sink to the bottom. Since Al_2O_3-CaO-SiO_2 slags is less dense than ferrosilicon it has a tendency to float on top. The density of the slag depends on temperature of the slag melt and constituents like SiC present in the slag. Densities for different Al_2O_3-CaO-SiO_2 slag systems can be found in figure 2.8.

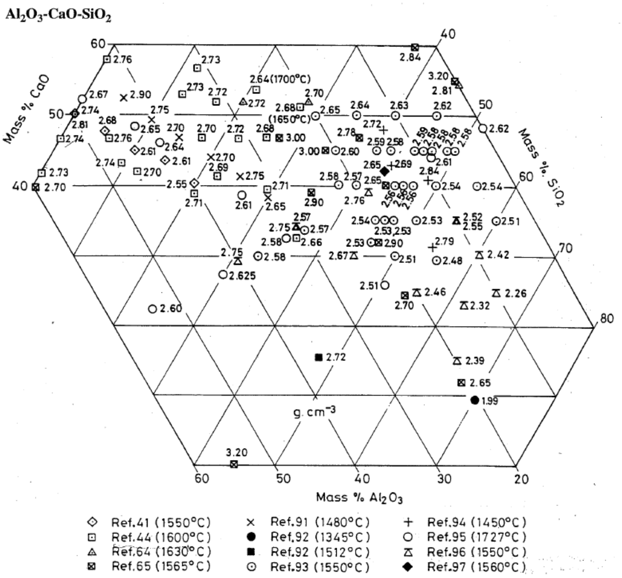

Figure 2.8: Densities in gcm^{-1} for different Al_2O_3-CaO-SiO_2 slag compositions at different temperatures (VDEh (1981)).

The work of McGrath et al. (2014) shows that the density of Al_2O_3-CaO-SiO_2 slags increases with increased CaO content and increases very slightly with temperature. It was also found a decrease in density with decrease in Al_2O_3 content. That is consistent with data found in figure 2.8 where densities ranges from 2.6 to 3.2 gcm^{-1}.

2.4 Heat transfer

Energy can be transferred between solids and fluids through three different mechanisms: conduction, convection, and thermal radiation. Thermal conduction is the heat transfer within a body of material without displacement of its particles. Convective heat transfer is the mechanism where heat is transferred through the movement of fluids. Thermal radiation is the kind of radiation that any matter emits if it posses a temperature above absolute zero. In the next three sections each of these heat transfer mechanisms will be elaborated according to Schuhmann (1952).

2.4.1 Conduction

Conduction in both solid and fluids occurs because of the transmission of kinetic energy from particle to particle within a body. This transfer of kinetic energy happens because molecules collide or generally interact with one another. The basic principle of heat conduction is stated by Fourier: *the rate of heat flow across a unit of surface is proportional to the temperature gradient perpendicular to the surface*. This statement can mathematically be stated as

$$q = -kA\frac{dT}{ds}, \tag{2.14}$$

where q is the rate of heat flow in J/s, k is the thermal conductivity of the material in W/(mK) and A is the area perpendicular to the heat flow in m^2. The expression dT/ds is the temperature gradient at a distance from plane A in the direction of the heat flow. It is important to know that equation 2.14 only applies for steady heat flow where the temperature gradient does not vary with time. For unsteady heat flow the temperature varies with time, and equation 2.14 can grow to be much more complex. Unsteady heat flow will not be discussed in this chapter.

To put Fouriers law to use in more practical systems equation 2.14 needs to be integrated. The solution will depend on the geometry of the system and the thermal conductivity of the material that is conducting the heat. For simple heat conduction system the heat flow q does not vary with either time or position s and is therefore constant. The integral form of equation 2.14 from position 1 to position 2 can be expressed as

$$q\int_{s_1}^{s_2}\frac{ds}{A} = -\int_{T_1}^{T_2} kdT. \tag{2.15}$$

If A is constant between position 1 and position 2, and k has a linear relationship with temperature the heat flow q can be expressed like

$$q = -k_{av}A\frac{\Delta T}{\Delta s}, \tag{2.16}$$

where ΔT is the temperature difference on surfaces at position 1 and position 2, Δs is the distance between position 1 and 2, and k_{av} is the average thermal conductivity of the conducting material. Thermal conductivity of materials can vary greatly from metals to insulating materials used in many areas in metallurgical industries. Thermal conductivities can also vary greatly with temperature, which must be taken in to account when calculating conduction heat flow. The relationship between k and T is often linear, so an average thermal conductivity, k_{av} can be used if the temperature range is known. In process metallurgy accurate values for thermal conductivity for liquid metals is particularly hard to find, but a selection of thermal conductivities of liquid metals at melting point can be found in Brandes et al. (1999). For silicon thermal conductivity from 0-100°C is 138.5 W/(mK) while for a typical refractory material the thermal conductivity has been found by Shimizu et al. (2013) to be 3.98 W/(mK). For fluids in general other heat transfer mechanisms like convection and thermal radiation is more dominant than conduction, so heat flow by conduction can often be neglected in these systems.

2.4.2 Convection

The movements of fluids carries heat with it as it flows, resulting in a convective heat transfer. The most common system of convection is natural convection where the motion of the fluid is caused by a difference in temperature. An example of that is hot air that rises up in a room and replaces the cool air which sinks to the bottom. The opposite of natural convection is forced convection where the movement of the fluid is produced in other ways than natural convection, like pumps or agitators. The natural convection heat transfer mechanism is the system that will be discussed in this section.

In process metallurgy it is of most interest to calculate the heat flow between the liquid metal and the surface that contains it, rather then calculating the heat flow within the liquid metal itself. In most cases it is often assumed that the temperature in the liquid metal is homogeneous because of the high amount of natural convection that occurs at these temperatures. The transfer of heat from a hot fluid to a cold surface happens through a thin layer of fluid near the solid surface called a stagnant layer with thickness Δs. The heat flow through this stagnant layer is mainly conduction where equation 2.16 comes in to play. The only problem is to define and determine the thickness of Δs. It is therefore of greater intent to rather use the following empirical relation for heat flow q from a hot fluid to a cold surface:

$$q = h_c A \Delta T, \tag{2.17}$$

Where A is the area where the hot liquid and the cold surface is in contact with one another and ΔT is the difference in temperature of the two. The coefficient h_c is called the convection heat transfer coefficient with unit W/(m^{2}K) and is inversely proportionate to Δs. The heat transfer coefficient is often found through empirical data, but several empirical equations also exist for estimating h_c for different systems. These equations are based on Nusselt, Prandtl, and Grashof dimensionless number. For a natural convection system where heat transfers from a hot liquid to a horizontal cylinder the estimation of h_c is

$$\frac{h_c D}{k} = \alpha \left[\left(\frac{c_p \mu}{k} \right) \left(\frac{D^3 \rho^2 \beta g \Delta T}{\mu^2} \right) \right]^{0.25}, \tag{2.18}$$

where c_p is the heat capacity of the fluid in J/(kgK), μ is the viscosity of the fluid in Pa/s, D is the diameter of the cylinder in meters, ρ is the density of the fluid in kg/m^3, and β is the thermal expansion coefficient of the fluid in 1/K. The factor α is in this case 0.53. Another estimation of h_c, which is a simplification of equation 2.18, is

$$h_c = C'(\Delta T)^{0.25}, \tag{2.19}$$

where C'= 0.38 for horizontal plates facing upwards, C'= 0.2 for horizontal plates facing downwards, and C'= 0.27 for vertical plates. To use equation 2.19 with these values for C' ΔT must be in fahrenheit, and the unit for h_c will be $Btu/hr - ft^2 -^o F$. For most natural convection problems encountered in metallurgical furnaces equation 2.19 will suffice in estimating h_c.

2.4.3 Radiation

The most important form of radiation when it comes to transfer of heat energy is the kind with wavelengths just beyond that of visible light. This is called infrared radiation. Like most kind of radiation infrared radiation can be blocked or travel through different kinds of materials. Refractory materials and liquid metal is opaque and can block infrared radiation, while gases are relatively transparent. The heat transfer rate through infrared radiation increases with the fourth power of the absolute temperature of the surface, so it is safe to say that heat transfer through radiation is greater than other heat transfer mechanisms at higher temperatures.

The ideal emitter and absorber of radiation is a black body, which absorbs all incident radiation. There are no absolute of black bodies found in the real world, but one approximate example is an isothermal enclosure with a small opening. The total radiated power per sqaure meter emitted by a black surface can be calculated by using Stefan-Boltzmann's law, that is

$$E_b = \sigma T^4. \tag{2.20}$$

The Stefan-Boltzmann constant σ has the value of $5.67 \cdot 10^{-8}\ W/m^2$ and the temperature T is in Kelvin. In the real world, however, equation 2.20 will not be the case. Real surfaces will always emit and absorb less energy than that of a black body at the same temperature. A new factor called emissivity ε needs to be introduced:

$$E = \varepsilon E_b. \tag{2.21}$$

Surfaces that has the total radiated power equal to equation 2.21 is called a grey body if it is assumed that ε has a value between 0 and 1 and is constant over all wavelengths. This is not entirely true either in the real world, but the data that is needed for rigorous calculations of emissivity over a range of wavelengths are not always available. For engineering calculations, however, it is common to assume grey-body behaviour and use a single estimated value for emissivity. For liquid silicon at melting point the emissivity has been reported by Takasuka et al. (1997) to be 0.25. The emissivity of steel has been found by Goett et al. (2013) to be around 0.2, but it was also found that slag present on the surface can increase the emissivity up to 0.35 at the same temperature.

2.4.4 The effect of change in heat content with temperature

In the previous sections different mechanisms for heat transfer have been discussed, but in this section it will be discussed how the change of heat content in a system will effect the temperature of that system. When the heat content in a system increases or decreases the change in temperature is heavily dependent of the heat capacity of the system, which is defined as the partial derivative of enthalpy with respect to temperature with constant pressure p:

$$C_p = \left(\frac{\partial H}{\partial T}\right)_p \tag{2.22}$$

with J/(mol K) as the units for C_p. Heat capacity itself is heavily dependent on temperature and has the following empirical relation:

$$C_p = a + 2bT - cT^{-2}. \tag{2.23}$$

The values of the empirical constants a, b, and c for many substances can be found in several reference books or programs like HSC Chemical 9. It is more common in engineering calculations to calculate the change in temperature or change in heat content per unit weight. The solution of the integrated form of equation 2.22 with respect to the mass of the system is

$$C_p = \frac{Q}{m\Delta T} \tag{2.24}$$

where C_p is the heat capacity of the substance in J/(kgK), Q is the amount of heat energy that enters the system in J, m is the mass of the system in kg, and ΔT is the change of temperature in the system. If Q is known by calculating heat transfer as discussed in previous sections then ΔT can be calculated.

Chapter 3

Experimental

In this chapter the instruments and methods for measuring temperatures around the tapping zone will be presented. Methods for collecting and analyzing FeSi samples will also be presented. Finally, the heat transfer modelling procedure will be disclosed. All temperature measurements, FeSi, and slag sampling was done by operators under guidance.

3.1 Temperature measurements

In this chapter the instruments and method for measuring temperatures around the tapping zone at the two campaigns at Finnfjord AS will be presented.

3.1.1 Instruments

Three different thermocouples were used to measure temperatures around the tapping area during the two campaigns. The temperature in the ladle was measured using the temperature measurement instrument Digilance IV with S-type disposable thermocouples. A sketch of the instrument can be seen in figure 3.1. The temperature in the runner was measured with a C-type thermocouple that was assembled according to figure 3.2. Two K-type thermocouples were also embedded in the runner that measured the temperature continuously from underneath the metal flow.

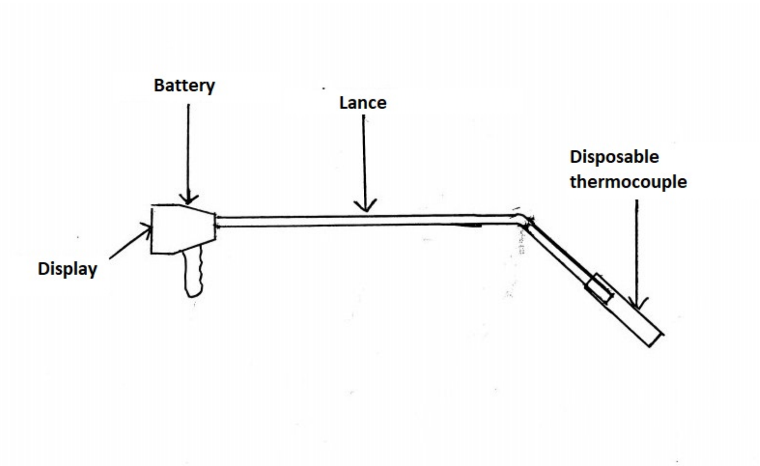

Figure 3.1: A sketch of the temperature measurement instrument Digilance IV that was used to measure temperatures in the ladle.

The S-type thermocouple is a platinum/rhodium alloy with 90 wt% platinum and 10 wt% rhodium and can measure temperatures up to 1767°C. The Digilance IV instrument, which the S-type thermocouple is mounted on, measures a temperature plateau and displays the maximum temperature at that point in time. The duration of the measurement is around 5 seconds. If the instrument is not held steady or the thermocouple breaks before reaching the temperature plateau error messages shows up on the display and a new measurements must be taken.

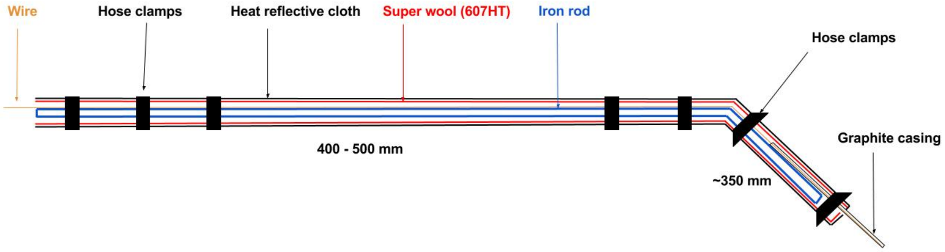

Figure 3.2: An illustration of the thermocouple used to measure the temperature in the runner.

The C-type thermocouple is a tungsten/rhenium alloy with 95 wt% tungsten and 5 wt% rhenium and can measure temperatures up to 2329°C. Due to the distance to the runner and the hot conditions the thermocouple was laid alongside an iron rod wrapped with super wool and heat reflective cloth according to figure 3.2. This was held together with hose clamps. The end of the wire was protected with a graphite casing that could be dipped in the metal bath. The C-type thermocouples that were used measured temperatures continuously.

The K-type thermocouple is a nickel alloy and can measure temperatures above $500^o C$. The two K-type thermocouples that were used were connected to a battery driven datalogger.

3.1.2 Methods

Measurements were done on a 18 MW furnace at Finnfjord AS during two campaigns. The furnace is tapped discontinuously, so different measurements were done at a total of 20 tapping sessions. Temperatures in the runner and ladle were measured using K-type, C-type and S-type thermocouples. Dip measurements in the ladle was performed by using C-type thermocouples and the temperature measurement instrument Digilance IV with S-type disposable thermocouples. The temperature in the runner was measured using K-type and C-type thermocouples. The application of the different thermocouples is illustrated in figure 3.3.

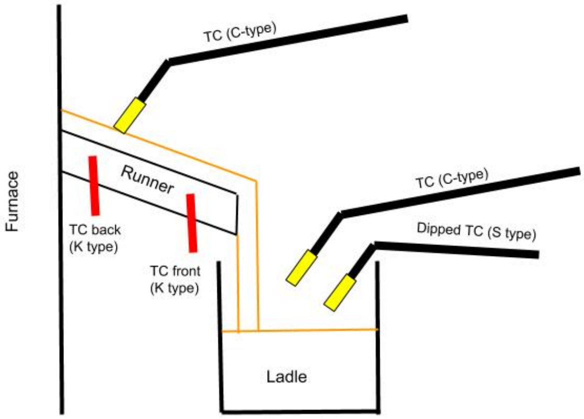

Figure 3.3: A sketch of the set-up that shows where the different thermocouples were used.

During tapping sessions both FeSi samples and temperature measurements with S-type thermocouples were taken with a 5 minutes interval when conditions allowed it. During some sessions the temperatures in the ladle and the FeSi flow were measured consecutively. Figure 3.4 shows the measurement positions in the ladle. Five measurements across the diameter of the ladle were also taken during one session with S-type thermocouples to investigate if there were temperature gradients in the ladle.

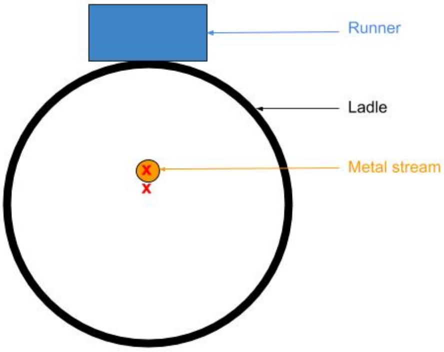

Figure 3.4: An illustration of the ladle. The positions of the temperature measurements are marked with red ”x”.

C-type thermocouples were used to measure the temperature in the runner during tapping sessions. The thermocouples measured continuously for 2 to 20 minutes before it either broke or had to be moved. A picture of the set-up can be found in figure 3.5. The C-type thermocouples were also used to measure the temperature in the ladle at some tapping sessions to compare with measurements done with the S-type thermocouple.

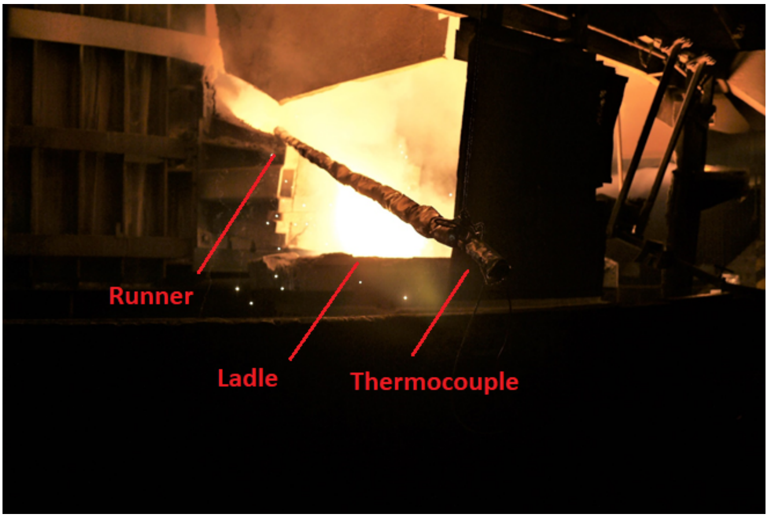

Figure 3.5: The setup for measuring the temperature in the runner with C-type thermocouples.

Two K-type thermocouples were embedded in the runner and measured continuously from underneath the FeSi flow during the last campaign.

3.2 FeSi and slag sample analysis

During the measuring campaign several FeSi and slag samples were collected, and this section will present the instruments and methods used to analyze these for chemical composition.

3.2.1 Instruments

The chemical composition of FeSi samples was found by the use of X-ray fluorescence (XRF). This chapter will present a short description on how XRF machines work according to Beckhoff et al. (2006). When an atom is bombarded with energetic X-rays one or several electrons in the inner orbitals can be ejected causing the atom to be ionized. This will cause electrons in higher orbitals to ”fall down” in the empty space and release a secondary, or fluorescence, X-rays for the atom. These X-rays are characteristic for each element and can be used to identify elements in a sample. An X-ray machine that can use this to identify and quantify elements in sample contains an X-ray source and an X-ray detector. The X-ray source is contained in a tube as the one shown in figure 3.6. The X-ray tube contains a cathode and an anode where electrons are emitted from the cathode and accelerated to the anode through an electric field. Different scattering processes will occur on the anode and X-rays are emitted in all directions from it, but will only emerge from a special exit window. The cathode is a heated filament, usually tungsten, and the anode is a elemental metal, usually chromium, copper, or molybdenum. The X-ray exits the tube and hits the sample, and a fluorescence X-ray will be emitted from the sample. The fluorescence X-ray will be detected by an X-ray detector which converts the released energy to electrical energy. The energy is measured and the elements in the sample are identified.

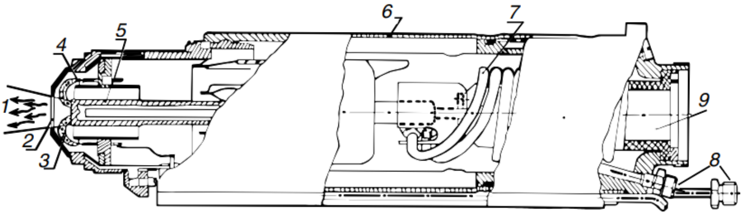

1. X-ray beam, 2 Be-window, 3 Electron beam, 4 Ring cathode, 5 Anode, 6 Tube housing assembly, 7 Insulating tube for cooling, 8 Cooling connections, 9 High-voltage connections

Figure 3.6: A typical design for an X-ray tube used for fluorescence analysis (Beckhoff et al. (2006)).

The chemical composition of the slag samples was found by using a energy-dispersive X-ray spectroscopy (EDS) detector on a scanning electron microscope (SEM). The SEM used in this study was of the field emission type by the name of FESEM Zeiss Ultra and is illustrated in figure 3.7. In SEM electrons from an electron source is accelerated towards the sample through a potential field that varies between 1-40 kV. When the electrons hit the sample secondary electrons will be scattered from the sample. These electrons are collected by a secondary electron detector and are used to create an image of the surface.

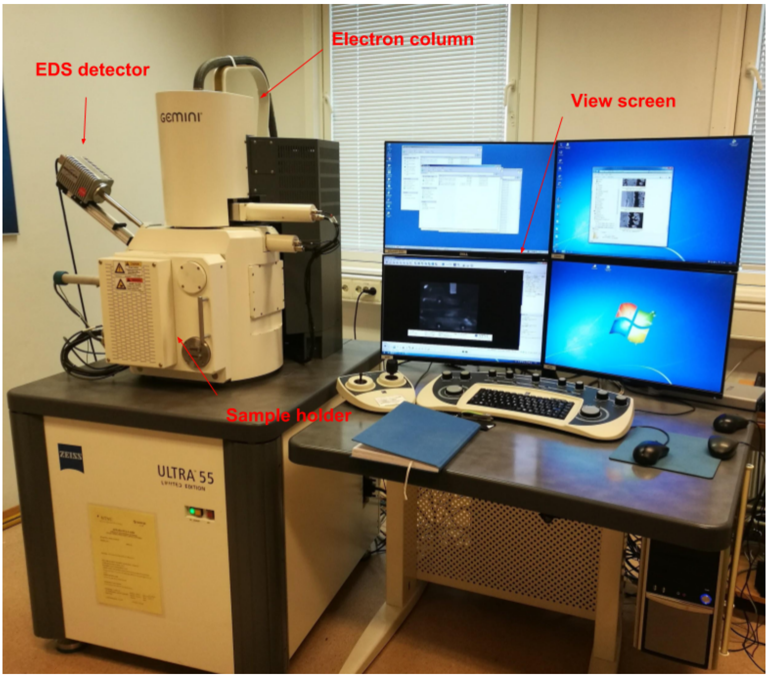

3.5

Figure 3.7: The FESEM Zeiss Ultra 55V at the Department of Material Science and Engineering, NTNU.

Electrons from the primary beam can also be backscattered from the surface. SEM can be mounted with a backscatter detector that detects the backscattered electrons. In backscatter mode the contrast on the sample surface will be caused by different average molecular weight or different crystallographic orientations. It can be used to identify areas on the sample that have different molecular weight, like slag and FeSi. The elemental analyses with EDS uses the same principle as the XRF. The way of acquiring a quantitative analysis from the X-ray spectroscope varies from manufacturer to manufacturer. In general, EDS quantitative analysis is a fast way of requiring chemical composition of a sample, but it is not highly accurate as standard deviations usually lies around +/- 5 %. (Hjelen (1986))

3.2.2 Methods

Several FeSi samples were taken over 17 tapping session and analyzed for chemical composition with X-ray fluorescence (XRF). For each tapping session 1-6 samples were collected directly from FeSi flow. Each sample was first crushed to around 1 cm grains, then milled for 2 minutes to create fine grained powder. Fine grained sample (12 g) and wax (3 g) was mixed and pressed to a cylindrical pellet with 4 cm in diameter. The pellets were then mounted in the XRF machine and analyzed for chemical compositions.

Slag samples were mainly collected from the runner, but some samples were also collected from tools used by the operator to clean the runner. The samples were analyzed for chemical composition with EDS in SEM. Preparation methods for samples that are to be analyzed with EDS is considered less comprehensive compared to other microscope sample preparations. The requirements are that the samples must be completely flat, electronically conductive, and free of surface contamination. The samples were cut, molded with epoxy, and polished to attain a smooth and flat surface. The samples were also coated with graphite to make the surface electronically conductive. The addition of a graphite layer on the sample surface will affect the EDS analysis, as it will show a increased amount of carbon on the sample.

Table 3.1: The settings used in SEM for viewing and analyzing the slag samples in backscatter mode.

Aperture	60 μm
Acceleration voltage	15 kV
Working distance	10 mm

Table 3.1 shows the settings used when viewing the sample surface in backscatter mode and analyzing the surface with EDS. During the analysis of the sample surface the main slag matrix was identified and analyzed with EDS at 100x magnification. Other phases present on the sample surface was also identified.

3.3 Modelling of heat loss of FeSi from furnace to ladle

Temperature reduction due to heat loss of FeSi metal from furnace to ladle and in the ladle will be calculated using theory presented in chapter 2. The problem has been divided into three parts:

- Heat transfer from FeSi to runner where heat convection has been assumed to be the most dominant heat transfer mechanisms, and heat transfer from FeSi to surrounding air where thermal radiation has been assumed to be the most dominant heat transfer mechanism.
- Thermal radiation from FeSi to surrounding air from the end of the runner to the ladle.

- Heat transfer from FeSi to ladle and from FeSi to the surrounding air where heat convection and thermal radiation has been assumed to be the most dominant heat transfer mechanisms respectively.

The problem is to calculate the heat loss and the resulting temperature difference of FeSi for the three parts mentioned above. A sketch of the problem can be found in figure 3.8 where the dimensions are visual estimations from a real tapping situation. In addition, FeSi in the runner will flow over a carbon block that is surrounded by refractory material. Some of the fixed parameters are also based on the measurements done during the measuring campaign, and the results of that can be found in chapter 4.

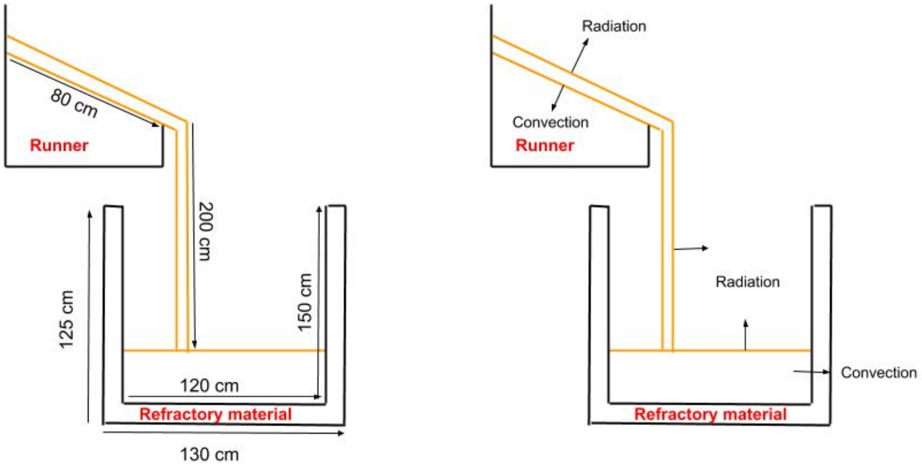

3.5

Figure 3.8: A sketch of the heat transfer problem.

For simplicity, the ladle and the FeSi flow from the end of the runner to the ladle is regarded as cylindrical, and the FeSi flow in the runner is regarded as half cylindrical. Other assumptions are:

- No heat convection and conduction in the FeSi melt resulting in a uniform temperature in the melt. Convection within the liquid body of FeSi may happen fast enough for the temperature to be uniform within a short period of time, so this assumption is reasonable.

- FeSi acts as a grey body with respect to radiation. This is not the case in real life, but this assumption is adequate for engineering purposes.

- All thermal radiation goes to the surrounding air, which is transparent with respect to radiation. This is a reasonable assumption if the air contains low concentrations of CO_2.

- Heat flow is directly proportional to so the surface area, which is consistent with the stagnant layer concept. This is adequate for an engineering calculation purpose.
- All heat from FeSi in the runner goes to the carbon block, which absorbes all of it. In real life, refractory material will encase the carbon block, and heat will be transferred between the two through conduction. In this case it is assumed that no conduction takes place between the two, and that conduction within the refractory material in the ladle and carbon block in the runner is very fast.
- Heat capacity and density is not dependent on temperature. This will not be the case in real life, but not enough data has been gathered for FeSi at this temperature to make accurate calculations on these material properties.
- Refractory material in the ladle is 50 % SiO_2 and 50 % Al_2O_3.
- The liquid FeSi contains 75 % Si and 25 % Fe.
- FeSi velocity is constant from furnace to ladle. This will not be the case in real life because of the "free fall" after the runner, but it is assumed that the increase of velocity in that part will have little effect for further calculations.
- No slag or SiC particles are present in the FeSi melt. Since FeSi production is considered a slag free process this might be a reasonable assumption.
- The temperature in the runner increases with 200°C within 30 minutes of tapping, which is based on results in chapter 4. A heat transfer coefficient h_c is estimated based on that.
- The FeSi temperatures in the furnace and between the furnace and ladle will be constant over the duration of tapping. This may not be the case in real life as the runner will heat up during the tapping, causing less and less heat to be transferred between FeSi and the runner. However, it is assumed that this will have little effect for the change in temperature in the ladle.

Before any calculations can be done, a heat transfer coefficient h_c for the runner and ladle needs to be estimated. This had been done in three ways: by the use of equation 2.18, 2.19, and by using empirical measurements from the measuring campaigns. By rephrasing equation 2.18 the expression for h_c for the ladle becomes

$$h_c = 0.53\frac{k_{Si}}{D}\left[\left(\frac{c_{p,FeSi}\nu_{FeSi}\rho_{FeSi}}{k_{Si}}\right)\left(\frac{D^3\beta_{Si}(T^0_{FeSi} - T^0_{ladle})g}{\nu^2_{FeSi}}\right)\right]^{0.25}. \tag{3.1}$$

By switching out T^0_{ladle} with T^0_{runner} in equation 3.1 the h_c for the runner can be calculated. Another estimation of h_c can be done by rephrasing equation 2.19 to

$$h_c = 0.27(T^0_{FeSi} - T^0_{ladle})^{0.25} \tag{3.2}$$

for the ladle, and

$$h_c = 0.2(T^0_{FeSi} - T^0_{runner})^{0.25} \tag{3.3}$$

for the runner. Equation 3.2 and 3.3 requires the temperatures to be in Fahrenheit. The last method used for estimating h$_c$ is by assuming that the runner has increased 200°C after 30 minutes of tapping as stated earlier, and calculate the amount of heat energy that is required to heat the runner up to that amount:

$$Q_{runner} = mC_{p,C}\Delta T, \tag{3.4}$$

where ΔT equals 200°C. The heat transfer coefficient can then be calculated by rephrasing equation 2.17:

$$h_c = \frac{Q_{runner}}{A(T^0_{FeSi} - T^0_{runner})t}, \tag{3.5}$$

where t equals 1800 seconds (30 minutes). The heat transfer coefficient will be estimated by the use of all three methods mentioned above.

The first part of the problem will investigate the heat loss from FeSi to the runner. The heat loss is mostly due to radiation and convection heat transfer between FeSi and surrounding air, and between FeSi and the runner respectively. This has been calculated in one step over the time it takes from FeSi to travel from the furnace to the end of the runner by using the following equations:

$$Q_{c,1} = h_c \frac{\pi d_{FeSi} L_{runner}}{2}(T^0_{FeSi} - T^0_{runner}) L_{runner} \frac{8\dot{m}}{\pi d^2_{FeSi} \rho_{FeSi} 3600} \tag{3.6}$$

for convective heat transfer from FeSi to runner and

$$Q_{r,1} = \varepsilon d_{FeSi} L_{runner} \sigma (T^0_{FeSi})^4 L_{runner} \frac{8\dot{m}}{\pi d^2_{FeSi} \rho_{FeSi} 3600} \tag{3.7}$$

for thermal radiation. The resulting temperature difference due to the convective and radiation heat loss has been calculating with

$$\Delta T_1 = (Q_{c,1} + Q_{r,1}) \frac{8}{\pi d^2_{FeSi} L_{runner} \rho_{FeSi}} \frac{1}{C_{p,FeSi}}. \tag{3.8}$$

The next part of the problem is the heat loss of FeSi from runner to the ladle due to thermal radiation. This has been calculated in one step over the time it takes from FeSi to go from the end of the runner to the ladle by using the following equation:

$$Q_{r,2} = \varepsilon h \pi d_{FeSi} \sigma (T^0_{FeSi} - \Delta T_1)^4 h \frac{8\dot{m}}{\pi d^2_{FeSi} \rho_{FeSi} 3600}. \tag{3.9}$$

where h is the height from the runner to the ladle given in figure 3.8. The resulting temperature difference due to thermal radiation has been calculated with

$$\Delta T_2 = Q_{r,2}\frac{8}{\pi d_{FeSi}^2 h \rho_{FeSi}}\frac{1}{C_{p,FeSi}}. \tag{3.10}$$

The third part of the problem has been calculated in 30 steps because the geometry changes over time due to the ladle filling up with FeSi. In this part heat transfer will happen through thermal radiation at the top and convective heat transfer at the wall and bottom of the ladle. Additionally, heat will be added to the system by new FeSi entering the ladle. It is assumed that all the energy released by cooling new FeSi to the temperature of FeSi in the ladle contributes to the overall heat changes in the ladle. The heat transfer through the wall has been calculated with the following equation:

$$Q_{x,wall} = h_c \pi r_{ladle} H_x (T_{ladle,x-1} - T_{FeSi,x-1})\Delta t, \tag{3.11}$$

where Δt is 60 seconds and H_x is the level of metal in the ladle given by

$$H_x = \frac{\dot{m}}{60\rho_{FeSi}\pi r_{ladle}^2} + H_{x-1}. \tag{3.12}$$

The level of FeSi in the ladle is H_0 = 0 at the start of the iteration. The start temperature of the FeSi in the ladle, $T_{FeSi,0}$, is given by

$$T_{FeSi,0} = T_{FeSi}^0 - \Delta T_1 - \Delta T_2. \tag{3.13}$$

The heat transfer through the bottom of the ladle is given by

$$Q_{x,bottom} = h_c \pi r_{ladle}^2 (T_{ladle,x-1} - T_{FeSi,x-1})\Delta t, \tag{3.14}$$

and the heat loss due to radiation is given by

$$Q_{x,r} = -\varepsilon\sigma\pi r_{ladle}^2 T_{FeSi,x-1}^4 \Delta t. \tag{3.15}$$

The addition of new FeSi will add heat to the ladle in the following way:

$$Q_{x,add} = C_{p,FeSi}(T_{FeSi,0} - T_{FeSi,x-1})\frac{\dot{m}}{3600}\Delta t. \tag{3.16}$$

The total change of heat for FeSi in the ladle for each iteration is given by $Q_{x,tot} = Q_{x,wall} + Q_{x,bottom} + Q_{x,r} + Q_{x,add}$, and the total heat going in to the ladle for each iteration is given by $Q_{x,totl} = -Q_{x,wall} - Q_{x,bottom}$. The temperature differences between FeSi and ladle can now be calculated with the following equations:

$$\Delta T_{FeSi,x} = \frac{Q_{x,tot}}{\pi r_{ladle}^2 H_x \rho_{FeSi} C_{p,FeSi}} \tag{3.17}$$

and

$$\Delta T_{ladle,x} = \frac{Q_{x,totl}}{m_{ref} C_{p,FeSi}}. \tag{3.18}$$

The new FeSi temperature in the ladle is given by $T_{FeSi,x} = T_{FeSi,x-1} + \Delta T_{FeSi,x}$, and the new ladle temperature is given by $T_{ladle,x} = T_{ladle,x-1} + \Delta T_{ladle,x}$.

The fixed parameters for each model simulation can be found in table 3.2. The heat capacity and density of the refractory material and the heat capacity of carbon has been found by HSC Chemical 9. The density of liquid FeSi has been calculated by using the mass fractions of the components and density data for liquid silicon found by Rhim and Ohsaka (2000) and liquid iron found by Jimbo and Cramb (1993). This is correct if it is assumed ideal mixing where the change of volume due to mixing is zero. The amount of FeSi tapped during a simulation is based on trends found during the measuring campaigns. The starting temperatures of FeSi, runner and ladle is also based on finding during the measuring campaigns. The thermal conductivity of silicon at 1800°C was found by Kobatake et al. (2007), kinematic viscosity of FeSi at melting point with 29 % Si was found by Bel'tyukov et al. (2014), and the thermal expansion coefficient for Si at melting point was found by Langen et al. (1998).

Table 3.2: Fixed parameters during model simulations.

Symbol	Description	Value	Unit
$C_{p,ref}$	Heat capacity of refractory material at 700°C	1182	$Jkg^{-1}K^{-1}$
$C_{p,C}$	Heat capacity of carbon at 700°C	1783	$Jkg^{-1}K^{-1}$
ρ_{ref}	Density of refractory material	3283	kgm^{-3}
ρ_{FeSi}	Density of liquid FeSi	3730	kgm^{-3}
k_{Si}	Thermal conductivity of silicon at 1800°C	60	$Wm^{-1}K^{-1}$
ν_{FeSi}	Kinematic viscosity of FeSi	$6\cdot 10^{-7}$	m^2s^{-1}
β_{Si}	Thermal expansion coefficient for silicon	$1.4\cdot 10^{-4}$	K^{-1}
t	Tapping time	30	min
m_C	Mass of runner	50	kg
T^0_{FeSi}	Start temperature of FeSi	1900	°C
T^0_{runner}	Start temperature of runner	700	°C
T^0_{ladle}	Start temperature of ladle	700	°C

Four parameters were chosen to vary in the model simulations: Heat capacity C_p, emissivity of FeSi ε_{FeSi}, the diameter of FeSi metal flow d_{FeSi}, and mass flow rate $\dot{m}$. One parameter was changed during one case while the others were given fixed values, where both the range and fixed values are shown in table 3.3.

Table 3.3: Variables during model simulations. If nothing else is stated the values given in this table are fixed.

Symbol	Description	Range	Value*	Unit
$C_{p,FeSi}$	Heat capacity of FeSi	[700:100:1100]	932	$\mathrm{Jkg^{-1}K^{-1}}$
ε_{FeSi}	Emissivity of FeSi	[0.2:0.2:1]	0.5	
d_{FeSi}	Diameter of FeSi metal flow	[0.02:0.02:0.1]	0.05	m
$\dot{m}$	Mass flow rate	[6000:1000:10000]	8500	$\mathrm{kgh^{-1}}$

In addition to the cases mentioned above three special cases were also done where the mass flow rate changes with time. This was done it the following way:

1. Mass flow rate starts at 10 000 kg/h and decreases with a rate of 100 kg/(h min). This was done to simulate a "good tapping" where the mass flow rate is very high in the beginning, but slowly decreases over time.
2. Mass flow rate starts at 7000 kg/h and decreases with a rate of 100 kg/(h min) for 10 minutes then increases rapidly to 10 000 kg/h which then again decreases with a rate of 100 kg/(h min). This was done to simulate a bad start to the tapping, but where the problem was fixed after a time.
3. Mass flow rate starts at 8000 kg/h and increases with a rate of 100 kg/(h min) for 15 minutes, then decreases with a rate of 100 kg/(h min) for 15 minutes. This was done to simulate a situation where the operator uses some time to clean and open up the tapping hole.

The start temperature in the ladle (1835°C) for these special cases will be the same for better comparison. The mean mass flow rate will also be almost the same for the three cases (8500 kg/h).

Chapter 4

Results

The results from measurements in the ladle and runner will be presented here. The chemical analysis of the FeSi samples and slag samples will also be presented in this chapter. Finally, the results from the heat transfer modelling will be presented.

4.1 Temperature measurements

Measurements in the ladle were done with S-type and C-type thermocouples, and measurements in the runner were done with C-type and K-type thermocouples. Each tapping session is identified with a 4 digit number for future reference. The results from measurements with the S-type thermocouples will be the main focus. For more information about the results with the other thermocouples see the works of Ksiazek et al. (2018).

The results from dip measurements in the ladle with the S-type thermocouple can be seen in figure 4.1. The tapping sessions are identified with a four digit number where tapping sessions 2XXX are from the first campaign and 3XXX are from the second campaign. There is a general downward trend for most tapping session, and it was found that the starting temperatures in the ladle varies up to 120°C from tapping session to tapping session. Other tapping sessions did not show the same downwards trend, and varied a lot throughout the tapping.

Normalized operational data for each tapping session can be found in table 4.1. The normalized electrode current (I 1-3) and the power load on the furnace are based on the average electrode current within two hours before a tapping session started compared to the average for the whole campaign period. The normalized absolute movements of the electrodes (AM 1-3) per hour is the total upwards and downwards movements of the electrodes per hour and is also based on the average absolute movements of the electrodes per hour within the first two hours before a tapping session compared to the average movements of the electrodes per hour for the whole campaign. The normalized movements of the electrodes (M 1-3) is the relative movement of the electrodes showing if the electrodes moved up or down in within two hour before a tapping session. For the tapping session where the electrode moved downward the normalization is based on the average downwards movements for all these tapping session. The same goes for the upwards movements. The normalized mass flow rate (MF) is based on the average mass flow rate for all the tapping sessions. The box coloring for I 1-3, power, AM 1-3, and MF tells if the value is lower than the average (red), close to average (yellow), or above average (green). For M 1-3 the box coloring tells if the electrodes are moving upward (green) or downward (red). Observations were made at the start (S), midway (M), or end (E) for each tapping sessions. The observations that were made were excess burning in the runner (EB), low metal flow (LMF), high metal flow (HMF), blowing with oxygen (O2), and excess gassing (EG).

The electrical current on the electrodes and the power is close to average for most of the tapping sessions, except for tapping session 2485, 3125, 3135, 3136, and 3137 because of incidents which led to the power being lowered. Electrode 1 shows a lot of movement during the first campaign, but very little movement during the second campaign. Electrode 2 and 3 moved much less in both campaigns, but they have both seem to move downward in the time before tapping started.

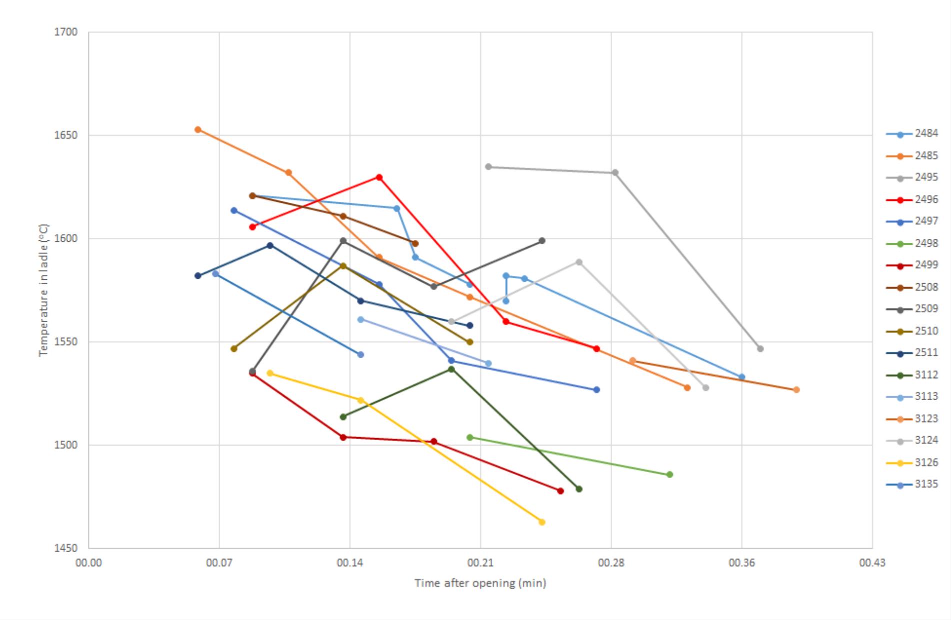

Figure 4.1: Temperature measurements in the ladle with S-type thermocouples for each tapping session.

Table 4.1: Normalized operational data for each tapping session where I 1-3 is the electrical current on electrode 1-3, power is the power load on the furnace, AM 1-3 is the absolute movements of electrode 1-3, M 1-3 is the relative movements of electrode 1-3, and MF is the mass flow rate of FeSi. The first letter in the observations indicates if it was observed in the start (S), midway (M), or end (E) of the tapping. The observations are excess burning (EB), low metal flow (LMF), high metal flow (HMF), O_2 blowing (O2), and excess gassing (EG).

Tap #	I 1	I 2	I 3	Power	AM 1	AM 2	AM 3	M 1	M 2	M 3	MF	Observations
2484	1.00	1.01	1.01	1.04	2.27	1.30	0.67	-0.62	-0.48	1.00	0.73	M.LMF, E.EB
2485	0.91	0.90	0.90	0.91	0.77	0.97	0.47	-1.45	-0.24	-0.40	0.94	M.LMF, E.O2
2495	1.02	1.01	1.05	1.04	0.61	0.97	0.63	-1.45	0.94	.0.67	1.00	
2496	0.96	0.96	1.00	0.96	1.59	0.94	0.89	0.65	-0.72	-1.33	0.97	M.EB
2497	1.02	1.01	1.01	1.00	1.16	1.11	1.11	0.37	0.31	-0.93	1.03	Cold ladle
2498	1.02	1.01	1.00	1.03	1.07	1.04	1.07	0.93	1.41	-0.80	1.00	S.LMF, S.EG
2499	1.02	1.01	1.01	1.04	1.40	0.97	0.89	-0.10	-1.20	-1.47	1.07	S.HMF
2508	1.00	1.01	0.97	1.00	1.50	0.83	1.30	1.11	0.47	-0.67	1.11	S.HMF, M.EB
2509	0.99	1.04	1.00	0.98	1.25	0.68	0.90	-1.34	-1.92	-0.93	1.03	M.EG, E.O2
2510	0.99	1.04	0.97	0.95	2.04	0.89	0.54	1.94	-1.44	-0.53	0.99	M.O2, E.LMF
2511	1.00	1.02	0.96	0.95	0.86	0.83	0.60	-1.03	1.88	-2.27	0.86	S.EG, M.HMF
3112	1.07	1.03	1.02	1.09	1.48	0.72	1.34	-1.52	-1.54	-1.76	0.68	S.O2, M.LMF, M.EB
3113	1.09	1.03	1.03	1.02	0.86	0.54	1.16	1.09	-0.38	-0.35	1.06	E.LMF
3123	1.02	1.03	1.02	1.02	0.90	1.04	0.76	-0.91	-1.15	-1.41	0.68	S.LMF, M.EB
3124	1.03	1.01	1.01	0.96	0.84	0.87	1.28	-0.30	-0.38	-0.71	1.12	S.O2
3125	0.90	0.93	0.90	0.87	1.27	1.19	1.02	-2.12	0.00	-1.32	1.15	E.O2
3126	1.02	1.03	1.03	1.02	0.97	0.59	1.27	-0.15	0.00	1.00	0.99	S.HMF
3135	0.57	0.57	0.57	0.48	0.97	1.09	0.86	0.91	-1.54	-0.44	1.32	
3136	0.87	0.88	0.88	0.81	0.96	1.14	0.76	-0.48	0.36	-0.30		S.HMF, E.LMF
3137	0.86	0.86	0.86	0.77	0.46	0.99	0.54	0.89	-2.25	-0.04		S.HMF, E.LMF

Halfway through tapping session 2484 temperatures across the ladle was measured with S-type thermocouples as shown in figure 4.2. The temperature varies little in the ladle, except for T_2 which deviates by around 30°C from the other measurements and can be considered an outlier. If T_2 is neglected the mean temperature in the ladle in this tapping session is 1578^oC.

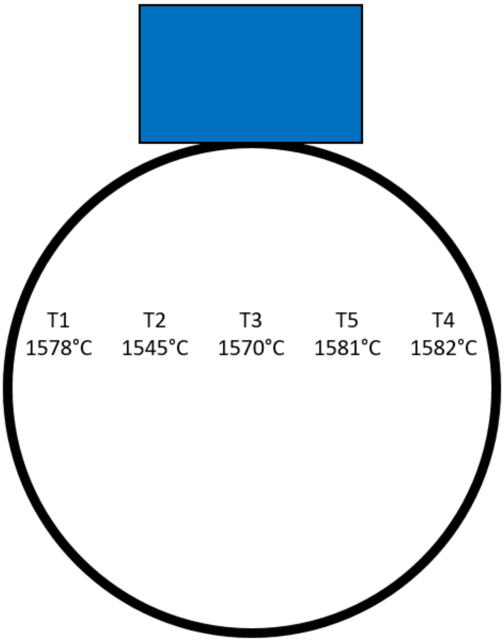

Figure 4.2: Temperatures measured across the ladle with S-type thermocouples for tapping session 2484.

The temperature in the FeSi flow was also measured with S-type thermocouples, and the results compared to the results from the temperature measurements in the ladle for tapping session 2495, 2496, and 2497 can be seen in figure 4.3. Measuring the temperature in the flow proved difficult as the lance was held unsteady or the thermocouple broke because of the force from the flow. Nevertheless, most measurements showed that the temperature in the flow was between 10^oC to 100^oC higher than the temperature measured in the ladle. The temperature range for the S-type thermocouple goes up to 1767°C, but only measurements in tapping session 2495 were close to this maximum.

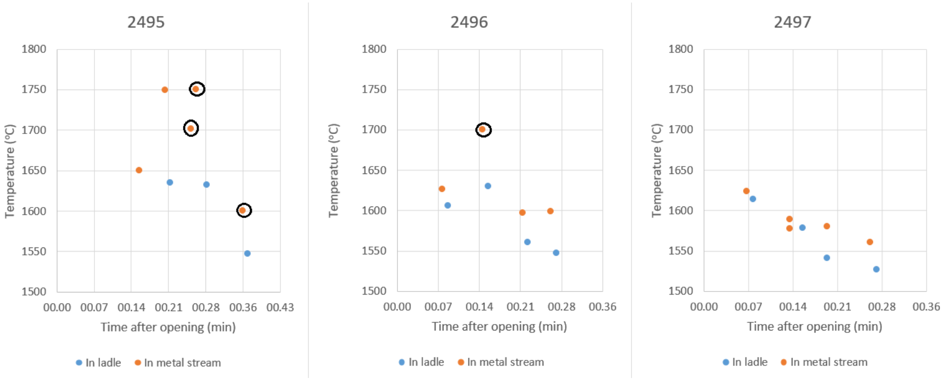

Figure 4.3: Temperatures measured in the flow compared to the temperature measured in the ladle. The circled points are the highest temperature measured before an error message was displayed on the instrument.

Measurements in the ladle with C-type thermocouples were done at several tapping sessions. The results for tapping session 3135 can be found in figure 4.4 together with results with S-type thermocouples from the same tapping session. The same trend was evident for both types of thermocouple for all measurements done of this kind.

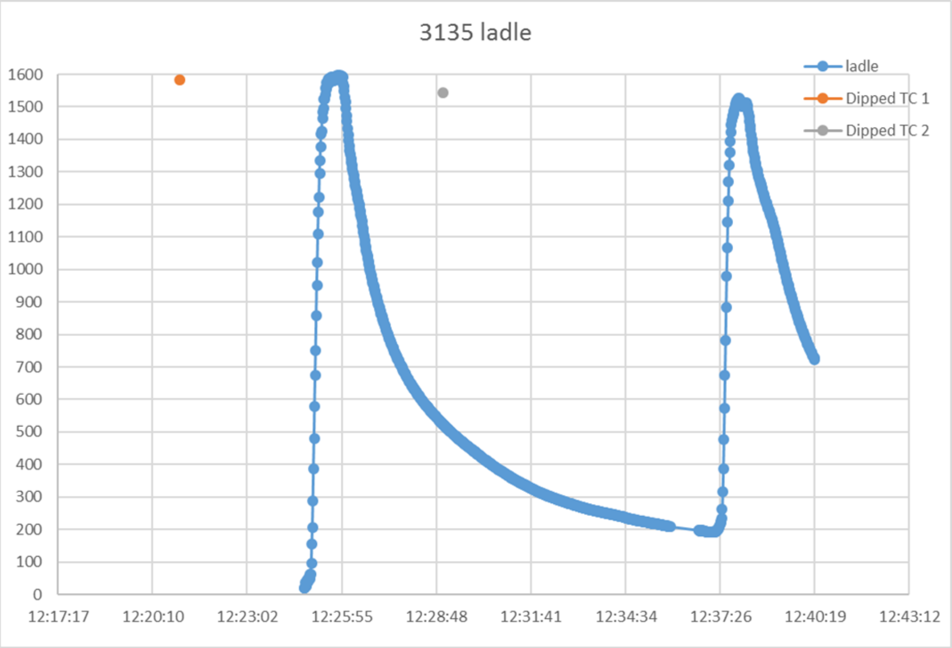

Figure 4.4: Measurements in the ladle with C-type thermocouple (blue points) and S-type thermocouples (orange and grey points).

The temperature of FeSi in the runner was measured with C-type thermocouples during eight tapping session. The results from these measurements can be seen in figure 4.5 for the first campaign and in figure 4.6 for the second campaign. The temperatures in the runner seem to be held steady through each tapping sessions and varies from 1760°C to 1920°C. At the end of some tapping session there are some disturbances where the operator started to burn or ”clean” the runner. There were also some disturbances in the measurement when the thermocouple was moved around. In some cases the thermocouple ended up measuring the air above the metal flow, which shows up in the graph as a sudden drop in temperature.

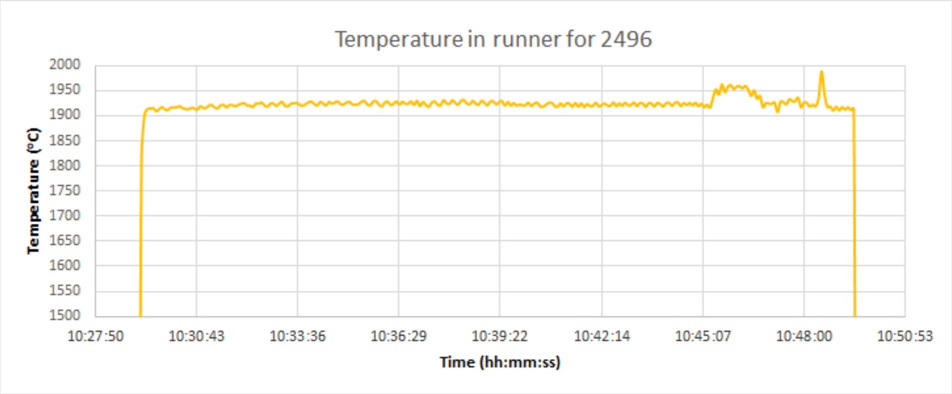

Figure 4.5: The temperature of FeSi in the runner for tapping session 2496.

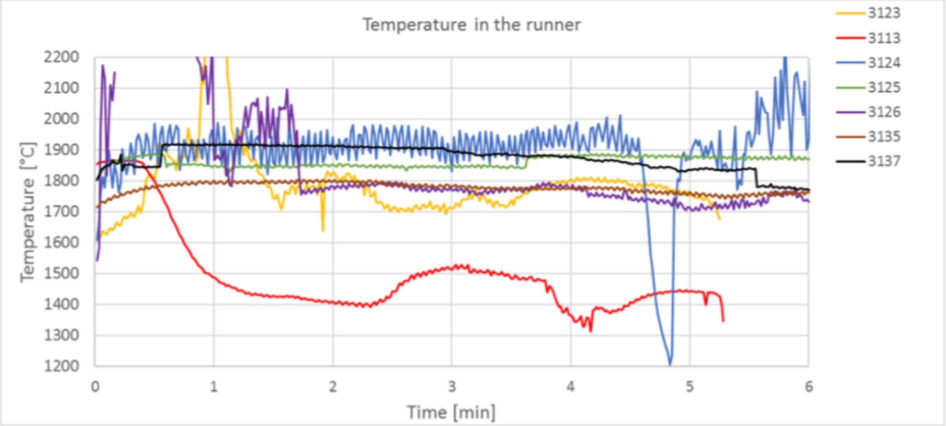

Figure 4.6: The temperature of FeSi in the runner during the second campaign at Finnfjord AS.

In the last campaign two K type thermocouples were embedded in the runner right underneath the FeSi flow. It measured the temperature of the runner for two days and the results from that can be seen in figure 4.7. The thermocouple in the back was situated close to the furnace, while the thermocouple in the front was close to the end of the runner. As the tapping hole is opened and FeSi started to flow the temperature in the new and cold runner increases rapidly from 200°C to over 500°C in the back and from 100° to over 300° in the front. The temperature decreases again when no tapping occurs. Over time the maximum temperature of the runner stabilizes at around 850° in the back and at around 800° in the front. The mean temperature difference during a tapping session is 111° in the back and at around 212° in the front, excluding periods when the tapping hole was not in use at around the 10th, 25th, and 45th hour.

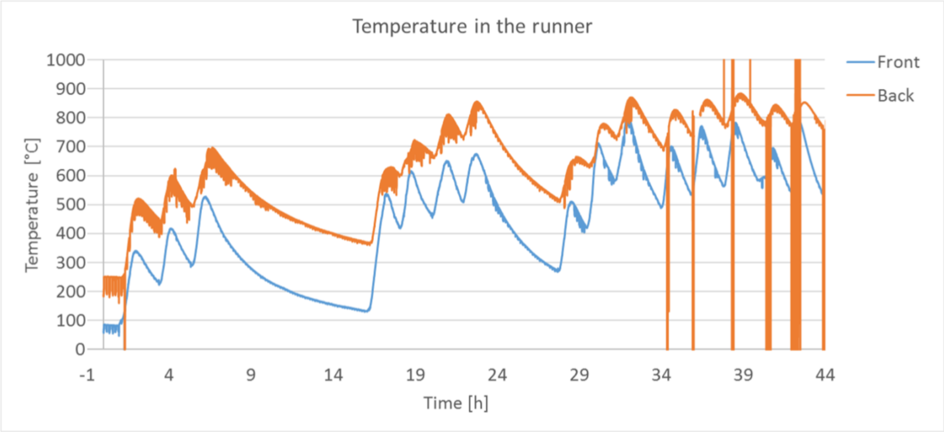

Figure 4.7: The temperature in the runner during the second campaign.

4.2 FeSi samples

FeSi samples were collected for 19 tapping sessions and analyzed for chemical composition with XRF. What was of most interest from the XRF results were the aluminum and calcium content in FeSi and how that varied throughout a tapping sessions. This is presented in figure 4.8 where aluminum and calcium content is shown varying throughout 12 tapping sessions. Only one sample was collected for each of the remaining tapping sessions. The average aluminum and calcium concentrations in FeSi from the different tapping sessions are given in table 4.2.

In several of the cases in figure 4.8 the aluminum and calcium content are relatively constant and only increases slightly as time progresses. In tapping session 2484, 2485, and 2497 the aluminum content seem to increase notably at the end of the session. For tapping sessions where only two samples were collected it is hard to tell the trend, but it seems like also here the variation is small.

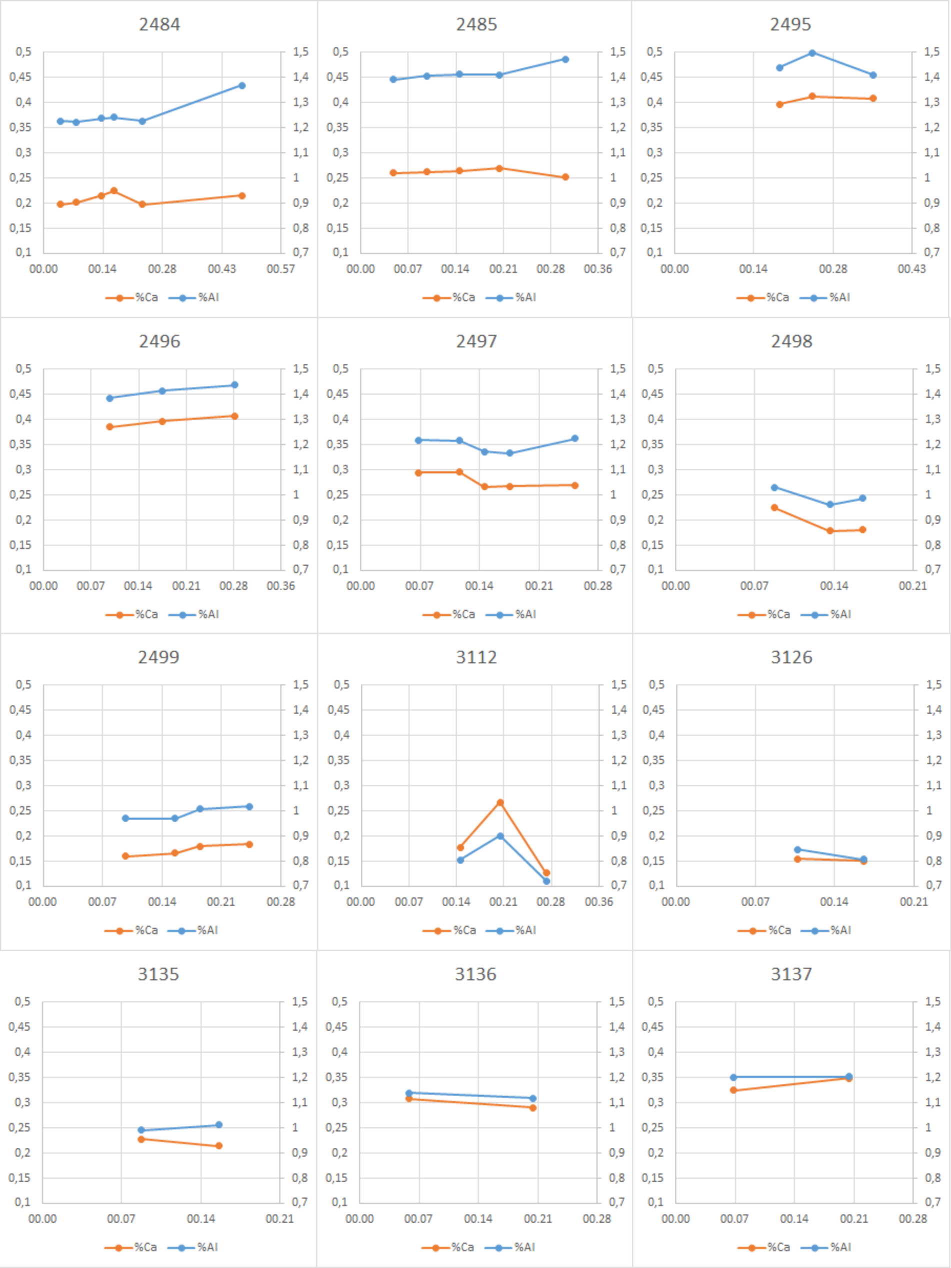

Figure 4.8: Aluminum and calcium content in metal samples from tapping session where several metal samples were collected. The x-axis is the time after the tapping hole was opened in minutes, the left y-axis is mass percentage of calcium, and the right y-axis is the mass percentage of aluminum.

Table 4.2: The average aluminum and calcium concentration in FeSi in weight percentage for each tapping session. Only one FeSisample was collected for the tapping sessions marked with bold letters.

Tap #	$\%\mathbf{Ca}_{av}$	$\%\mathbf{Al}_{av}$
2484	0.21	1.25
2485	0.25	1.42
2495	0.41	1.45
2496	0.40	1.41
2497	0.28	1.20
2498	0.20	0.99
2499	0.17	0.99
2508	0.14	0.98
2509	0.23	1.20
2510	0.19	1.00
2511	0.16	0.92
3112	0.19	0.81
3113	0.19	0.86
3124	0.27	1.14
3126	0.15	0.83
3135	0.22	1.00
3136	0.30	1.13
3137	0.34	1.20

4.3 Slag samples

Four slag samples were collected during the first measuring campaign. One sample was collected after tapping session 2485 and three samples were collected after tapping session 2496. All of the slag samples were cut, molded in epoxy, and analyzed for chemical composition with EDS in SEM.

The slag sample collected after tapping session 2485, from now on called sample 1, was collected from an iron rod that the operator used to clean the runner. A picture of sample 1 can be seen in figure 4.9. The sample contained mostly slag with a a few visible metal drops and carried a light weight. The slag was porous and had a glass like appearance which made it easy to break apart.

Figure 4.9: Slag sample collected after tapping session 2585 (slag sample 1).

A slag sample collected from one of the sides of the runner was collected after tapping session 2496 when the runner had cooled down. From now on this sample will be called sample 2, and a picture of it can be found in figure 4.10. Sample 2 was heavy and contained a lot of FeSi with only a few slag drops.

Figure 4.10: Slag sample from one of the sides of the runner collected after tapping session 2496 (slag sample 2).

A slag sample was collected from the front of the runner, also called a ”beard”, after tapping session 2496, and will from now on be called sample 3. The sample contained larger areas of slag encased with FeSi. It contained mostly FeSi so it was somewhat heavy for it size. A picture of sample 3 can be found in figure 4.11.

Figure 4.11: Slag sample from the front of the runner collected after tapping session 2496 (slag sample 3).

A slag sample was collected from the bottom of the runner after tapping session 2496, and will from now on be called sample 4. It contained layers of slag and FeSi over some carbon materials from the runner and ramming paste. A picture of sample 4 can be seen in figure 4.12.

Figure 4.12: Slag sample from the bottom of the runner collected after tapping session 2496 (slag sample 4).

A cut section of each sample was made ready for analysis in SEM as shown in figure 4.13. The cut section of slag sample 1 shows an porous area with slag with a few FeSi metal drops. The cut section of slag sample 2 shows an area with FeSi, and with only a few drops of slag that is barley visible with the naked eye. The cut section of slag sample 3 shows a large slag area with a smaller FeSi layer. The cut section of slag sample 4 shows an area mixed with FeSi metal and different types of slags. One area on each sample was analyzed with EDS in SEM, and it is marked with red circles in figure 4.13.

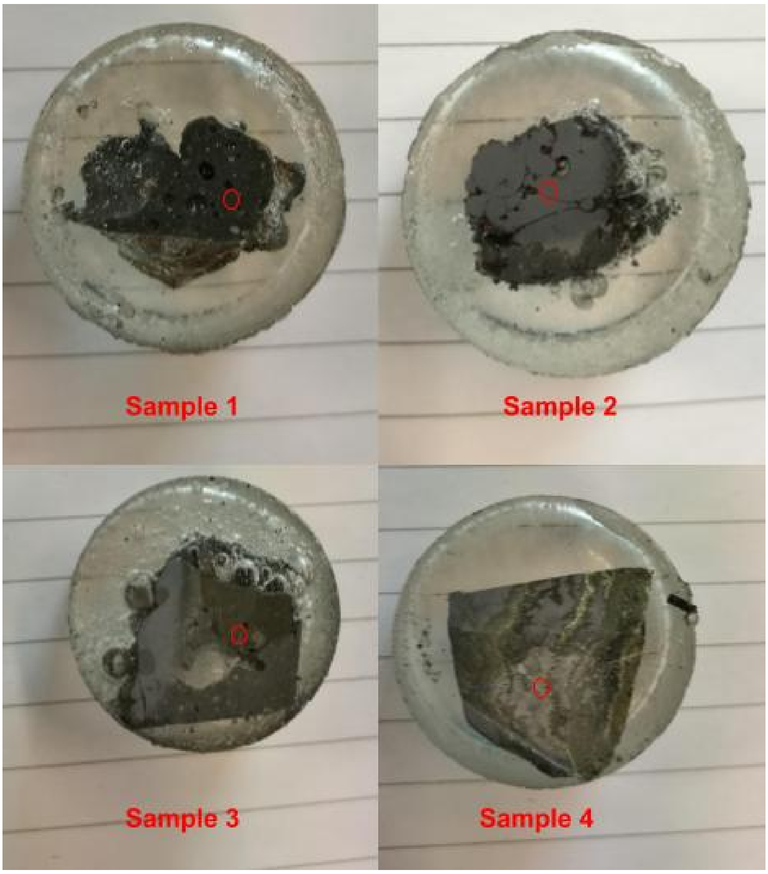

Figure 4.13: A cut section of slag sample 1-4. The red circles indicate areas that were analyzed.

The area on slag sample 1 that was analyzed with EDS can be found in figure 4.14. This area contained two different slag phases, epoxy filled pores, and some iron droplets. The result from the EDS analysis of the different phases present in this area can be found in table 4.3.

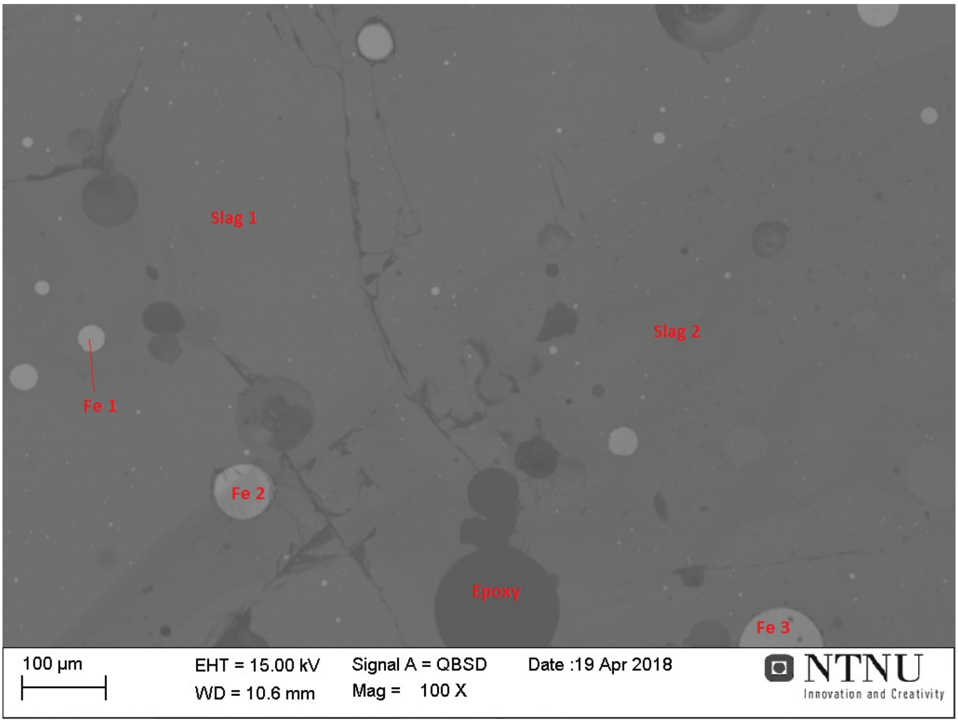

Figure 4.14: Area on slag sample 1 that was analyzed with EDS in SEM.

Even though it appears to be two different slag phases present in this area because of the contrast difference, this is not the case. The contrast difference is caused by uneven carbon coating because the ratio between the components in the slag is the same, excluding the iron oxide found in slag phase 2.

Table 4.3: The EDS results from slag sample 1.

Phase	**C** (%)	**O** (%)	**Si** (%)	**Ca** (%)	**Al** (%)	**Fe** (%)	**Cl** (%)
Slag 1	8.5	39.1	30.88	7.7	10.3		
Slag 2	22.3	35.0	25.3	6.1	8.7	2.4	
Fe 1	6.2		1.3			81.0	
Fe 2	20.1	3.2	2.0			74.8	
Fe 3	14.3	2.3	1.8			81.7	
Epoxy	75.2	23.9					0.8

The area on slag sample 2 that was analyzed with EDS in SEM can be found in figure 4.15. This area contained large amount of silicon, FeSi, and epoxy. A smaller slag area and an iron droplet was also found. The results from the EDS analysis of the different phases present in this area can be found in table 4.4.

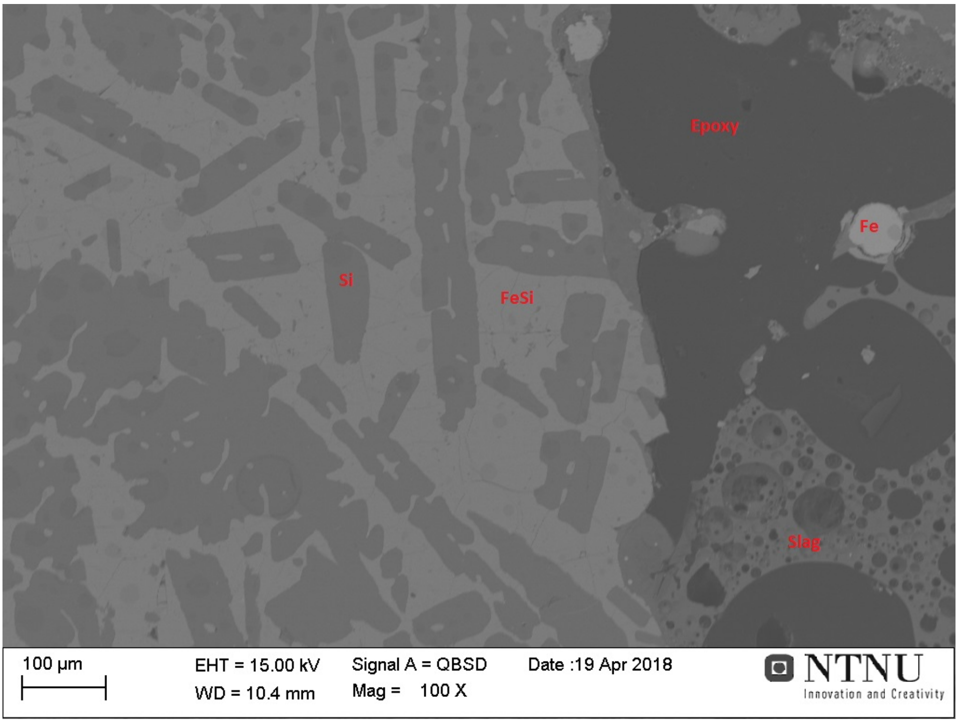

Figure 4.15: Area on slag sample 2 that was analyzed with EDS in SEM.

As mentioned earlier, the slag sample contained a lot of FeSi which made an area with slag hard to find. The area in figure 4.15 was the only area on the cut section of sample 2 with a slag phase of this size.

Table 4.4: The EDS results from slag sample 2.

Phase	**C (%)**	**O (%)**	**Si (%)**	**Ca (%)**	**Al (%)**	**Fe (%)**	**Cl (%)**
Slag	11.3	38.8	20.4	11.9	11.9	4.9	
FeSi	10.4		44.5		1.2	39.5	
Si	14.9	1.0	84.1				
Fe	7.2					92.9	
Epoxy	77.5	21.5					1.0

The area on slag sample 3 that was analyzed with EDS in SEM can be found in figure 4.16. This area contained a large slag matrix with some smaller areas with FeSi and epoxy. The results from the EDS analysis of the different phases present in this area can be found in table 4.5.

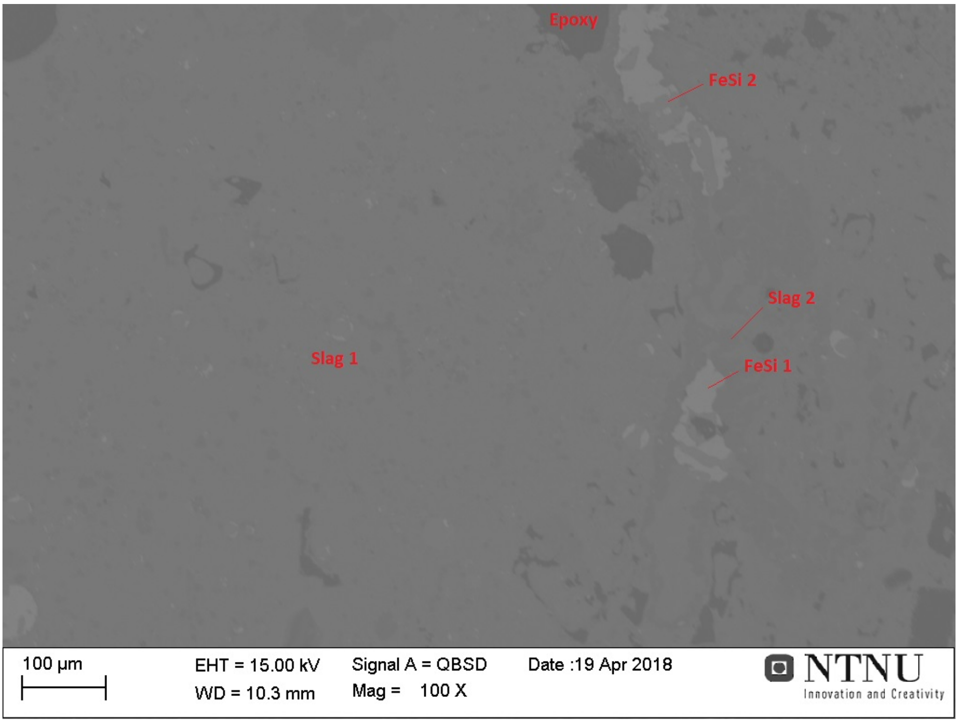

Figure 4.16: Area on slag sample 3 that was analyzed with EDS in SEM.

There are two slag phases present in this area, but slag phase 1 will be considered as the main slag phase because it appears in much larger amounts.

Table 4.5: The EDS results from slag sample 3.

Phase	C (%)	O (%)	Si (%)	Ca (%)	Al (%)	Fe (%)	Cl (%)	Ti (%)
Slag 1	7.4	33.9	14.6	27.7	16.3			
Slag 2	13.8	22.5	36.5	12.8	14.4			
FeSi 1	11.7		49.1			39.2		
FeSi 2	19.2	2.4	49.4			28.0		1.1
Epoxy	79.9	19.4					0.71	

The area on slag sample 4 that was analyzed with EDS in SEM can be found in figure 4.17. This area contained FeSi, Si, and slag phases distributed around the area. The results from the EDS analysis of the different phases present in this area can be found in table 4.6.

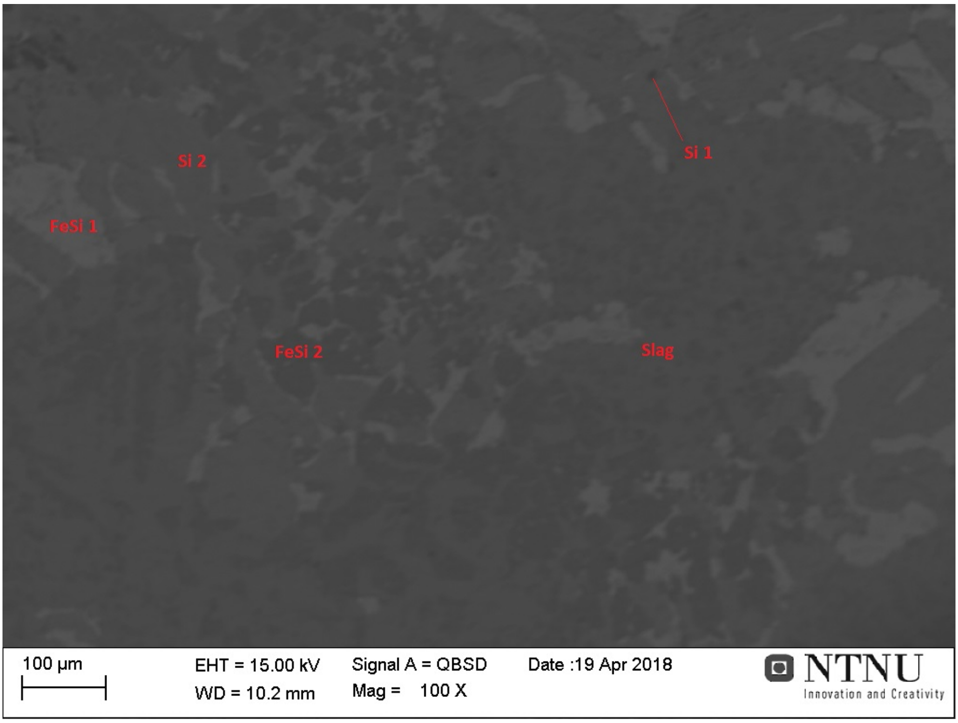

Figure 4.17: Area on slag sample 4 that was analyzed with EDS in SEM.

It appears to be an uneven carbon coating in this area, so the contrasts seen in figure 4.17 is most likely not representative for the sample itself. The focus is also a bit off because of aberrations.

Table 4.6: The EDS results from slag sample 4.

Phase	C (%)	O (%)	Si (%)	Ca (%)	Al (%)	Fe (%)
Slag	7.1	35.0	12.7	25.4	19.9	
FeSi 1	11.4		48.8			39.9
FeSi 2	27.4	1.6	66.9			4.1
Si 1	53.0	1.5	45.5			
Si 2	15.1	1.3	83.6			

The composition of the slag phases found on slag sample 1-4 with respect to Al_2O_3, CaO, and SiO_2 can be found in table 4.7. Their respective liquidus point, viscosity, and density is also in the same table, and was found by using theory in chapter 2. In figure 4.18 the compositions is plotted in the phase diagram for the Al_2O_3-CaO-SiO_2 slag system.

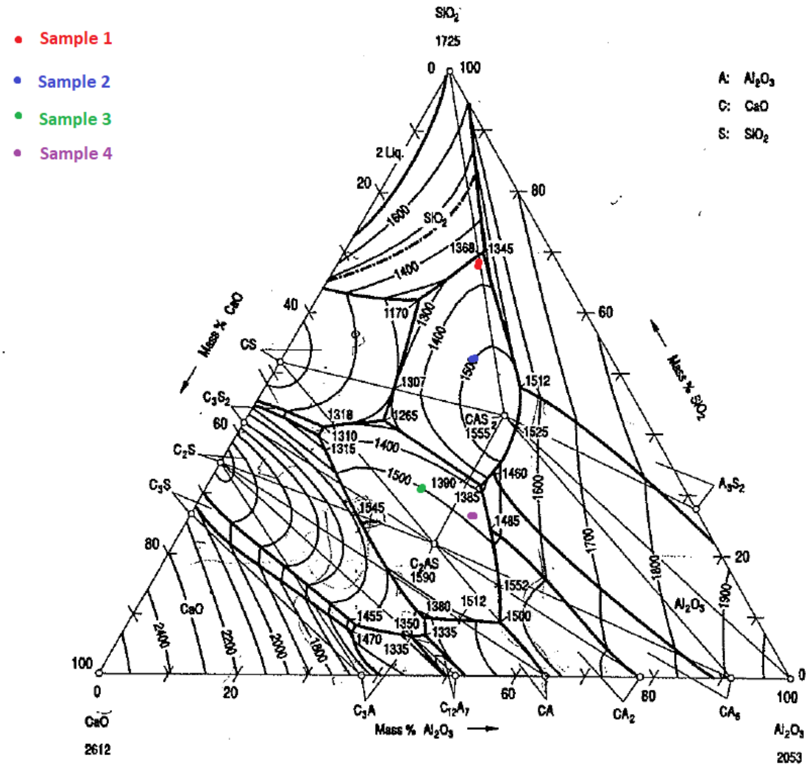

Figure 4.18: The Al_2O_3-CaO-SiO_2 phase diagram with the plotted composition for slag sample 1-4.

Slag sample 1, which was found to be stuck on an iron rod, have the lowest liquidus point at 1325°C and the highest viscosity at 400 P. Slag sample 2, which was found on one of the sides of the runner, has a liquidus point at 1500°C and viscosity at 30 P. Slag sample 3, which was found at the end of the runner, also has a liquidus point at 1500°C, but with a viscosity at 16 P. Slag sample 4, which was found at the bottom of the runner, has a liquidus at 1475°C and a viscosity at 6 P. The densities for the four slag samples differs very little from one another.

Table 4.7: The composition of the slag phases found on slag sample 1-4 and their respective liquidus point (T_L), viscosity (μ), and density (ρ). The viscosities are given at 1500 °C and the densities are given at 1565°C, 1600°C, and 1550°C for sample 1, 3, and 4 respectively.

Sample	Al_2O_3 (%)	CaO (%)	SiO_2 (%)	T_L(°C)	μ (P)	ρ (g/cm^3)
1	20.2	11.2	68.6	1325	400	2.65
2	27.2	20.1	52.7	1500	30	
3	30.5	38.5	31.0	1500	16	2.71
4	38.6	33.6	27.8	1475	6	2.58

4.4 Modelling of heat loss of FeSi from furnace to ladle

A simulation of heat loss and temperature decrease of FeSi from furnace to ladle has been carried out and the results of that is presented in this chapter. The problem was divided into three part: Temperature in the runner (part 1), temperature between runner and ladle (part 2), and temperature in the ladle (part 3). Four parameters were chosen to vary in the model simulations: Heat capacity C_p, emissivity of FeSi ε_{FeSi}, the diameter of FeSi metal flow d_{FeSi}, and mass flow rate $\dot{m}$. A total of 23 cases have been studied.

First, the heat transfer coeffcicient h_c was estimated using three different methods, and the results of that can be found in table 4.8. The h_c value varies greatly using the different estimation methods, but method 2 and 3 seems more reliable for these calculation purposes. A decision was made to use the h_c value given by method 3 for further calculations.

Table 4.8: The results of estimation of heat transfer coefficient, h_c, using different methods.

Method	h_c Runner (W/(m^{2}K))	h_c Ladle (W/(m^{2}K))
1	38373	38373
2	7.8	10.6
3	131	131

The results from cases where different heat capacities for FeSi were applied can be found in figure 4.19 for part 1 and 2, and figure 4.20 for part 3. For both part 1 and 2 the temperatures increases with increased heat capacity, more for the latter than the former. The temperature in the runner seem to vary little with changing heat capacities and the difference in temperature in part 1 and part 2 gets smaller with increased heat capacity. A summary of the temperature differences and heat loss is given in table 4.9.

Table 4.9: The temperature differences in the runner (ΔT_1), when in free fall (ΔT_2), and in the ladle (ΔT_3) at different heat capacities for FeSi. The total heat loss from radiation (Q_r) and convection (Q_c) for the simulated tapping sessions are also given in percentage.

C_p (J/(kgK))	ΔT_1 (°C)	ΔT_2 (°C)	ΔT_3 (°C)	Q_r (%)	Q_c (%)
700	14.9	68.0	280.2	53.2	46.8
800	13.1	59.8	258.4	53.6	46.4
900	11.6	53.3	239.7	53.9	46.1
1000	10.4	48.1	223.6	54.1	45.9
1100	9.5	43.8	209.5	54.4	45.6

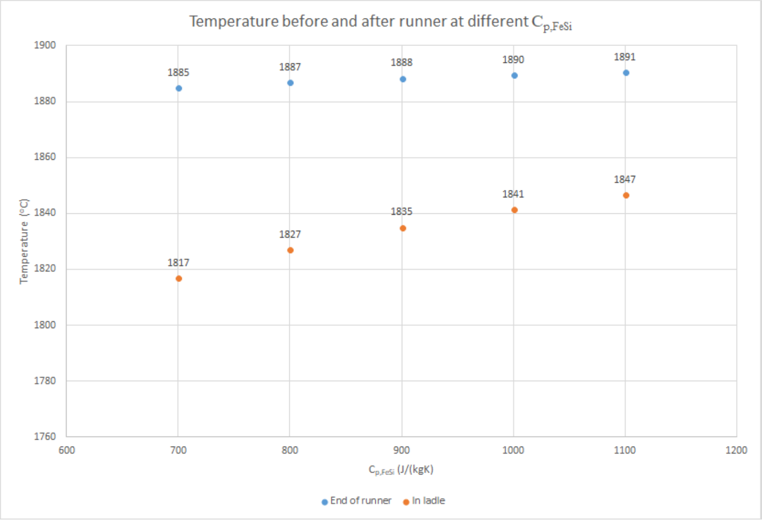

Figure 4.19: The FeSi temperature at the end of the runner (blue) and right before FeSi hits the ladle (orange) at different values for FeSi heat capacity.

FeSi that first enters the ladle will sink drastically in temperature within the first minute, but will gradually increase in temperature within the first four minutes after that because more hot FeSi is added to the ladle. As the level of FeSi in the ladle increases and more will be in contact with the ladle wall, the temperature decreases again. This trend seems to be the same for all of the 5 cases.

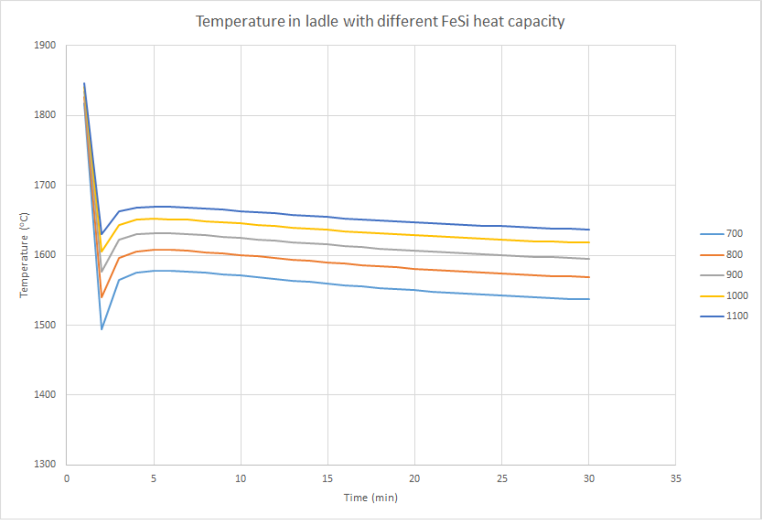

Figure 4.20: The FeSi temperature in the ladle as a function of tapping time with different values for heat capacity of FeSi.

The difference in temperature in the ladle seen in figure 4.20 for the 5 cases are caused by both the difference in start temperature of FeSi in the ladle, which again is caused by different heat loss in the runner, and because of different values for heat capacity. The latter is not significant before the heat capacity gets above 900 J/(kgK).

Table 4.10: The temperature differences in the runner (ΔT_1), when in free fall (ΔT_2), and in the ladle (ΔT_3) at different emissivity for FeSi. The total heat loss from radiation (Q_r) and convection (Q_c) from the simulated tapping sessions are also given in percentage.

ε	**ΔT_1 (°C)**	**ΔT_2 (°C)**	**ΔT_3 (°C)**	**Q_r (%)**	**Q_c (%)**
0.2	7.2	20.8	192.9	33.0	67.0
0.4	9.9	31.3	222.4	48.7	51.3
0.6	12.5	61.6	244.7	58.1	41.9
0.8	15.2	81.7	262.0	64.4	35.6
1	17.9	101.6	275.4	69.0	31.0

The results from cases where different emissivities for FeSi were applied can be found in figure 4.21 for part 1 and 2 and in figure 4.22 for part 3. For part 1 and 2 the temperatures decreases with increased emissivity, which is expected, but for part 2 the emissivity has a huge impact on the temperature because of the larger area that emits thermal radiation. A summary of the temperature differences and heat loss is given in table 4.10.

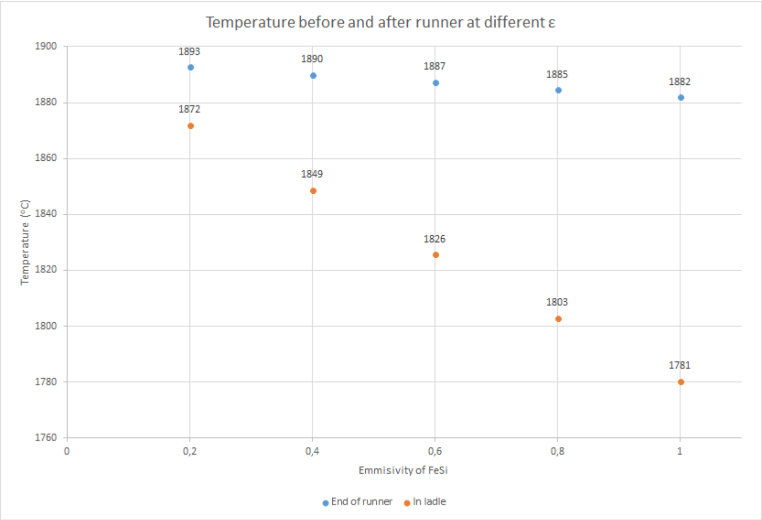

Figure 4.21: The FeSi temperature at the end of the runner (blue) and right before FeSi hits the ladle (orange) at different values FeSi emissivity.

The general trend for these 5 cases in the ladle is mostly the same as before. The large difference in temperature is somewhat caused by the difference in start temperature of FeSi in the ladle, but the end temperature in the ladle decrease when emissivity increases.

It is safe to say that radiation place a large part in the heat loss in the ladle as emissivity increases.

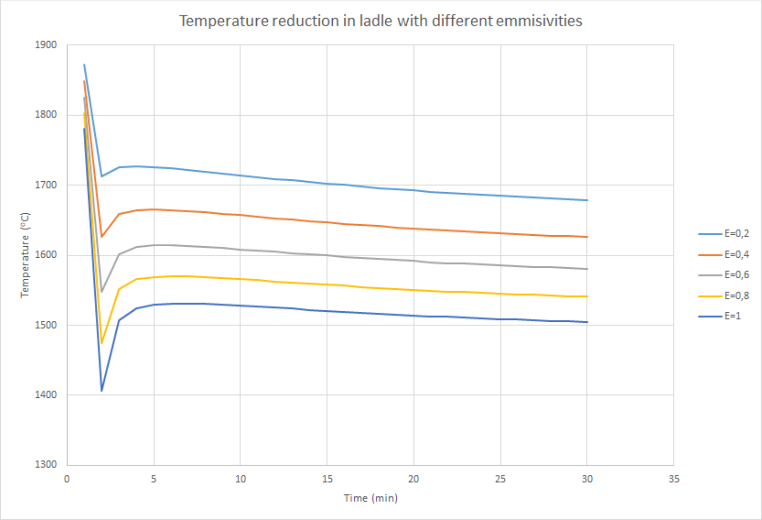

Figure 4.22: The FeSi temperature in the ladle as a function of tapping time with different values for FeSi emissivity.

The results from cases where different FeSi flow diameter were applied can be found in figure 4.23 for part 1 and part 2 and in figure 4.24 for part 3. For part 1 and 2 the temperature decreases with increased metal flow diameter. This is caused by the fact that when the mass flow rate is constant for the 5 cases the velocity of FeSi decreases with increased metal flow diameter making FeSi stay longer in these two parts. It is also caused by the increased radiation area, which is especially noticeable in part 2. However, more FeSi will also be present in the runner and in free fall when the diameter increases, and that will require more heat to be reduced in temperature. A summary of the temperature differences and heat loss is given in table 4.11.

Table 4.11: The temperature differences in the runner (ΔT_1), when in free fall (ΔT_2), and in the ladle (ΔT_3) at different flow diameter for FeSi. The total heat loss from radiation (Q_r) and convection (Q_c) from the simulated tapping sessions are also given in percentage.

d (cm)	ΔT_1 (°C)	ΔT_2 (°C)	ΔT_3 (°C)	Q_r (%)	Q_c (%)
2	4.5	20.9	245.1	49.0	51.0
4	9.0	41.4	237.9	52.4	47.6
6	13.4	61.5	230.8	55.4	44.6
8	17.9	81.3	224.0	58.0	42.0
10	22.4	100.6	217.3	60.3	39.7

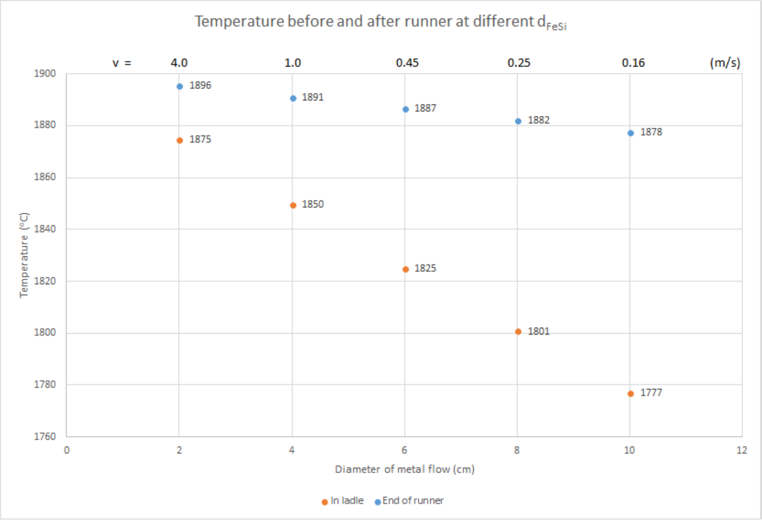

Figure 4.23: The FeSi temperature at the end of the runner (blue) and right before FeSi hits the ladle (orange) at different values for FeSi flow diameter. Velocity in m/s of FeSi is also added as a secondary horizontal axis.

The general trend for these 5 cases in the ladle is mostly the same as before. The temperature calculations in the ladle is not dependent on the FeSi flow diameter, so the only difference is the FeSi start temperature in the ladle.

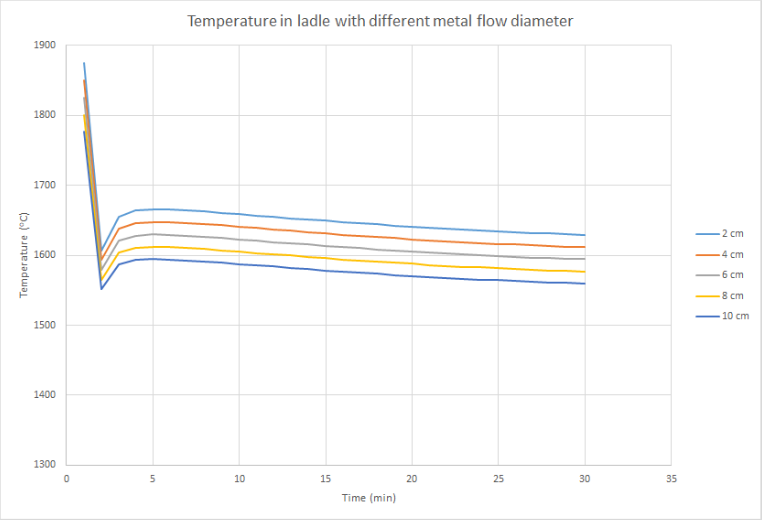

Figure 4.24: The FeSi temperature in the ladle as a function of tapping time with different values for FeSi metal flow diameter

Table 4.12: The temperature differences in the runner (ΔT_1), when in free fall (ΔT_2), and in the ladle (ΔT_3) at different mass flow rate for FeSi. The total heat loss from radiation (Q_r) and convection (Q_c) from the simulated tapping sessions are also given in percentage.

$\dot{m}$ **(kg/h)**	ΔT_1 **(°C)**	ΔT_2 **(°C)**	ΔT_3 **(°C)**	Q_r **(%)**	Q_c **(%)**
6000	15.9	72.3	271.5	57.0	43.0
7000	13.6	62.2	254.8	55.7	44.3
8000	11.9	54.7	240.7	54.5	45.5
9000	10.6	48.7	228.4	53.4	46.6
10000	9.5	43.9	217.7	52.4	47.6

The results from cases where different mass flow rate were applied can be found in figure 4.25 for part 1 and 2 and in figure 4.26 for part 3. For part 1 and 2 the temperature increases with increased mass flow rate. This is caused by the fact that when the mass flow rate increases and the FeSi metal flow diameter stays the same, the velocity will increase. This will make FeSi move more quickly from the furnace to the ladle. A summary of the temperature differences and heat loss is given in table 4.12.

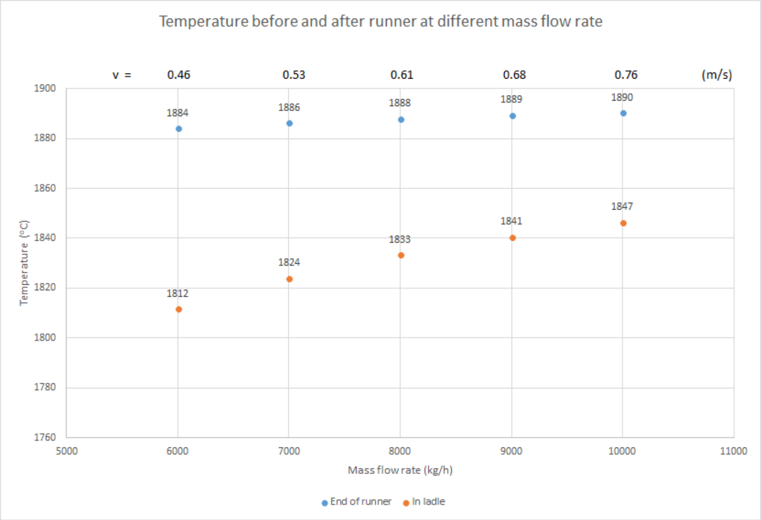

Figure 4.25: The FeSi temperature at the end of the runner (blue) and right before FeSi hits the ladle (orange) at different values for mass flow rate. Velocity in m/s of FeSi is also added as a secondary horizontal axis.

The general trend for these 5 cases in the ladle is mostly the same as before. Since the FeSi start temperature in the ladle only varies slightly, the cause for the temperature variation between these cases are mostly due to the mass flow rate. Lower flow rate will add less FeSi each iteration causing the temperature to decrease.

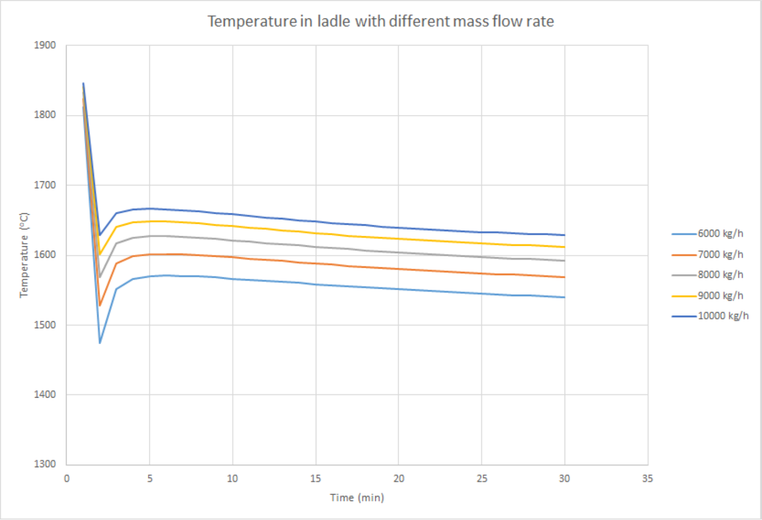

Figure 4.26: The FeSi temperature in the ladle as a function of tapping time with different values for mass flow rate

The three special cases were also investigated where the mass flow rate changes with time. The different cases were:

1. Mass flow rate starts at 10 000 kg/h and decreases with a rate of 100 kg/(h min).

2. Mass flow rate starts at 7000 kg/h and decreases with a rate of 100 kg/(h min) for 10 minutes then increases rapidly to 10 000 kg/h which then again decreases with a rate of 100 kg/(h min).

3. Mass flow rate starts at 8000 kg/h and increases with a rate of 100 kg/(h min) for 15 minutes, then decreases with a rate of 100 kg/(h min) for 15 minutes.

The results from these cases can be found in figure 4.27. Case 1 shows a more rapid decrease in temperature compared to results from figure 4.26. This is caused by less FeSi that enters the ladle for each iteration, and thus less heat is supplied to the lade. Case 2 shows an increase in temperature when the mass flow rate suddenly increases, and after that the temperature stays mostly the same for the rest of the tapping. Case 3 shows a steady temperature throughout the tapping. Even though the end temperature is the same for all of these three cases, this shows well how temperature varies throughout a tapping when mass flow rate changes with time.

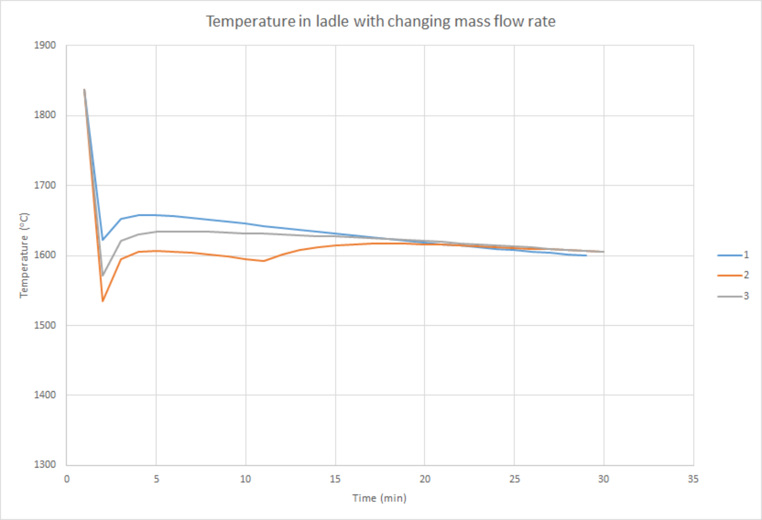

Figure 4.27: The FeSi temperature in the ladle as a function of tapping time with flow rate that changes with time.

Chapter 5

Discussion

In ferrosilicon production there is a problem with solidification of FeSi and slag in the runner and ladle during tapping of FeSi. This has been investigated by measuring the temperature in the runner and ladle during tapping sessions at a ferrosilicon production plant and heat transfer modelling. FeSi and slag samples have also been collected and analyzed for chemical composition.

During two campaigns at ferrosilicon producer Finnfjord AS the temperatures in the runner and ladle have been measured with three different thermocouples. The temperatures of FeSi in the runner was measured with C type thermocouples, and was found to vary between 1800-1920°C. The temperatures in the runner was measured right underneath the FeSi flow with two K type thermocouple, one close to the furnace and one close to the end of the runner. It was found that the temperature of the runner increased up to 850°C in the back and 800°C in the front. The mean temperature difference in the runner was found to be 111°C in the back and 212°C in the front. The temperature of FeSi in the ladle was measured with S type thermocouples, and it was found that it varied between 1650°C and 1465°C in a decreasing trend throughout tapping sessions. Several tapping sessions showed different trends than others, where some showed very low or high ladle temperatures while others seemed to increase and decrease throughout a tapping session.

Four variables were chosen for calculation of heat loss and temperature difference in the runner and ladle: heat capacity of FeSi, emissivity of FeSi, diameter of FeSi flow, and mass flow rate. A summary of the model results can be found in figure 5.1. Three special cases were also performed where mass flow rate varied to see how much the added heat from hot FeSi contributes to the temperature trend in the ladle. In the first special case the mass flow rate started high at 10 000 kg/h and steadily decreased for the duration of tapping. In this case the decrease in temperature after the 5 first minutes is more rapid than for the cases when the mass flow rate was constant. In the second special case the mass flow rate started low at 7000 kg/h and then rapidly increased after 10 minutes. In this case the temperature in the ladle increased when the mass flow rate suddenly increased after 10 minutes, and then started to decrease again at the end of the simulated tapping. In the third special case the mass flow rate started at medium level at 8000 kg/h then increased steadily for 15 minutes than decreased steadily for 15 minutes. In this case the temperature in the ladle was nearly constant and only drops 50°C after the 5 first minutes.

Table 5.1: A summery of the temperature differences in the runner (ΔT_1), when in free fall (ΔT_2), and in the ladle (ΔT_3) for the model cases. The total heat loss from radiation (Q_r) and convection (Q_c) for the simulated tapping sessions are also given in percentage.

Variables	**ΔT_1 (°C)**	**ΔT_2 (°C)**	**ΔT_3 (°C)**	**Q_r (%)**	**Q_c (%)**
700 J/(kgK)	14.9	68.0	280.2	53.2	46.8
800 J/(kgK)	13.1	59.8	258.4	53.6	46.4
900 J/(kgK)	11.6	53.3	239.7	53.9	46.1
1000 J/(kgK)	10.4	48.1	223.6	54.1	45.9
1100 J/(kgK)	9.5	43.8	209.5	54.4	45.6
0.2	7.2	20.8	192.9	33.0	67.0
0.4	9.9	31.3	222.4	48.7	51.3
0.6	12.5	61.6	244.7	58.1	41.9
0.8	15.2	81.7	262.0	64.4	35.6
1	17.9	101.6	275.4	69.0	31.0
2 cm	4.5	20.9	245.1	49.0	51.0
4 cm	9.0	41.4	237.9	52.4	47.6
6 cm	13.4	61.5	230.8	55.4	44.6
8 cm	17.9	81.3	224.0	58.0	42.0
10 cm	22.4	100.6	217.3	60.3	39.7
6000 kg/h	15.9	72.3	271.5	57.0	43.0
7000 kg/h	13.6	62.2	254.8	55.7	44.3
8000 kg/h	11.9	54.7	240.7	54.5	45.5
9000 kg/h	10.6	48.7	228.4	53.4	46.6
10000 kg/h	9.5	43.9	217.7	52.4	47.6

The FeSi samples showed very little variation in aluminum and calcium concentration throughout a tapping sessions, but varied more from session to session. Some samples within a session varied more than the others, usually at the end of tapping session, but these can be considered outliers.

The first slag samples was taken after tapping session 2585 from an iron rod the operator used to clean the runner. It was found to have a higher amount of silicon oxide compared to the amount of calcium oxide and aluminum oxide in the sample. It was found that the composition of the slag phase in the sample would give the slag a liquidus point at 1325°C, viscosity at 400 P, and density at 2.66 g/cm^3. The second slag sample was found at one of the sides of the runner after tapping session 2496. It was also found to have a higher amount of silicon oxide compared to the other components in the slag phase. It was found that the composition of the slag phase in the sample would give the slag a liquidus point at 1500°C and a viscosity at 30 P. The third slag sample was collected at the front of the runner after tapping session 2496. The slag phase had a near equal amount of silicon oxide, aluminum oxide, and calcium oxide. The liquidus point was found to be 1500°C, the viscosity was found to be 16 P, and the density was found to be 2.71 g/cm^3. The fourth slag sample was found at the bottom of the runner after tapping session 2496. It was found to contain more aluminum oxide and calcium oxide than silicon oxide, and has a liquidus point at 1475°C. The viscosity was found to be 6 P and the density was found to be 2.58 g/cm^3.

5.1 Temperature measurements and heat transfer modelling

In this chapter the temperature and heat transfer modelling will be compared with eachother. The dip measurements in the ladle with the S-type thermocouple can be categorized into four groups based on trends, events during tapping, or furnace operations as seen in figure 5.1. The normalized operational is arranged after group 1-4 in table 5.2.

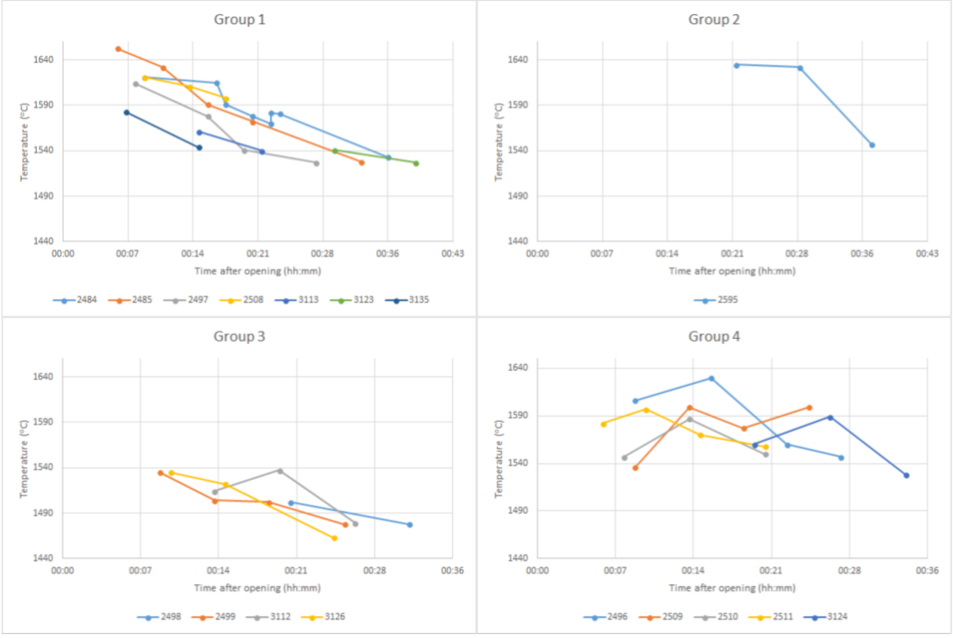

Figure 5.1: The dip measurements of the temperature in the ladle during tapping sessions can be organized in groups based on trends, events during tapping, or furnace operations

In group 1 there is a clear downward trend that starts at a high temperature and ends with low temperatures. Group 2 only contain one tapping session and and has a very high temperature late in the tapping session, but quickly reduces at the very end. Group 3 also has a downward trend, but the start and end temperatures are very low compared to temperatures recorded at other tapping sessions. The temperatures measured in tapping sessions from group 4 have no clear downward trend, but fluctuates throughout tapping sessions.

The operational data is not sufficient to explain the temperature behaviour for tapping sessions in group 1 because table 5.2 show no common ground among the data for group 1 tapping sessions. However, it was noted that during some tapping sessions the metal flow was low in the middle and end of the session. In figure 5.2 temperatures from group 1 are compared with results from the simulation case where the mass flow rate started high and decreases with 100 kg/(h min). It seemed reasonable to compare the two as it was noted that the mass flow rate seemed to decrease steadily throughout these tapping sessions. The case was also set with a FeSi emissivity at 0.5, but a higher emissivity in real life is not unlikely. During the model simulations it was also found that an increased emissivity could decrease the end temperature in the ladle drastically. It is therefore not unlikely that emissivity of FeSi is higher than 0.5. Based on the modelling and observations made during the group 1 tapping sessions it is therefore not unlikely that the temperature trends seen in group 1 is caused by a steadily decrease of mass flow rate during a tapping session.

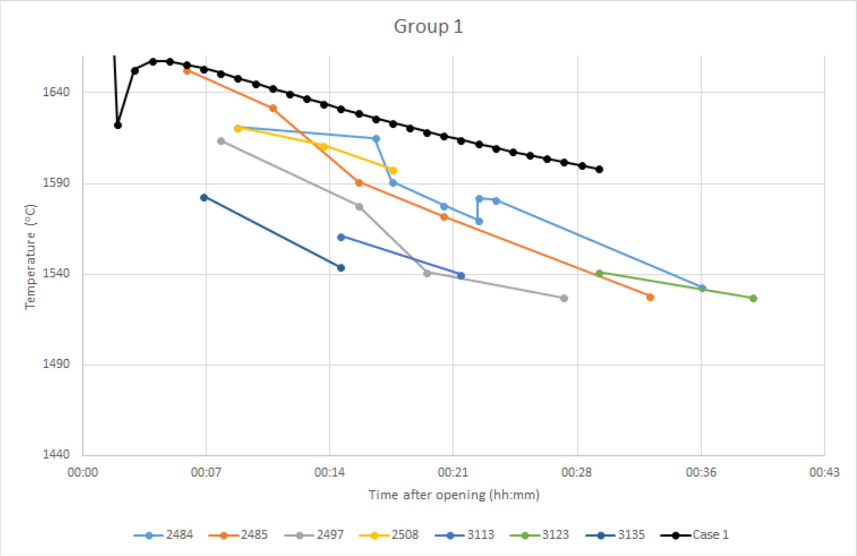

Figure 5.2: Group 1 temperatures compared with special case 1 from modelling

The temperatures recorded in group 2 can be explained by operational data. In the period before tapping started the electrical current was increased on electrode 3, which was closest to the tapping hole at that time. The power load on the furnace is also above average compared to data for the whole measuring campaign period. When the current increases through the charge in the furnace, the heat supplied to the furnace will also increase. However, an increased electrode current was also applied before a tapping session in group 1 and 3 as well, and the temperature in the ladle was much lower for these sessions. The

Table 5.2: Normalized operational data for each tapping session for group 1-4 where I 1-3 is the electrical current on electrode 1-3, power (P) is the power load on the furnace, AM 1-3 is the absolute movements of electrode 1-3, M 1-3 is the relative movements of electrode 1-3, and MF is the mass flow rate of FeSi. The first letter in the observations indicates if it was observed in the start (S), midway (M), or end (E) of the tapping. The observations are excess burning (EB), low metal flow (LMF), high metal flow (HMF), O_2 blowing (O2), and excess gassing (EG).

Gr.	Tap #	I 1	I 2	I 3	P	AM 1	AM 2	AM 3	M 1	M 2	M 3	MF	Observations
1	2484	1.00	1.01	1.01	1.04	2.27	1.30	0.67	-0.62	-0.48	1.00	0.73	M.LMF, E.EB
1	2485	0.91	0.90	0.90	0.91	0.77	0.97	0.47	-1.45	-0.24	-0.40	0.94	M.LMF, E.O2
1	2497	1.02	1.01	1.01	1.00	1.16	1.11	1.11	0.37	0.31	-0.93	1.03	Cold ladle
1	2508	1.00	1.01	0.97	1.00	1.50	0.83	1.30	1.11	0.47	-0.67	1.11	S.HMF, M.EB
1	3113	1.09	1.03	1.03	1.02	0.86	0.54	1.16	1.09	-0.38	-0.35	1.06	E.LMF
1	3123	1.02	1.03	1.02	1.02	0.90	1.04	0.76	-0.91	-1.15	-1.41	0.68	S.LMF, M.EB
1	3135	0.57	0.57	0.57	0.48	0.97	1.09	0.86	0.91	-1.54	-0.44	1.32	
2	2495	1.02	1.01	1.05	1.04	0.61	0.97	0.63	-1.45	0.94	.0.67	1.00	
3	2498	1.02	1.01	1.00	1.03	1.07	1.04	1.07	0.93	1.41	-0.80	1.00	S.LMF, S.EG
3	2499	1.02	1.01	1.01	1.04	1.40	0.97	0.89	-0.10	-1.20	-1.47	1.07	S.HMF
3	3112	1.07	1.03	1.02	1.09	1.48	0.72	1.34	-1.52	-1.54	-1.76	0.68	S.O2, M.LMF, M.EB
3	3126	1.02	1.03	1.03	1.02	0.97	0.59	1.27	-0.15	0.00	1.00	0.99	S.HMF
4	2496	0.96	0.96	1.00	0.96	1.59	0.94	0.89	0.65	-0.72	-1.33	0.97	M.EB
4	2509	0.99	1.04	1.00	0.98	1.25	0.68	0.90	-1.34	-1.92	-0.93	1.03	M.EG, E.O2
4	2510	0.99	1.04	0.97	0.95	2.04	0.89	0.54	1.94	-1.44	-0.53	0.99	M.O2, E.LMF
4	2511	1.00	1.02	0.96	0.95	0.86	0.83	0.60	-1.03	1.88	-2.27	0.86	S.EG, M.HMF
4	3124	1.03	1.01	1.01	0.96	0.84	0.87	1.28	-0.30	-0.38	-0.71	1.12	S.O2

temperature in the runner for tapping session 3113 in group 1 was also low compared to what one might expect with an increased current, and was measured to be around 1850°C. If the electrode were further away from the tapping hole in an area where the resistance in the charge was low could explain the low temperatures recorded for these tapping sessions. It is therefore concluded that the temperature trend seen in group 2 could be explained by the increases of electrode current.

In group 3 there are no major consistency in the operational data, observations, and the tapping sessions, other than large absolute movement for electrode 1 and 3. Since the temperature of FeSi in the runner was 1800°C for tapping session 3126, which is very low compared to other tapping sessions, it is possible that the low temperature in the ladle must be explained by conditions in the furnace. In tapping session 3112 a higher current was also applied on electrode 1, but this did not increase the ladle temperature as it did for the tapping session in group 2. Since the electrode was closer to the tapping hole in the tapping session in group 2, it is possible that the condition of electrodes further away from the tapping hole does not contribute a lot to the temperature out of the furnace. The operational data also shows that there is a downwards trend for electrode 3, but this is the case for most tapping sessions in all groups so it is not sufficient for explaining the low temperatures found in group 3. There were also a lot of work going on in the runner, like excess burning and blowing with oxygen, it is therefore possible that a combination of low temperatures out of the furnace and disturbances in the FeSi flow during tapping creates low ladle temperatures. Why the FeSi temperature is low out of the furnace is uncertain.

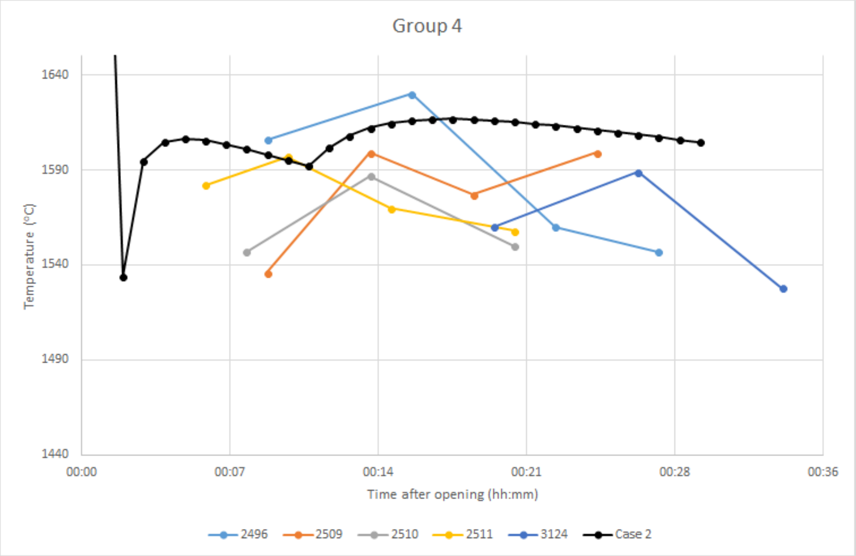

Figure 5.3: Group 4 temperatures compared with special case 2 from modelling

The temperatures recorded in group 4 also show no consistency when it comes to the operational data. However, it was noted that a lot of work going on in the runner during these tapping sessions, and that there were some blowing with oxygen. In tapping session 2511 it was also noted that a high metal flow occurred midway through the tapping. It is possible that the sudden increase in metal flow in the middle of a tapping session can increase the temperature in the ladle. In figure 5.3 temperatures from group 4 are compared with results from the simulation case where the mass flow rate is lower in the beginning, but drastically increases after 10 minutes. It seemed reasonable to compare the two as it was noted that there were a lot of work in the runner during these tapping sessions that could disturb the mass flow rate. This involves burning in the runner, O_2 blowing in the tap hole, and gas blowing from the tap hole. Of course, in the cases of O_2 blowing the oxygen can react with different metal components in FeSi like aluminum and calcium and create oxides. These reactions are exothermic and will release energy which can increase the temperature of FeSi. However, it is also shown through the special case 2 simulation that the heat supplied from new metal in the ladle also can contribute greatly to a change in FeSi temperature in the ladle. It is therefore concluded that both the change of mass flow rate and blowing with oxygen can contribute to the temperature trend seen in group 4.

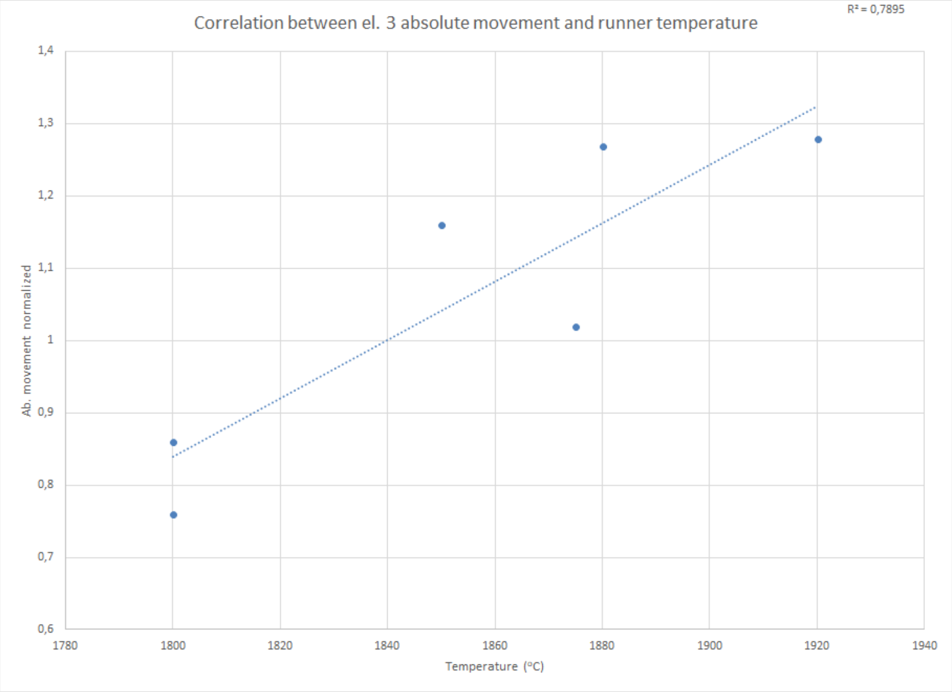

Figure 5.4: Correlation between absolute movement of electrode 3 with FeSi temperature in the runner.

It has already been discussed on how furnace operations can impact the FeSi temperatures found in the runner. This has been investigated by plotting the temperature against the different operational data. Since the electrical current applied to the electrodes and the power varied very little during the campaigns, what was of most interest was the movements of the electrode and if they influenced the temperature out of the furnace. What was found was that the absolute movement of electrode 3 correlate well with FeSi temperature in the runner as seen in figure 5.4. The movements and absolute movements of the other electrodes did not correlate at all with the runner electrodes. The position of the electrode relative to the tapping hole might therefore be crucial to whether or not the movements of the electrode will influence the temperature out of the furnace.

The temperature was also measured across the ladle during tapping session 2484. The result showed no large differences in temperature between the different measuring points except for one point that deviates from the other. The even temperature in the ladle can be caused by the high amount of heat convection that can occur at these temperatures so that the transport of heat causes the temperature to even out very fast. Measurements across the ladle was only done once so more measurements like these has to be done before any real conclusions can be drawn, but for now it seems like there is very little differences in temperature across the ladle.

Another observation was that the temperature of FeSi in the runner was 300^oC higher than in the ladle. The temperature in the flow was also measured to be between 20^oC to 70^oC higher than the ladle temperature. From model calculations it was found that the temperature only decreased up to 120^oC from the furnace to the ladle. It was also shown through the model simulations that the temperature decreased rapidly in the moment new FeSi hits the "cold" ladle. It is not unreasonable to think that convection within the liquid FeSi happens very fast so that temperature is very much uniform at all times, and that could be the cause for the large temperature difference between FeSi in the runner and FeSi in the ladle. This is also supported by the measurements done across the ladle, where temperatures varied very little. It is also worth noting that several measurement done directly from the stream resulted in a failure, and only the highest temperature was recorded before the thermocouple broke. It is therefore not unlikely that the temperature in the stream could be as high as 1800^oC, as the simulations showed.

The K-type thermocouples in the runner measured lower temperatures than what was expected. It was expected that conduction in the carbon block would be very high as hot FeSi ran over it because of the high thermal conductivity of carbon. According to theory, K-type thermocouples should not measure temperatures lower than 500° because of non-linear relationships between the measured emf and temperature under that value. It is therefore possible that temperatures measured under 500° are not reliable.

A crucial component for the heat transfer calculations done in the model is the heat transfer coefficient, h_c. The heat transfer coefficient was estimated by the use of three different techniques. The first estimation was done by using equation 2.18 and resulting in h_c = 38 373 W/(m^{2}K). The second estimation was done by using equation 2.18 and resulted in h_c = 7.8 W/(m^{2}K) in the runner and h_c = 10.6 W/(m^{2}K) in the ladle. The third estimation was done by calculating how much heat is required to heat up the runner and from there calculate h_c, and this resulted in h_c = 131 W/(m^{2}K). The reason for the large difference in heat transfer coefficient by the use of the different estimation techniques might be because it was assumed that all heat is transferred to the refractory material in the ladle without resistance and instantly heats it up. This might not be the case in real life if the thermal conductivity of the solid material is lower than the heat transfer coefficient. This will cause a bottleneck at the wall while heat is transported through the material. In other words, the heat transfer coefficient might be very high, but it does not really matter if the thermal conductivity of the refractory material is very low. This is the case for common refractory materials like aluminum oxide and silicon oxide, and it is also the reason why they are used as heat insulating materials. The heat transfer coefficient also depends on the geometry of the system, and equation 2.19 is based on heat transfer between liquids and a solid plate. This is not the case in the runner and ladle, which have cylindrical geometries. The heat transfer coefficient found by estimation method 3 was most promising because it included the assumptions mentioned earlier and the geometry of the system, and was therefore used for further calculations.

From all the cases done in the modeling, emissivity had the largest impact on temperature in both runner and ladle. It was reported by Takasuka et al. (1997) and Goett et al. (2013) that the emissivity of liquid silicon and steel is quite low, 0.25 and 0.2 respectively. Since thermal radiation only counted to 33 % of the total heat loss at $\varepsilon = 0.2$, it is uncertain if thermal radiation is the major mechanism of heat transfer during a real tapping situation. However, it was also reported that slag on top of a steel surface can increase the emissivity up to 0.35 at 1900°C. At $\varepsilon = 0.4$ the thermal radiation was 48.7 % of the total heat loss and the temperature would be 30°C less than for emissivity at 0.2. Slag on top of FeSi in the runner might not be a major concern because of the minor amounts thats tapped, but slag will accumulate in the ladle as more and more FeSi is tapped. However, temperatures in the ladle was measured to be lower than the calculated ladle temperatures with emissivity at 0.2 and 0.4. Either other factors contributes to reduction of ladle temperatures, or more accurate calculations must be made where conduction in the ladle also is taken into account.

In the model simulation the heat capacity was allowed vary between 700 J(kgK) and 1100 J/(kgK). The heat capacity of ferrosilicon was calculated based on heat capacity of iron and silicon found by HSC Chemical 9 and by assuming no volume expansion. This resulted in a heat capacity for ferrosilicon at 932 J/(kgK). In HSC Chemical 9 liquid silicon is given only one value, and iron varies only with 70 J/(kgK) from 1000°C to 2000°C. So it is possible that the heat capacity does not vary much with temperature for liquid ferrosilicon and does not play an important role in the heat loss during tapping.

In the model simulations where the diameter of FeSi flow varied from 2 cm to 10 cm the velocity of FeSi also varied from 4.0 m/s to 0.16 m/s when the mass flow rate was held constant at 8500 kg/h. It was not really the diameter that was the major variable, but the velocity of FeSi because less time is spent in the runner and in free fall with high FeSi velocity. With high velocity less heat is lost in the runner and in free fall, but in the ladle the heat loss will be the same for all of these cases. When the mass flow rate is changed the velocity also changes when the diameter is constant, but in a less degree than when the diameter varied. As discussed previously the change in mass flow rate can impact the temperature in the ladle greatly because of the added heat from new and hot FeSi that enters the ladle.

5.2 FeSi and slag samples

During the two campaigns FeSi and slag samples were collected and analyzed for chemical composition. The impurity elements aluminum and calcium in the FeSi samples are of most interest because it can give a clue about the temperature in the furnace since aluminum and calcium require higher temperatures to be reduced from aluminum oxide and calcium oxide. From theory presented in chapter 2 it is known that the amount of aluminum and calcium in FeSi is dependent on temperature because the equilibrium constants for the reactions depends on temperature. However, from figure 5.5 it can be seen that neither aluminum nor calcium correlates with temperature of FeSi in the ladle. The temperature that is correlated with the calcium and aluminum concentration is the ones that were taken with the S-type thermocouple in the ladle where the metal sample and temperature was taken consecutively.

It has been discussed in the previous chapter that the ladle temperatures can be effected by many things, including emissivity, mass flow rate and the diameter of FeSi flow. It might be more relevant to compare the runner temperature with the concentration of aluminum and calcium concentration in the samples because it might be more representative to the temperature in the furnace where aluminum oxide and calcium oxide is reduced. This has been done in figure 5.6 where the mean aluminum and calcium concentration in the tapping session where C type thermocouples have been used to measure the temperature in the runner. However, not even the temperature in the runner shows correlation with aluminum and calcium concentrations in FeSi samples.

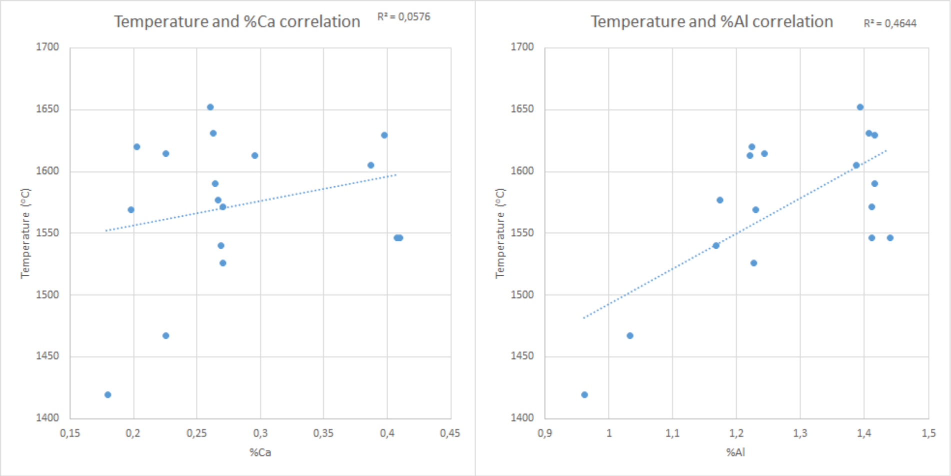

Figure 5.5: Correlation between temperature and aluminum content, and temperature and calcium content in the FeSi samples.

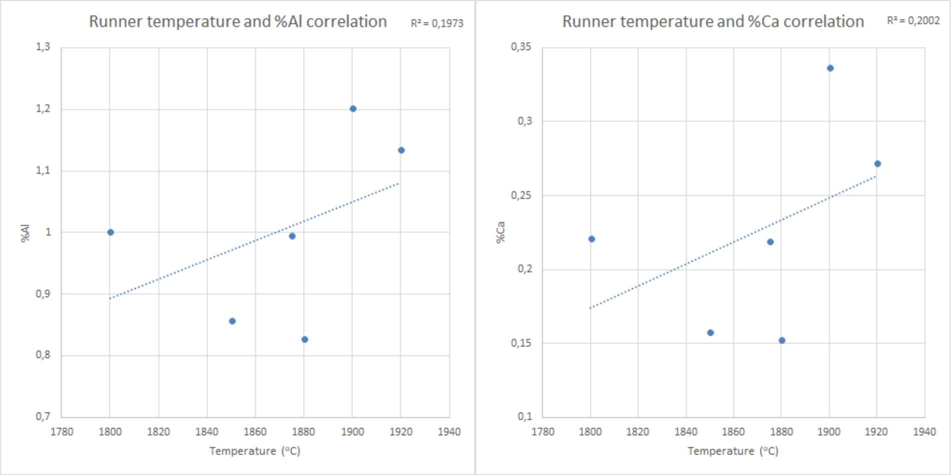

Figure 5.6: Correlation between runner temperature, aluminum and calcium concentration in FeSi samples.

Because of these results one might ask how much do temperature affect the concentration of aluminum and calcium in FeSi. By calculating the ideal concentration of aluminum and calcium according to equation 2.9 and 2.10 the temperature dependency for aluminum and calcium in FeSi can be seen. This is presented in figure 5.7.

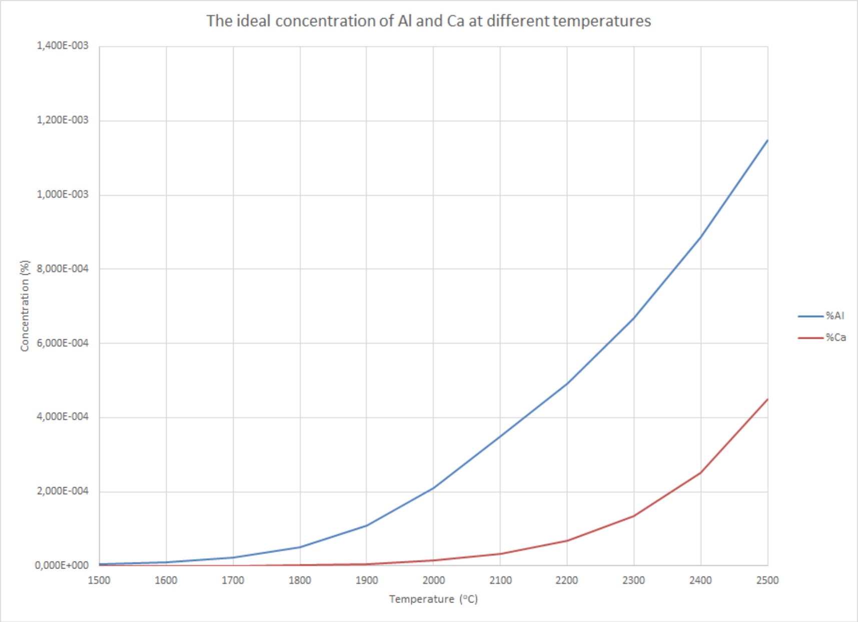

Figure 5.7: The variation of ideal concentration of aluminum and calcium in FeSi with temperatures.

In an ideal mixture the activity coefficient for a substance x, γ_x, equals 1. It has been assumed that there is 75 % silicon in the metal phase, and the slag phase has a composition of 29.1 % Al_2O_3, 25.9 % CaO, and 45 % SiO_2 which is the mean composition of the slag samples found in chapter 4. The equilibrium constant at different temperatures has been calculated with HSC Chemical 9. From these calculations it was found that the ideal concentration in FeSi is very low at all temperatures compared to what has been found, but equilibrium conditions may not apply to the conditions in a real furnace. Nevertheless, the concentrations increases rapidly at temperatures above 1800°C for aluminum and at temperatures above 2100°C for calcium. It is believed that temperatures in the furnace is around 2000°C, so it is possible that the temperatures does not affect the concentration of aluminum and calcium as much as the composition of the slag and FeSi phases.

However, some trends between temperature and the concentrations of aluminum and calcium is evident as figure 5.8 shows. In this figure low temperatures in the ladle shows low concentrations of aluminum and calcium (green), medium temperatures shows meadium concentrations of aluminum and calcium (orange), and high temperatures show high concentrations of aluminum and calcium (yellow).

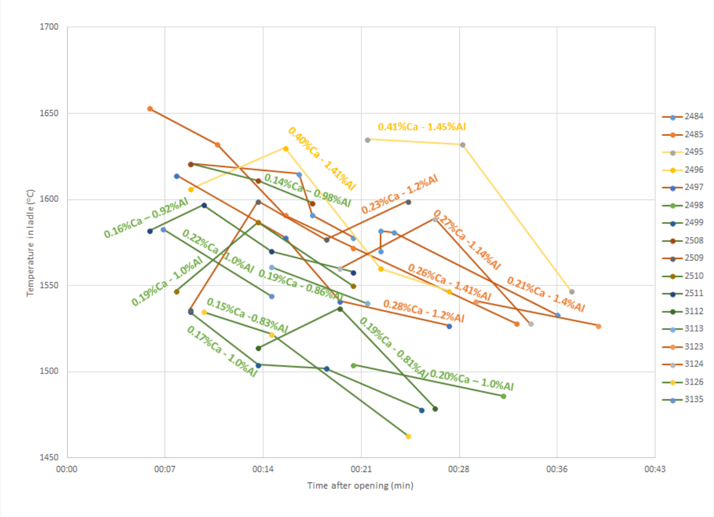

Figure 5.8: Temperatures measured in the ladle compared with mean aluminum and calcium content for each tapping session. Green is low concentrations, orange is medium concentrations, and yellow is high concentrations.

Another way to check if aluminum or calcium correlates with temperature is to check if they correlate with one another. According to equation 2.9 and 2.10 aluminum and calcium does not depend on one another because their concentration in the FeSi phase is very low compared to silicon and iron. Previous findings have shown that aluminum and calcium concentrations correlates very well, but in figure 5.9 shows that this is not the case here.

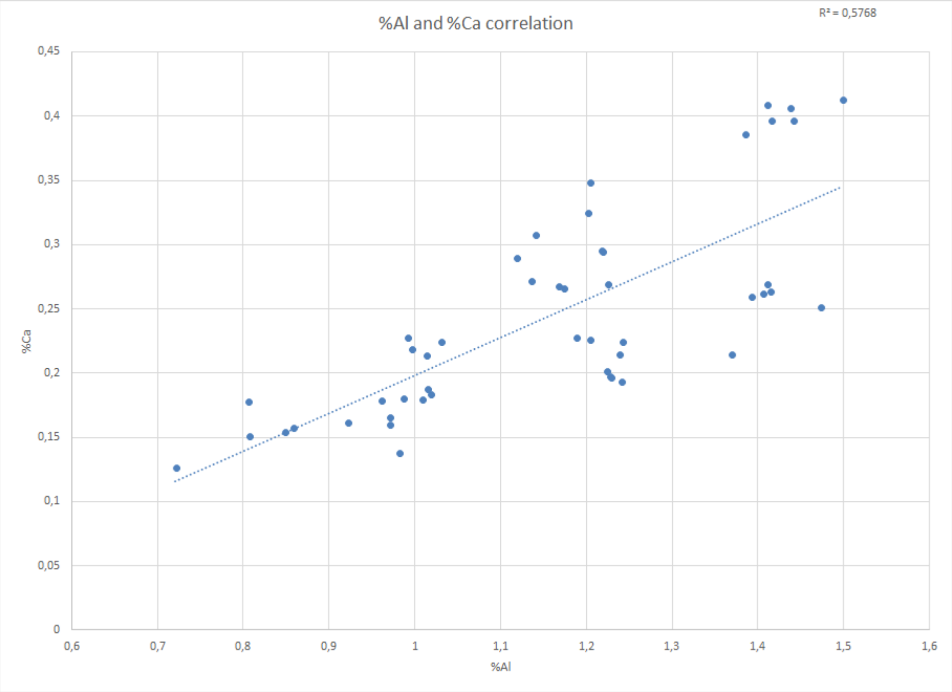

Figure 5.9: Correlation between aluminum and calcium content in the FeSi samples.

To explain this behaviour the correlation plot in figure 5.9 has been split to show the correlation from samples taken in the first campaign and second measuring campaign as seen in figure 5.10. The correlation between aluminum and calcium in the first campaign still show a very poor correlation, while in the second campaign the correlation is very good and is in line with previous findings. As discussed previously, the reason for change in aluminum and calcium concentration could be change in temperature, FeSi composition, and slag composition. From information given by Finnfjord AS it was found that coke and coal was added to the furnace in excess to the normal recipe throughout the first measuring campaign, while no extra carbon materials were added in the second measuring campaign. Since coke and coal can contain different amounts of calcium oxide and aluminum oxide, and these carbon materials where added in different amount at different times, it is possible that this can play a part in the amount of calcium and aluminum that ends up in the metal. So in periods where no extra carbon materials are added to the furnace the slag and metal phase is fairly constant, and the temperature in the furnace is main factor that changes the calcium and aluminum concentrations in FeSi. In periods where extra carbon material is added to the furnace the change of composition in the slag phase may be the main factor that determines the concentration of aluminum and calcium.

Slag samples were collected from tapping session 2585 from an iron rod used by operators and from tapping session 2496 at different places in the runner. The slag sample from the iron rod (sample 1) was found to have a higher amount of silicon oxide than the other samples. Sample 1 was also found to be more viscous than the other slag phases found on sample 2-4. Viscous slag during tapping sessions is a reported problem during tapping of both ferrosilicon and silicon furnaces, and it is believed that this slag is mostly silicon oxide. It can clog up the tapping hole and stick to equipment used by operators. Less viscous slag was found further down the runner, so it seems like the viscosity of the slag is important to reduce the amount of slag clogging up the tapping hole. If the intention is to tap all slag into the ladle together with FeSi addition of calcium oxide can increase the basicity of the slag and thus reduce its viscosity. However, further studies are needed to fully understand the interaction between slag and FeSi during tapping of ferrosilicon furnaces.

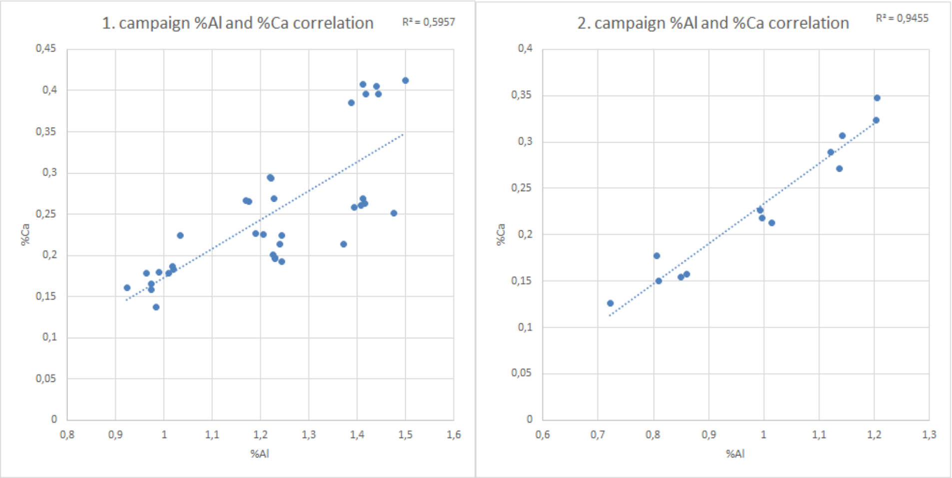

Figure 5.10: Correlation between aluminum and calcium content in the FeSi metal samples for campaign 1 and 2.

Chapter 6

Conclusion

In ferrosilicon production there is a problem with solidification of FeSi and slag in the runner and ladle during tapping of FeSi. This has been investigated by measuring the temperature in the runner and ladle during tapping sessions at a ferrosilicon production plant and heat transfer modelling. FeSi and slag samples have also been collected and analyzed for chemical composition.

Dip measurements of temperature with S-type thermocouples have been performed in the ladle, and it has been concluded that the measurements from each session can be categorized in four groups based on trends, events during tapping, and furnace operations. The temperature seemed to follow a general downward trend for each tapping session, and the groups had the following characteristics:

- Group 1 showed a steady decrease of temperature over time. A factor that may affect temperatures in group 1 is a steady decrease of mass flow rate throughout the tapping.
- Group 2 showed high temperatures in the ladle late in the tapping session. A factor that may affect temperatures in group 2 is an increase of electric current on the electrodes.
- Group 3 shows low temperatures in the ladle during tapping sessions. Factors that may affect temperatures in group 3 are movements of the electrodes and unsteady mass flow.
- Group 4 shows fluctuating temperatures throughout tapping sessions. Factors that may affect temperatures in group 4 are fluctuations in mass flow rate throughout the tapping and blowing of O_2.

The temperature in the runner was measured with C type thermocouples and was found to vary between 1760°C and 1920°C. The temperature in the runner may depend on movements on the electrodes, especially the electrode closest to the tapping hole. The temperature in the runner and ladle was also found to differ up to 300°C. The heating up of the ladle found through modelling and fast convection causing uniform FeSi temperature within the ladle can be an explanation of that.

The estimation of heat transfer coefficient, h_c, used in the modeling varied greatly from 7.8 W/(m^2K) to 38 373 W/(m^2K). A reason for this could be that h_c could be really high, but if the solid material that is going to conduct the heat has a low thermal conductivity k, which is the case for refractory materials, a bottleneck will be created at the wall because heat will not be transported through the material fast enough. The geometry of the system also plays a large part in calculating h_c, and estimation methods are often based on general geometries like flat surfaces or tubes. For these calculation purposes the heat transfer coefficient calculated based on measurements done in this study was used.

The emissivity of FeSi plays a large part in heat transfer calculation because large areas are suspect to thermal radiation. However, previous findings suggest that the emissivity of FeSi could be very low. This can greatly lower the amount of heat that is lost due to thermal radiation. However, previous finding also suggest that slag on top of liquid metal can increase the emissivity, and this might be the case for tapping of FeSi.

In the modelling heat capacity was varied between 700 J/(kgK) and 1100 J/(kgK), but in reality heat capacity of liquid FeSi may vary with temperature in only a small degree compared to what was done in the model. The variation in heat capacity with temperature may not contribute in a large degree to the total heat loss and temperature decrease during tapping of FeSi.

Model cases was also done by varying the diameter of FeSi flow, but with a constant mass flow rate. This results in lower FeSi velocity and larger area which thermal radiation occurs decreasing the temperature further in the runner and when FeSi is in free fall. The decrease in velocity may contribute more to the heat loss in the runner than larger thermal radiation area. Cases were also done where mass flow rate was changed, and with a constant FeSi flow diameter. Also here the velocity decreases with decreasing mass flow rate. Higher mass flow rate may also be important because it contributes a great deal to heat flow going in to the ladle which again contributes to increasing the temperature in the ladle during the first five minutes of tapping.

Aluminum and calcium concentrations in FeSi varies very little during a tapping session with only a few outliers. It was aslo found that aluminum and calcium concentrations does not correlate with either ladle nor runner temperatures of FeSi, but there are some trends suggesting that low concentrations of of aluminum and calcium are present in FeSi where the measured ladle tempertaures are low and high concentrations of aluminum and calcium are present in FeSi where the measured ladle temperatures are high. It also seems like addition of carbon materials to the furnace in excess to the normal recipe also impact the amount of aluminum and calcium that ends up in FeSi.

Four slag samples were also collected after some tapping sessions and it was found that high viscosity slag with high amounts of silicon was found just around the tapping hole and sticks to equipment used by operators. This is a reported problem found in ferrosilicon and silicon industry that high viscosity slag clogs up the tapping hole. Low viscosity slag was found further down the runner, and it seems that only this type of slag can find its way down to the ladle. However, further studies are needed to fully understand the interaction between slag and FeSi during tapping of ferrosilicon furnaces.

Bibliography

Beckhoff, B., Kanngiesser, B., Langhoff, N., Wedell, R., Wolff, H., 2006. Handbook of Practical X-ray Fluorescence Analysis. Springer Berlin Heidelberg.

Bel'tyukov, A., Lad'yanov, V., Shishmarin, A., 2014. Viscosity of fe-si melts with silicon content up to 45 at %. High Temperature 52 (2), 185–191.

Brandes, E. A., Brook, G. B., Smithells, C. J., 1999. Smithells metals reference book. Butterworth-Heinemann.

Goett, G., Kozakov, R., Uhrlandt, D., Schoepp, H., Sperl, A., 2013. Emissivity and temperature determination on steel above the melting point. The International Journal of Materials Joining 57 (4), 595–602.

Hjelen, J., 1986. Scanning elektron-mikroskopi.

HSC, 2018-05-08. Outotec. V. 9.2.3.
URL `https://www.outotec.com/products/digital-solutions/hsc-chemistry/`

Hustad, H. M., Tangstad, M., 2017. The effect of fe$_x$o$_y$ on different al$_2$o$_3$-cao-sio$_2$ slag systems, specialization project at Department of Material Science and Engineering, NTNU.

Jimbo, I., Cramb, A., 1993. The density of liquid iron-carbon alloys. Metallurgical Transactions B 24 (1), 5–10.

Kobatake, H., Fukuyama, H., Minato, I., Tsukada, T., Awaji, S., 2007. Noncontact measurement of thermal conductivity of liquid silicon in a static magnetic field. Applied Physics Letters 90 (9).

Ksiazek, M., Hustad, H. M., Nymoen, A., Holta, J., Grdal, S., Tangstad, M., 2018. Metal temperature measurements during tapping of fesi industrial furnace.

Langen, M., Hibiya, T., Eguchi, M., Egry, I., 1998. Measurement of the density and the thermal expansion coefficient of molten silicon using electromagnetic levitation. Journal of Crystal Growth 186 (4), 550–556.

McGrath, T. D. H., White, J. F., Downey, J. P., 2014. Experimental determination of density in molten lime silicate slags as a function of temperature and composition. Mineral Processing and Extractive Metallurgy 123 (3), 178–183.

Pollock, D. D., 1991. Thermocouples: theory and properties. CRC Press.

Rhim, W. K., Ohsaka, K., 2000. Thermophysical properties measurement of molten silicon by high-temperature electrostatic levitator. Journal of Crystal Growth 208 (1), 313–321.

Rosenqvist, T., 2004. Principles of extractive metallurgy. Tapir Academic Press.

Schei, A., Tuset, J. K., Tveit, H., 1998. Production of high silicon alloys. Tapir.

Schuhmann, R., 1952. Metallurgical Engineering. Addison-Wesley.

Shimizu, T., Matsuura, K., Furue, H., Matsuzak, K., 2013. Thermal conductivity of high porosity alumina refractory bricks made by a slurry gelation and foaming method. Journal of the European Ceramic Society 33 (15-16), 3429–3435.

Takasuka, E., Tokizaki, E., Terashima, K., Kimura, S., 1997. Emissivity of liquid silicon in visible and infrared regions. Journal of Applied Physics 81 (9), 6384–6389.

VDEh, 1981. Slag Atlas. Verlag Stahleisen.

Yefimets, A. M., Tesleva, E. P., Solovyan, A. V., 2015. Influence of boric anhydride upon physical and chemical properties of ferrosilicon slag. IOP Conference Series: Materials Science and Engineering 91 (1), 012049.

Zhang, G., Chou, K., 2013. Influence of al2o3/sio2 ratio on viscosities of cao-al2o3-sio2 melt. ISIJ Int. 53 (1), 177–180.

Appendix A

FeSi and slag experiments

Experimental

Three experiments will be carried out to better understand how slag end FeSi interacts with one another during a simulated tapping situation at different temperatures. This chapter will explain which raw material and instruments were used, the experimental setup, and the method for carry out the experiments.

Raw materials and instruments

The FeSi used in the experiments were provided by industry and contains roughly 75 % silicon and 25 % iron. The slag was made synthetically. The raw materials for making the slag were 99.95 % CaO, 99.5 % SiO_2 , and 99.95 % Al_2O_3, all in powder form. The purity is based on the metal content of the material. The grain size of the CaO and SiO_2 powder was stated by the supplier to be less than 10 micron, and the grain size for Al_2O_3 was stated by the supplier to be between 0.25-0.45 micron. Trace element distribution in the CaO, SiO_2, and Al_2O_3 powders was not given by the supplier.

The induction furnace used in the experiments is a small scale smelting apparatus with a maximum power of 75 kW. It is capable of reaching temperatures up to 2000 °C, most because of insulation and cooling complications. The induction furnace used at the Department of Material Science and Engineering at NTNU is illustrated in figure A.1. The sample is mounted in a cylindrical graphite crucible with diameter and height at 15 cm and 40 cm respectively.

Figure A.1: The induction furnace ”IF75” furnace at the Department of Materials Science and Engineering.

The furnace does not supply heat itself, but rather heats up the electrical conductive graphite crucible by eddy currents. These currents are induced by changing the magnetic fields in the graphite crucible which heats it up. The important components in an induction furnace are thus an electromagnet and an electronic oscillator which have the task of changing the magnetic field in the conductive crucible and thus inducing the eddy currents. The IF75 furnace has an electronic oscillator that oscillates at a frequency of 3kHz.

Three cameras were used to record the experiments: A mobile phone, a high speed camera, and a infrared camera. The camcorder on the phone records colored images with 1920x1080 pixels resolution with a frame rate at 60 fps. The high speed camera can record colored images with a long range of different resolutions and frame rates and can record images with frame rates as high as 109,500 fps, but at reduced resolution. The highest resolution can be set at 1024x1024 with a frame rate as high as 1000 fps. The global shutter speed for the high speed camera can be as high as 2 μs, independent on the frame rate selected.

Figure A.2: From left to right: The phone camera, high speed camera, and infrared camera used in the experiments.

The infrared camera can record images with a 640x480 resolution, and can measure temperatures from 0-2000°C with 2 % deviation. The spectral range is from 7.5 to 13 μm. The camera can record single frames and sequential frames up to 30 fps. Before recording can start a temperature range must be applied based on the expected temperature of the film object. Different color spectres can also be applied based on the camera operators preferences.

Experimental procedure

The experiments will be carried out by melting FeSi and slag together in a graphite crucible in an induction furnace. FeSi (1000 g, 75 vol. %) and slag (270 g, 25 vol. %) are weighed in a graphite crucible with a thermocouple as seen in figure A.3. The thermocouple will measure the temperature in the crucible through out each experiment. The composition of the slag used was 7.7 % Al_2O_3, 44.2 % CaO, and 48.1 % SiO_2. This slag was chosen because of its low liquidus point and low viscosity. The density of the slag is also low compared to FeSi, resulting in the slag floating on top of FeSi when both are in a liquid state.

Before the experiments started the camera was set in place, turned on, and camera settings applied. The graphite crucible with slag, FeSi, and thermocouple was then placed in the induction furnace and the furnace was turned on. The crucible was heated up to a certain temperature, given for each experiment in table A.1, and held there for around 20 minutes to make sure all the content in the crucible had melted. When FeSi and slag had melted the tapping simulation started. This was done by two people together lifting and pouring out the content in the crucible out into a graphite casting mold at a slow pace. The tapping procedure was recorded with the camera. A summary of the experiments can be found in table A.1. The infrared camera was used for experiment 1 and was set to record sequential frames with a frame rate at 30 fps and with a temperature range at 200-2000°C. The high speed camera was used for experiment 2 and was set to record with a frame rate at 150 fps at 1024x1024 resolution. The phone camera was used for experiment 3 and was set to record with a frame rate at 60 fps at 1920x1080 resolution.

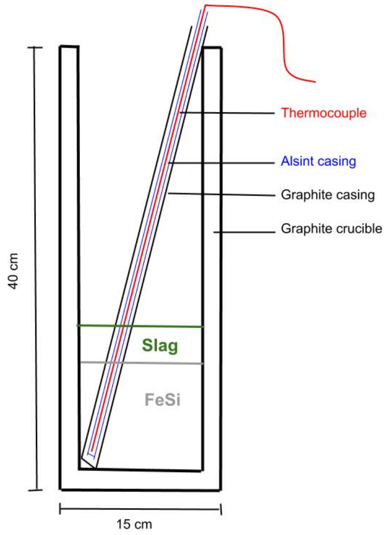

Figure A.3: The experimental setup.

Table A.1: A summary of the experiments performed.

Experiment	m$_{FeSi}$ (g)	m$_{slag}$ (g)	Temperature (°C)	Camera
1	1000	270	1600	Infrared
2	1000	270	1700	High Speed
3	1000	270	1800	Phone

Results

The results from the experiments will be presented in this section. In experiment 1 slag and FeSi was heated up to 1600°C and was recorded with an infrared camera. In experiment 2 slag and FeSi was heated up to 1700°C and was filmed with a high speed camera. In exeriment 3 slag and FeSi was heated up to 1800°C and was filmed with a phone camera.

Experiment 1

In experiment 1 slag and FeSi was heated up to 1600°C, and the simulated tapping session was filmed with an infrared camera. The temperature log for the experiment is found in figure A.4.

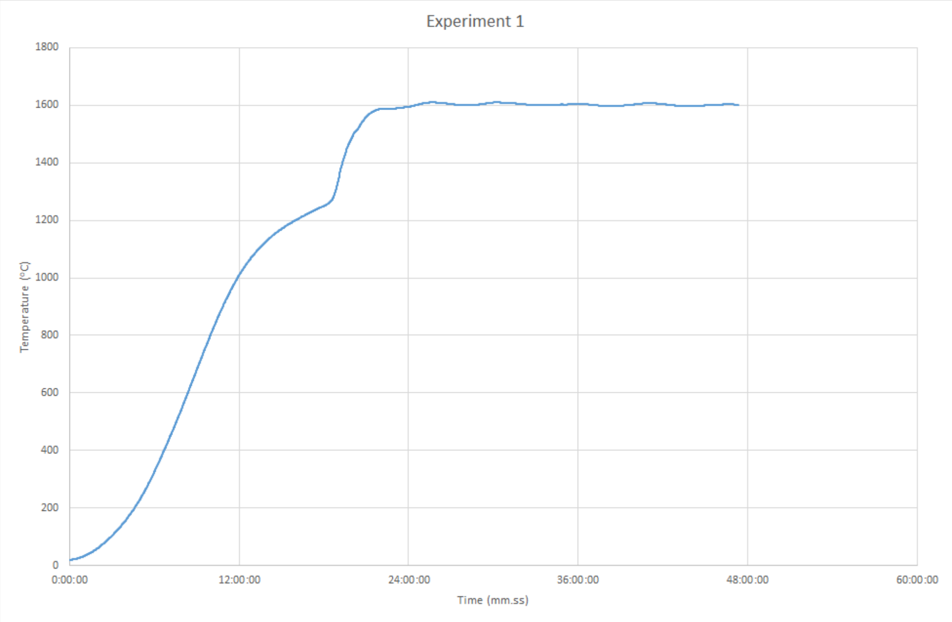

Figure A.4: The temperature log for experiment 1.

A still photo for every 3rd second of the simulated tapping session in experiment 1 can be found in figure A.5. Ferrosilicon seem to be tapped first for the first 9 seconds, and than the bulk of the slag is tapped in the last 6 seconds. The slag is very viscous so it takes some additional seconds to clear it out of the crucible. The temperature decreases fast as the content leaves the crucible.

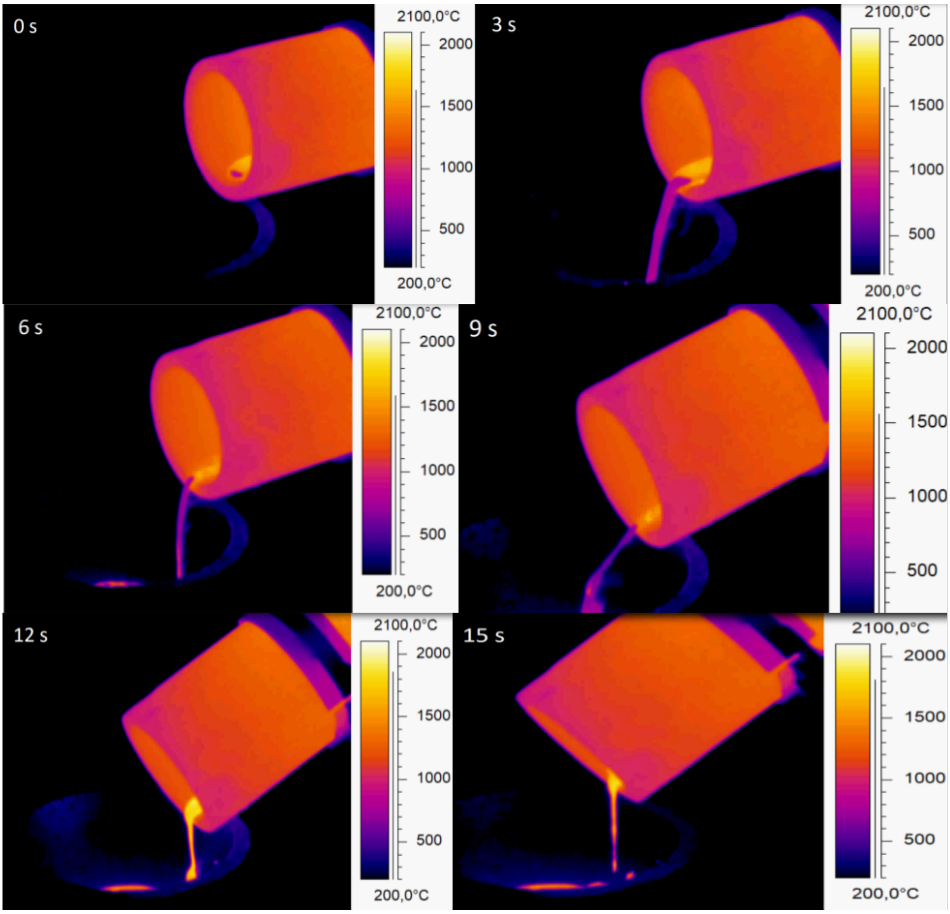

Figure A.5: The simulated tapping session from experiment 1 filmed with the infrared camera.

The maximum temperature was also recorded with the infrared camera and the result can be seen in figure A.6. The temperature shown in this figure is not representable for the real temperature because the emissivity is not known, and was set to be 0.7 in the analysis of the video. However, temperatures seems to fluctuate a lot during the simulated tapping session and the "temperature" of the slag recorded here is much higher than that of FeSi.

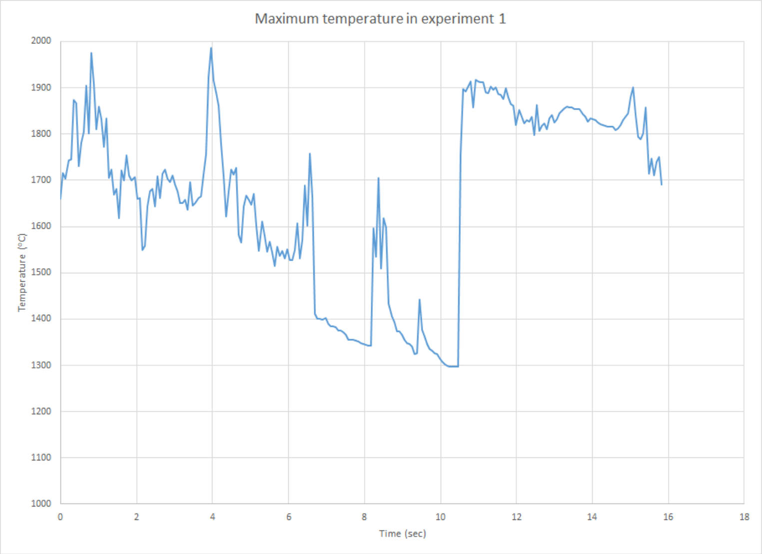

Figure A.6: The maximum temperature measured with the infrared camera for each frame in the experiment 1 video.

Figure A.7 shows the solidified slag and FeSi after experiment 1. The bulk of the slag can be seen close to where the tapping took place. There is also a thin layer of slag visible to the naked eye on top of the bulk mass of FeSi as well.

Figure A.7: The solidified slag and FeSi after experiment 1.

Experiment 2

In experiment 2 slag and FeSi was heated up to 1700°C and the simulated tapping session was filmed with a high speed camera. The temperature log for experiment 2 can be found in figure A.8.

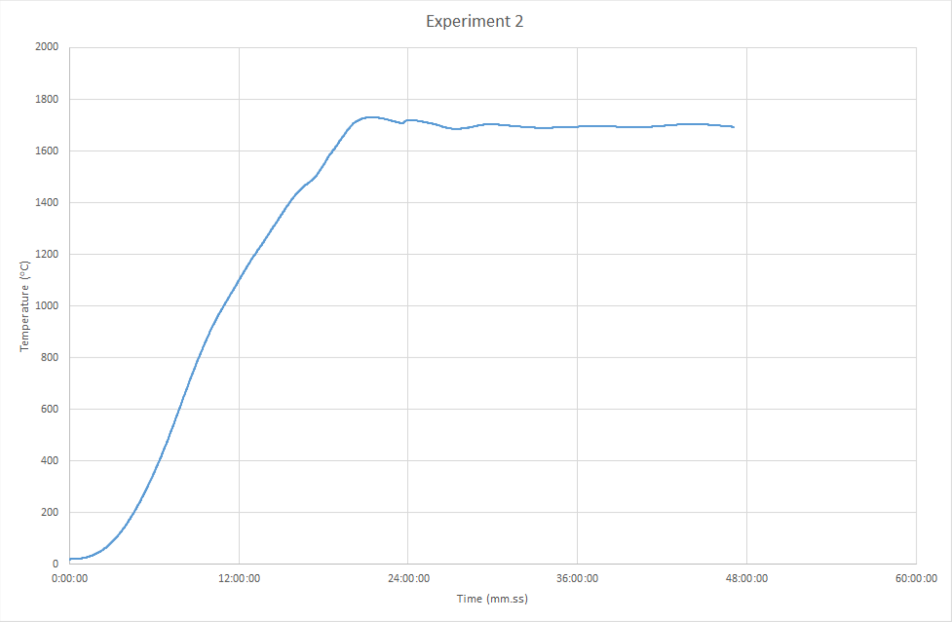

Figure A.8: The temperature log for experiment 2.

A still photo for every 3rd second of the simulated tapping session in experiment 2 can be found in figure A.9. FeSi was first tapped, but not long after a lot of gas and hot dust clouds the view. Near the end of the simulated tapping the cloud disappear and the bulk of the slag can be seen tapped. The slag is very viscous so it takes an additional time after the first 15 seconds to get all out of the crucible.

Figure A.9: The simulated tapping session from experiment 2 filmed with the high speed camera.

Figure A.10 shows the solidified slag and FeSi after experiment 2. The bulk of the slag is spread out on almost the total area of the graphite mold, but is centered around where the tapping happened. A thin layer of slag is also visible to the naked eye over the FeSi mass.

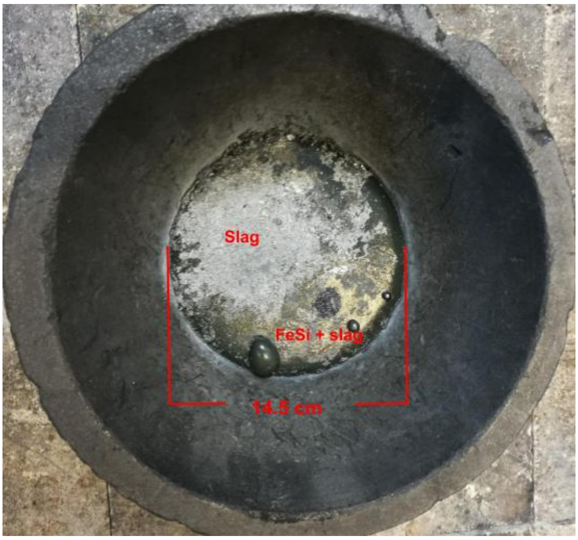

Figure A.10: The solidified slag and FeSi after experiment 2.

Experiment 3

In experiment 3 slag and FeSi was heated up to 1800°C and the simulated tapping session was filmed with a phone camera. The temperature log for experiment 3 can be found in figure A.11.

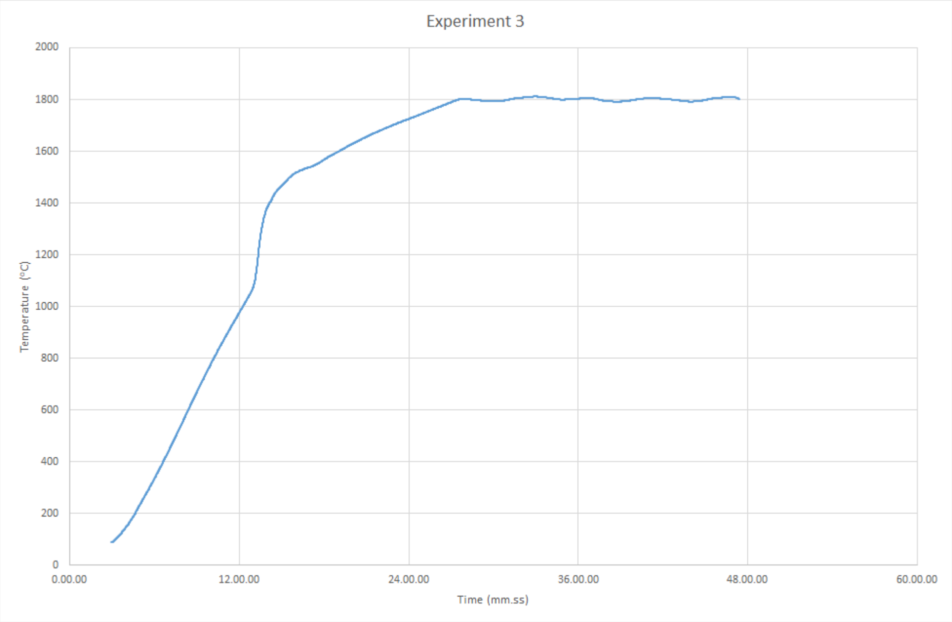

Figure A.11: The temperature log for experiment 3.

A still photo for every 3rd second of the simulated tapping session in experiment 3 can be found in figure A.12. FeSi is tapped first for half of the tapping duration. Some smoke and dust clouds also obscures the view hal-way in. In the last part of the simulated tapping the slag is seen. This is very viscous, and it takes some additional seconds to clear it out of the crucible.

Figure A.13 shows the solidified slag and FeSi after experiment 3. The bulk of the slag is spread out over half the area in the graphite mold, but is centered around the area where the tapping happened. A thin layer of slg is also visible to the naked eye of the bulk of FeSi.

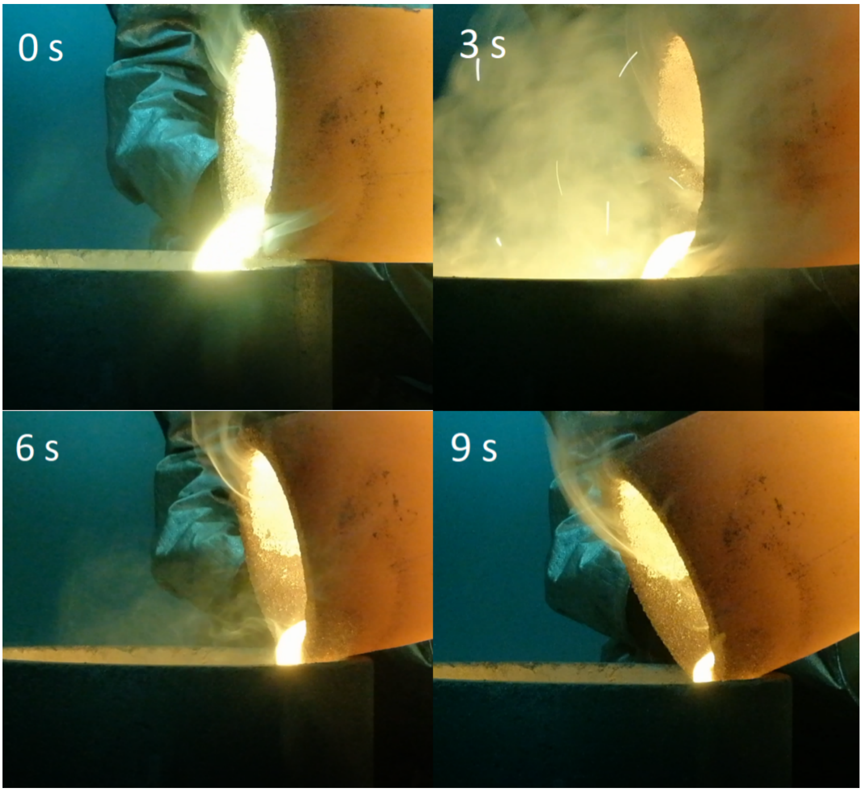

Figure A.12: The simulated tapping session from experiment 3 filmed with the phone camera.

Figure A.13: The solidified slag and FeSi after experiment 3.

Appendix B

Calculations

Heat Capacity and Density of liquid FeSi, $C_{p,FeSi}$ and ρ_{FeSi}

The calculation of heat capacity of FeSi, $C_{p,FeSi}$, was based on the heat capacity of iron and silicon at 1900°C. In HSC (2018-05-08) the heat capacities at 1900°C is given as

- $C_{p,Fe}$ = 824 J/(kgK)
- $C_{p,Si}$ = 968 J/(kgK)

With a FeSi composition at 75 % Si and 25% Fe the heat capacity of FeSi, $C_{p,FeSi}$, would be

$$C_{p,FeSi} = x_{Fe} \cdot C_{p,Fe} + x_{Si} \cdot C_{p,Si} = (0.25 \cdot 824 + 0.75 \cdot 968) J/(kgK) = 932 J/(kgK) \tag{B.1}$$

The calculation of density of liquid FeSi, ρ_{FeSi}, was based on the density of liquid iron and silicon at 1600°C. The density of liquid iron was given by Jimbo and Cramb (1993) to be 7.12 g/cm^3 at 1600°C and the density of liquid silicon was found by Rhim and Ohsaka (2000) to be 2.60 g/cm^3 at 1600°C. If it is assumed that no volume expansion occurs when iron and silicon mix the density of liquid FeSi with 75 % Si and 25 % Fe at 1600°C is

$$\rho_{FeSi} = x_{Fe} \cdot \rho_{Fe} + x_{Si} \cdot \rho_{Si} = (0.25 \cdot 7.12 + 0.75 \cdot 2.60) g/cm^3 = 3.73 g/cm^3 \tag{B.2}$$

Al_2O_3, CaO, and SiO_2 from elemental analysis

In the EDS elemental analysis the slag composition found on slag sample 1-4 the following equations were used for calculating the mass of Al_2O_3, CaO, and SiO_2 of 100 g slag with the elemental composition given by the analysis:

$$m_{CaO} = m_{Ca} + \frac{m_{Ca}}{M_{Ca}} \cdot M_O, \tag{B.3}$$

$$m_{Al_2O_3} = m_{Al} + \frac{3}{2} \cdot \frac{m_{Al_2O_3}}{M_{Al_2O_3}} \cdot M_O, \tag{B.4}$$

$$m_{SiO_2} = m_{Si} + 2 \cdot \frac{m_{SiO_2}}{M_{SiO_2}} \cdot M_O, \tag{B.5}$$

where the molar weight is given by HSC Chemical 9 as M_{Ca} = 40 g/mol, M_{Al} = 27 g/mol, M_{Si} = 28 g/mol, and M_O = 16 g/mol. The elemental analysis for slag sample 1-4 gives

- Sample 1: m_{Ca} = 7.7 g, m_{Al} = 10.3 g, m_{Si} = 30.9 g.
- Sample 2: m_{Ca} = 11.9 g, m_{Al} = 11.9 g, m_{Si} = 20.4 g.
- Sample 3: m_{Ca} = 27.7 g, m_{Al} = 16.3 g, m_{Si} = 14.6 g.
- Sample 4: m_{Ca} = 25.4 g, m_{Al} = 19.9 g, m_{Si} = 12.7 g.

The mass percentage of Al_2O_3, CaO, and SiO_2 was calculated with the following equations:

$$\%CaO = \frac{m_{CaO}}{m_{CaO} + m_{Al_2O_3} + m_{SiO_2}}, \tag{B.6}$$

$$\%Al_2O_3 = \frac{m_{Al_2O_3}}{m_{CaO} + m_{Al_2O_3} + m_{SiO_2}}, \tag{B.7}$$

$$\%SiO_2 = \frac{m_{SiO_2}}{m_{CaO} + m_{Al_2O_3} + m_{SiO_2}}. \tag{B.8}$$

With the above numbers the mass percentage of Al_2O_3, CaO, and SiO_2 in the slag phases found on sample 1-4 are:

- Sample 1: %CaO = 11.2, %Al_2O_3 = 20.2, %SiO_2 = 68.6
- Sample 2: %CaO = 20.1, %Al_2O_3 = 27.3, %SiO_2 = 52.7
- Sample 3: %CaO = 38.5, %Al_2O_3 = 30.5, %SiO_2 = 31.0
- Sample 4: %CaO = 33.6, %Al_2O_3 = 38.6, %SiO_2 = 27.8

Heat Transfer Coefficient, h$_c$

The heat transfer coefficient was estimated by the use of the following equation:

$$h_c = 0.53\frac{k_{Si}}{D}\left[\left(\frac{c_{p,FeSi}\nu_{FeSi}\rho_{FeSi}}{k_{Si}}\right)\left(\frac{D^3\beta_{Si}(T^0_{FeSi} - T^0_{ladle})g}{\nu^2_{FeSi}}\right)\right]^{0.25}. \tag{B.9}$$

where

- Thermal conductivity of silicon k_{Si} = 60 W/(mK) (Kobatake et al. (2007))
- Heihjt of ladle D = 1.5 m
- Heat capacity of FeSi $C_{p,FeSi}$ = 932 J/(kgK) (HSC Chemical 9)
- Kinematic viscocity of FeSi ν_{FeSi} = 0.0000006 m^2/s (Bel'tyukov et al. (2014))
- Density of FeSi ρ_{FeSi} = 3730 kg/m^3 (Rhim and Ohsaka (2000), Jimbo and Cramb (1993))
- Thermal expansion coefficient for silicon β_{Si} = 0.00014 1/K (Langen et al. (1998)
- The temperature of FeSi out of the furnace T$^0_{FeSi}$ = 1900°C
- The temperature of the ladle T$^0_{ladle}$ = 700°C
- The temperature of the runner T$^0_{runner}$ = 700°

This resulted in h$_c$ = 38 373 W/(m^{2}K). The heat transfer coefficient was also calculated with the following equations for ladle and runner:

$$h_c = 0.27(T^0_{FeSi} - T^0_{ladle})^{0.25} \tag{B.10}$$

for the ladle, and

$$h_c = 0.2(T^0_{FeSi} - T^0_{runner})^{0.25} \tag{B.11}$$

for the runner. This resulted in h$_c$ = 7.8 W/(m^{2}K) in the runner, and h$_c$ = 10.6 W/(m^{2}K) in the ladle. The last method used for estimating h$_c$ is by assuming that the runner has increased 200°C after 30 minutes of tapping as stated earlier, and calculate the amount of heat energy that is required to heat the runner up to that amount:

$$Q_{runner} = mC_{p,C}\Delta T, \tag{B.12}$$

where ΔT equals 200°C. The heat transfer coefficient can then be calculated by using equation 2.17:

$$h_c = \frac{Q_{runner}}{A(T^0_{FeSi} - T^0_{runner})t}, \tag{B.13}$$

where t equals 1800 seconds (30 minutes). This resulte din a heat transfer coefficient h$_c$ = 131 W/(m^{2}K).

Appendix C

EDS analysis results

This chapter includes all EDS element analysis done on slag samples 1-4.

EDS analysis of slag sample 1

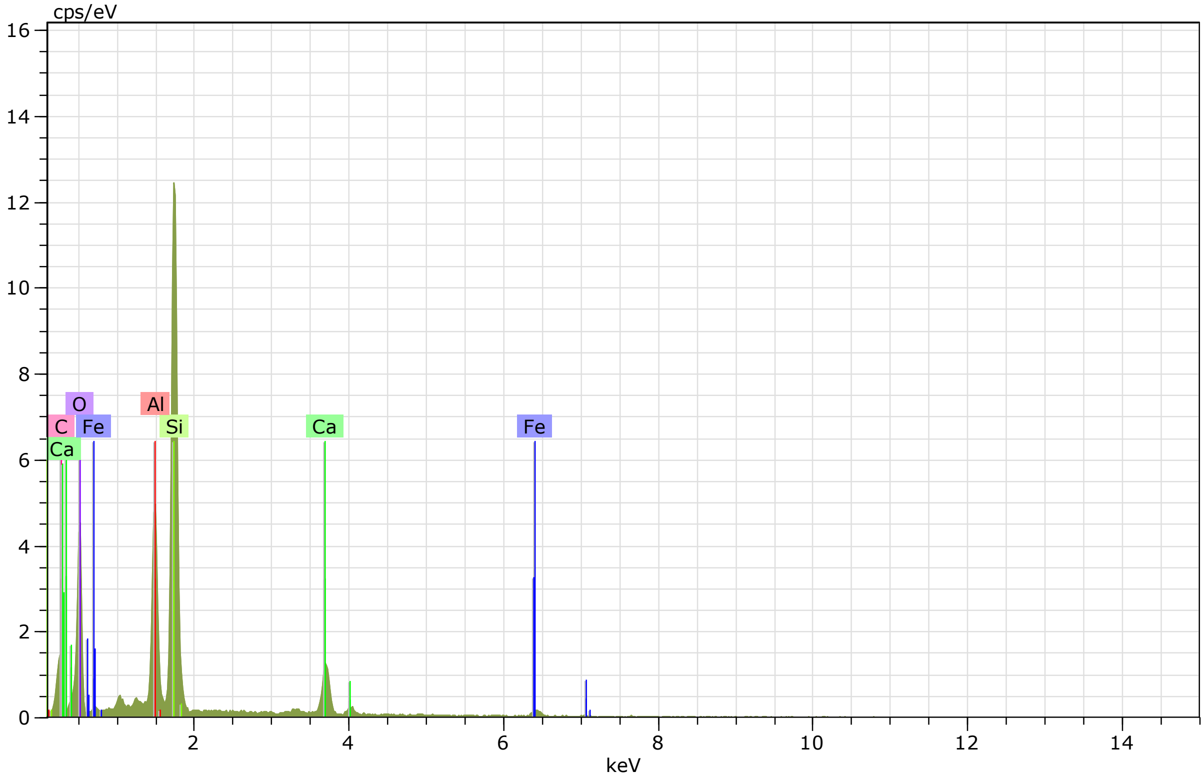

```
Spectrum:  59

El AN  Series     Net unn. C norm. C Atom. C Error (1 Sigma)
                      [wt.%]   [wt.%]   [at.%]          [wt.%]
-----------------------------------------------------------
O  8  K-series  8183  32.11   34.96   39.97            4.66
C  6  K-series  2314  20.50   22.32   34.00            3.78
Si 14 K-series 31150  23.27   25.34   16.50            1.01
Al 13 K-series 10981   7.97    8.68    5.89            0.41
Ca 20 K-series  4084   5.64    6.14    2.80            0.22
Fe 26 K-series   569   2.35    2.56    0.84            0.16
-----------------------------------------------------------
               Total:  91.85  100.00  100.00
```

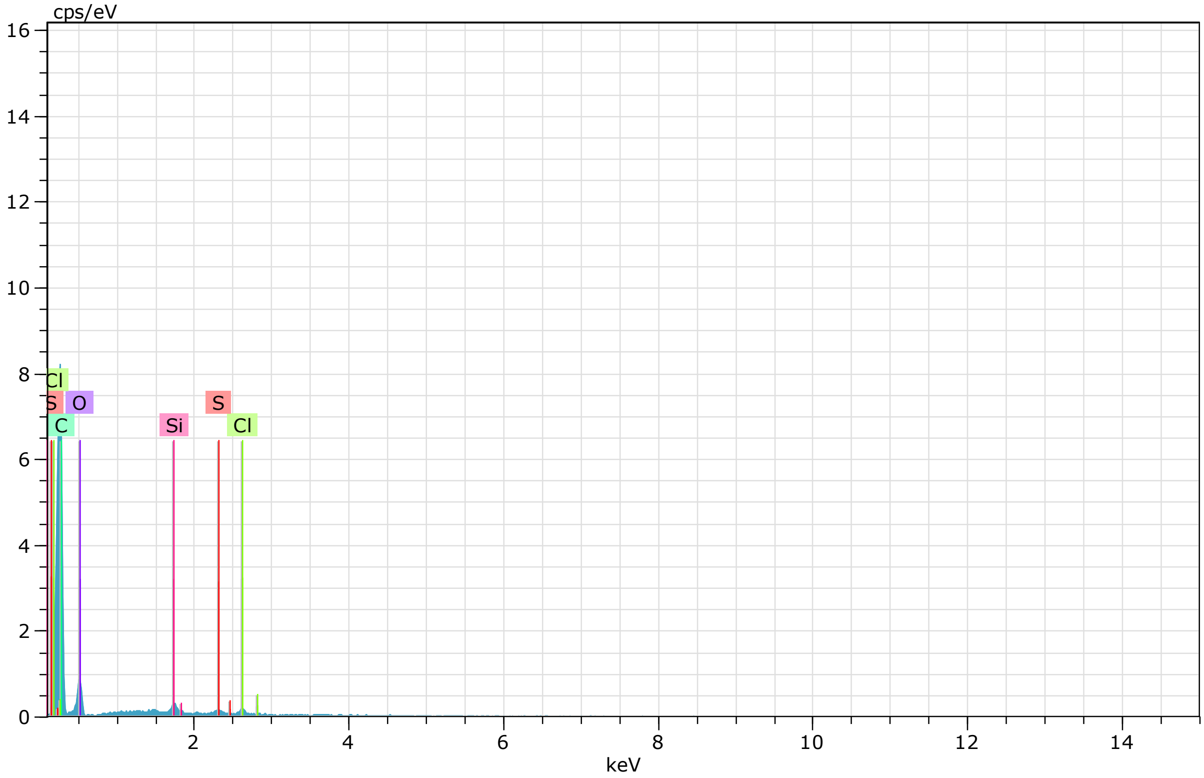

```
Spectrum:  60

El AN  Series    Net unn. C norm. C Atom. C Error (1 Sigma)
                     [wt.%]  [wt.%]  [at.%]           [wt.%]
-----------------------------------------------------------
C   6  K-series 13617  76.37   76.37   81.81            10.28
O   8  K-series  1602  21.58   21.58   17.36             4.34
Si 14  K-series   521   0.75    0.75    0.35             0.08
Cl 17  K-series   392   0.79    0.79    0.29             0.08
S  16  K-series   300   0.51    0.51    0.21             0.06
-----------------------------------------------------------
               Total: 100.00  100.00  100.00
```

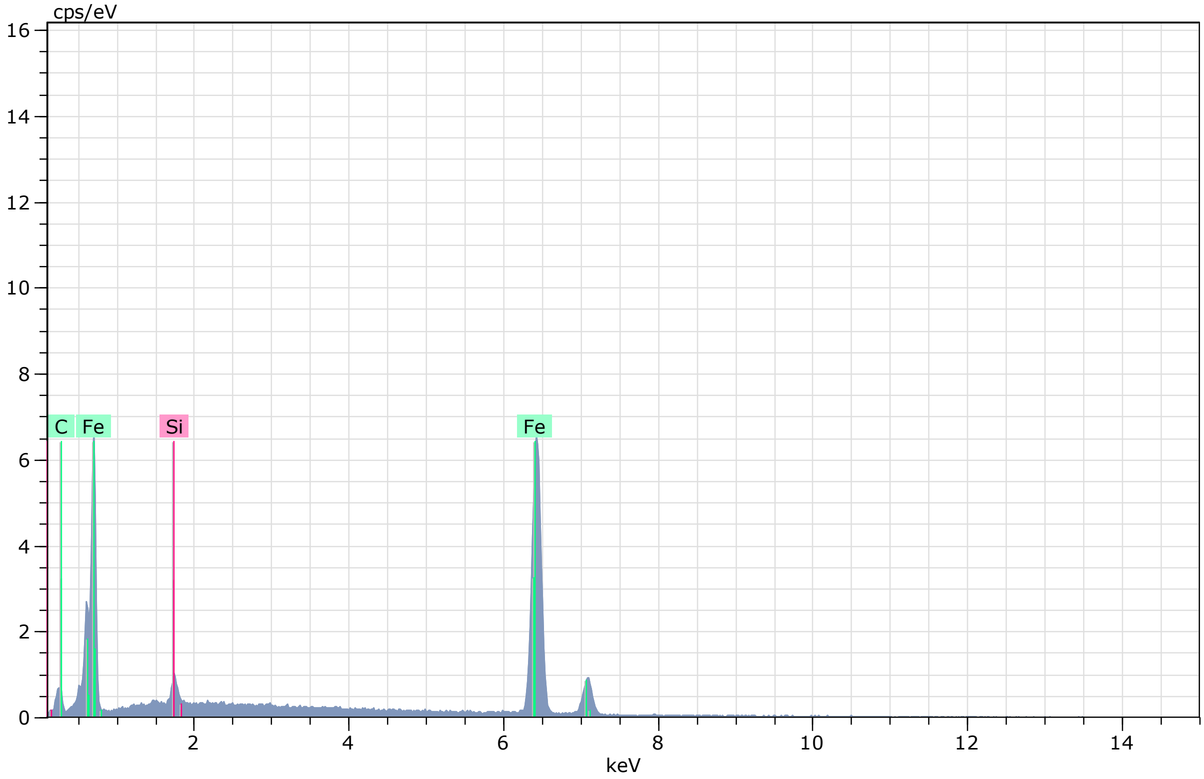

```
Spectrum:  61

El AN   Series     Net unn. C norm. C Atom. C Error (1 Sigma)
                        [wt.%]  [wt.%]  [at.%]           [wt.%]
-----------------------------------------------------------------
Fe 26 K-series 27766  80.95   91.62   72.26            2.46
C   6  K-series  1037   6.15    6.96   25.52            1.40
Si 14 K-series  1570   1.25    1.42    2.22            0.09
-----------------------------------------------------------------
               Total:  88.35  100.00  100.00
```

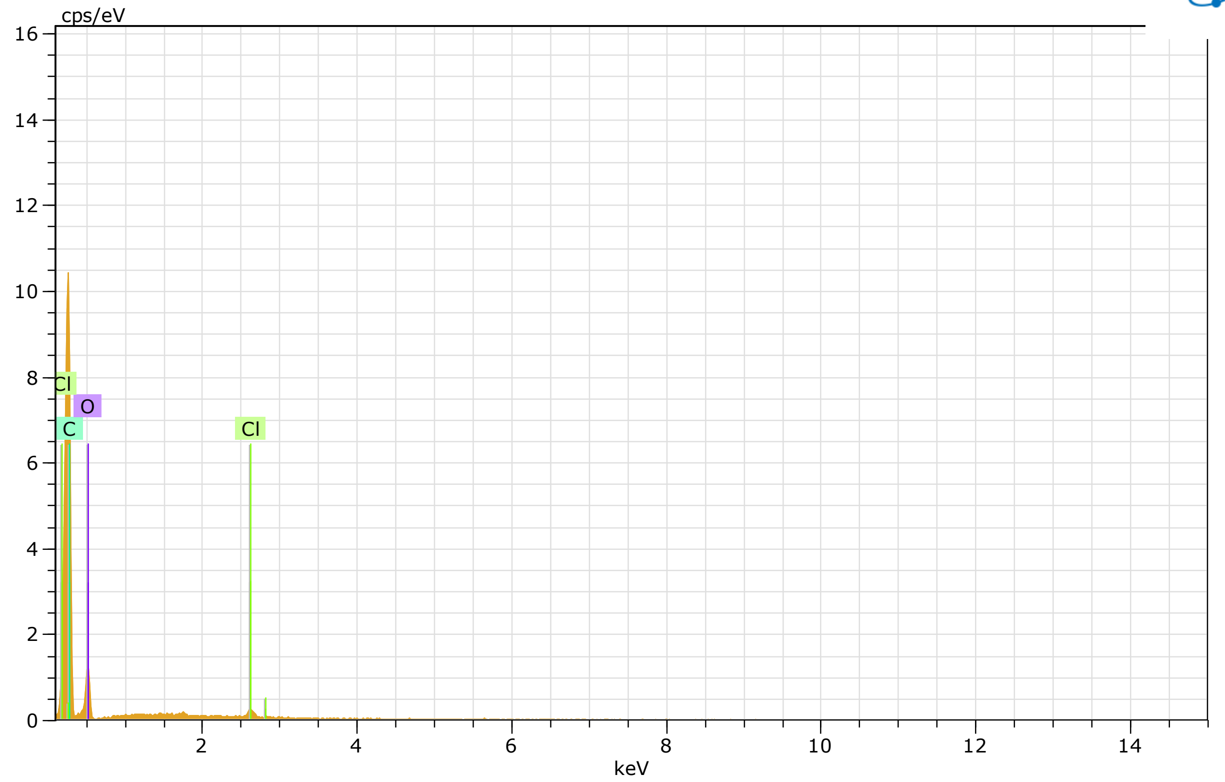

```
Spectrum:   62

El AN   Series     Net unn. C norm. C Atom. C Error (1 Sigma)
                       [wt.%]   [wt.%]   [at.%]           [wt.%]
-----------------------------------------------------------
C   6   K-series 17438   75.14    75.24    80.49             9.81
O   8   K-series  2212   23.88    23.91    19.20             4.44
Cl 17   K-series   545    0.84     0.84     0.31             0.08
-----------------------------------------------------------
               Total:   99.86   100.00   100.00
```

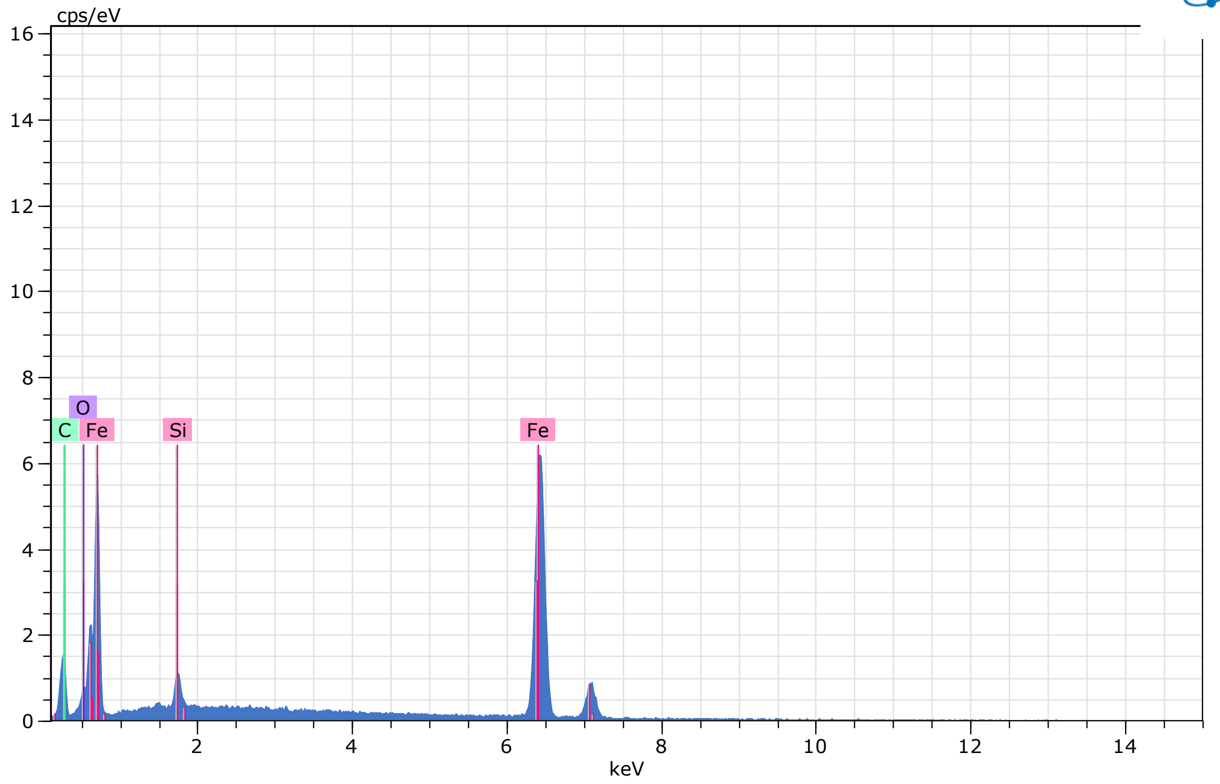

```
Spectrum:  63

El AN  Series     Net unn. C norm. C Atom. C Error (1 Sigma)
                      [wt.%]  [wt.%]  [at.%]           [wt.%]
-------------------------------------------------------------
Fe 26 K-series 26867  74.06   81.65   51.19              2.25
C   6 K-series  2484  12.93   14.25   41.54              2.36
O   8 K-series   941   2.09    2.30    5.04              0.51
Si 14 K-series  2042   1.62    1.79    2.23              0.11
-------------------------------------------------------------
               Total:  90.70  100.00  100.00
```

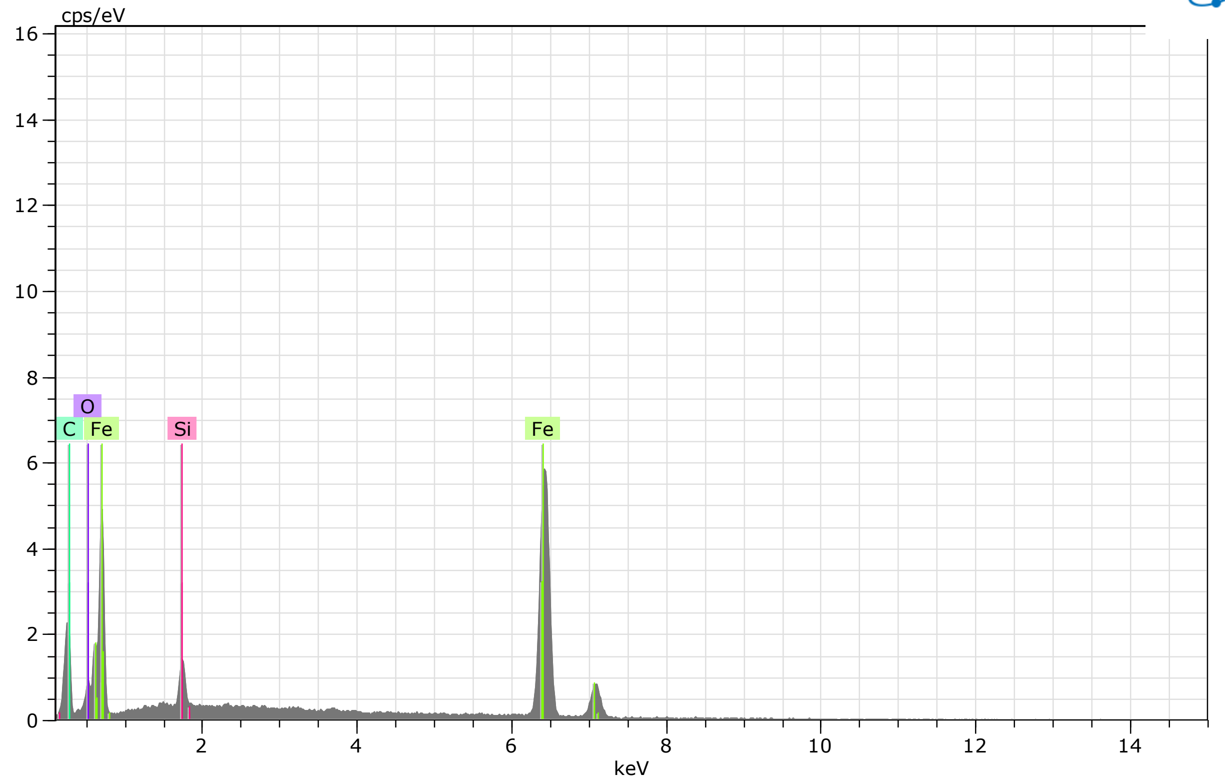

```
Spectrum:  64

El AN  Series    Net unn. C norm. C Atom. C Error (1 Sigma)
                     [wt.%]   [wt.%]   [at.%]           [wt.%]
------------------------------------------------------------
C   6  K-series  3828  17.94    20.05    50.94            2.98
Fe 26  K-series 25508  66.96    74.84    40.90            2.04
O   8  K-series  1244   2.84     3.17     6.05            0.63
Si 14  K-series  2564   1.74     1.95     2.11            0.11
------------------------------------------------------------
               Total:   89.47   100.00   100.00
```

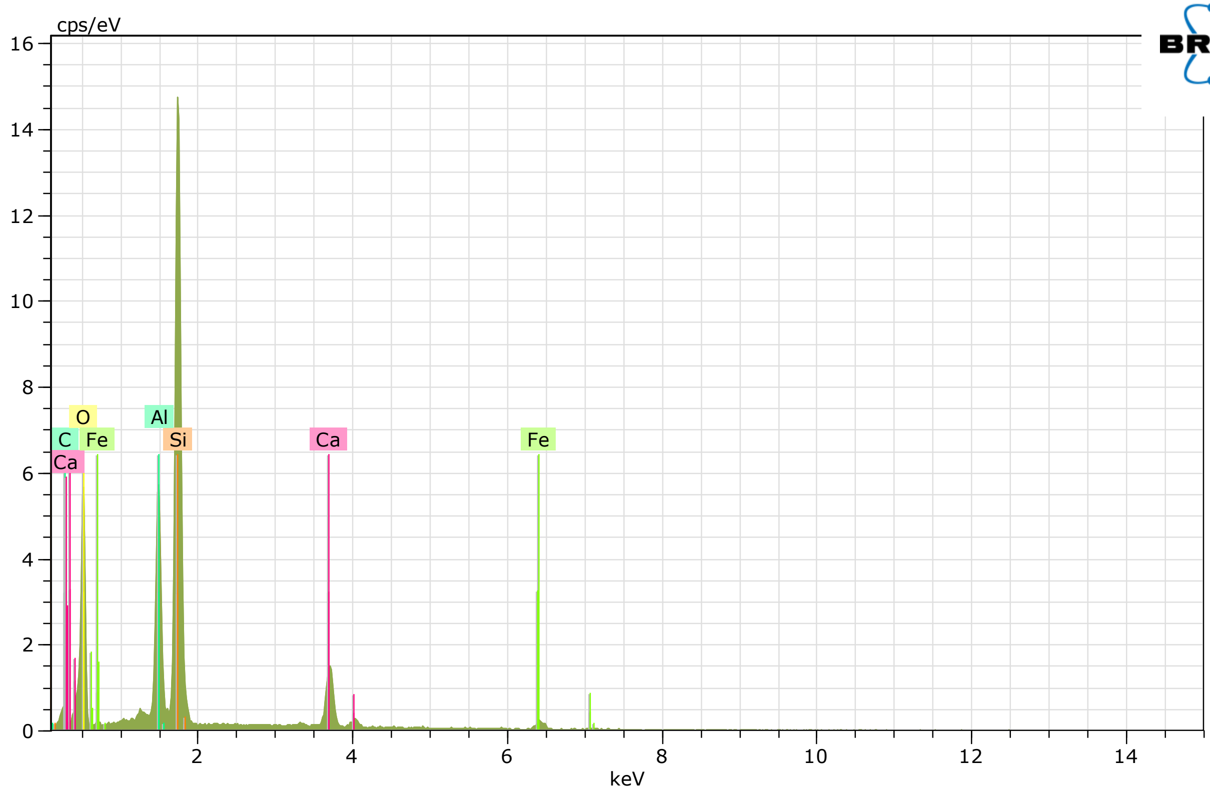

```
Spectrum:  58

El AN  Series    Net unn. C norm. C Atom. C Error (1 Sigma)
                     [wt.%]  [wt.%]  [at.%]           [wt.%]
-----------------------------------------------------------
O  8  K-series 10116  33.51   39.07   50.01             4.71
Si 14 K-series 36238  26.48   30.88   22.52             1.14
C  6  K-series   730   7.25    8.46   14.42             1.82
Al 13 K-series 12494   8.80   10.26    7.79             0.45
Ca 20 K-series  4991   6.59    7.68    3.93             0.25
Fe 26 K-series   803   3.13    3.64    1.34             0.18
-----------------------------------------------------------
               Total:  85.76  100.00  100.00
```

EDS analysis of slag sample 2

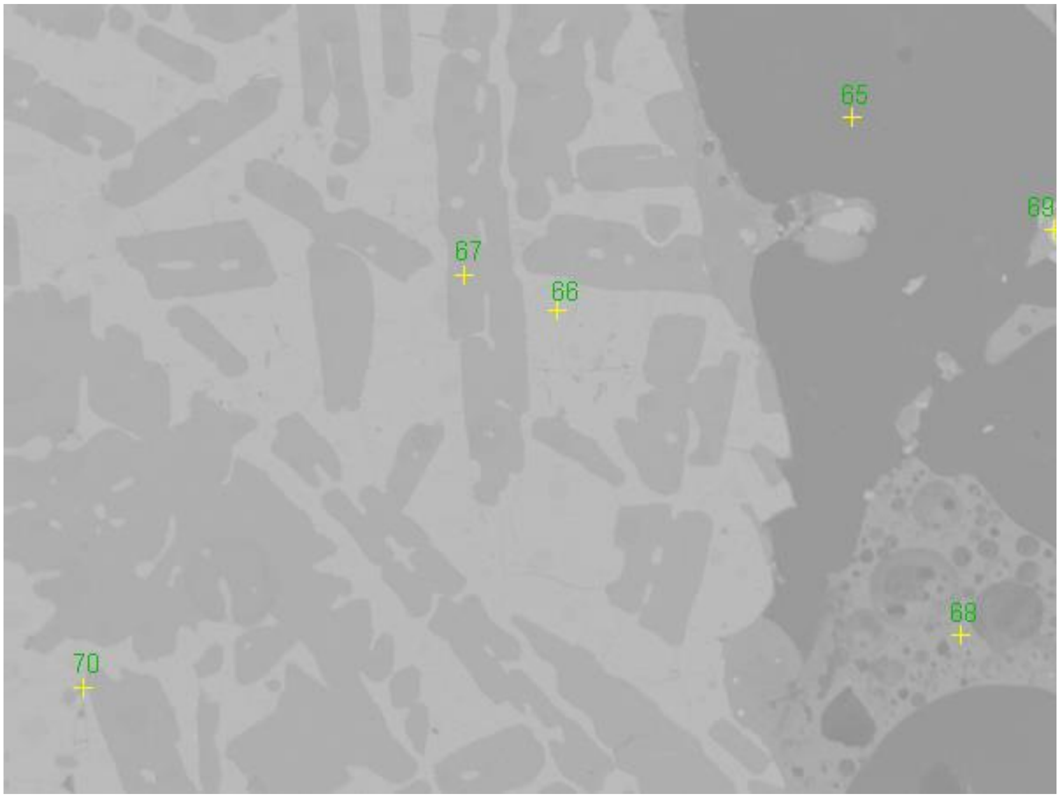

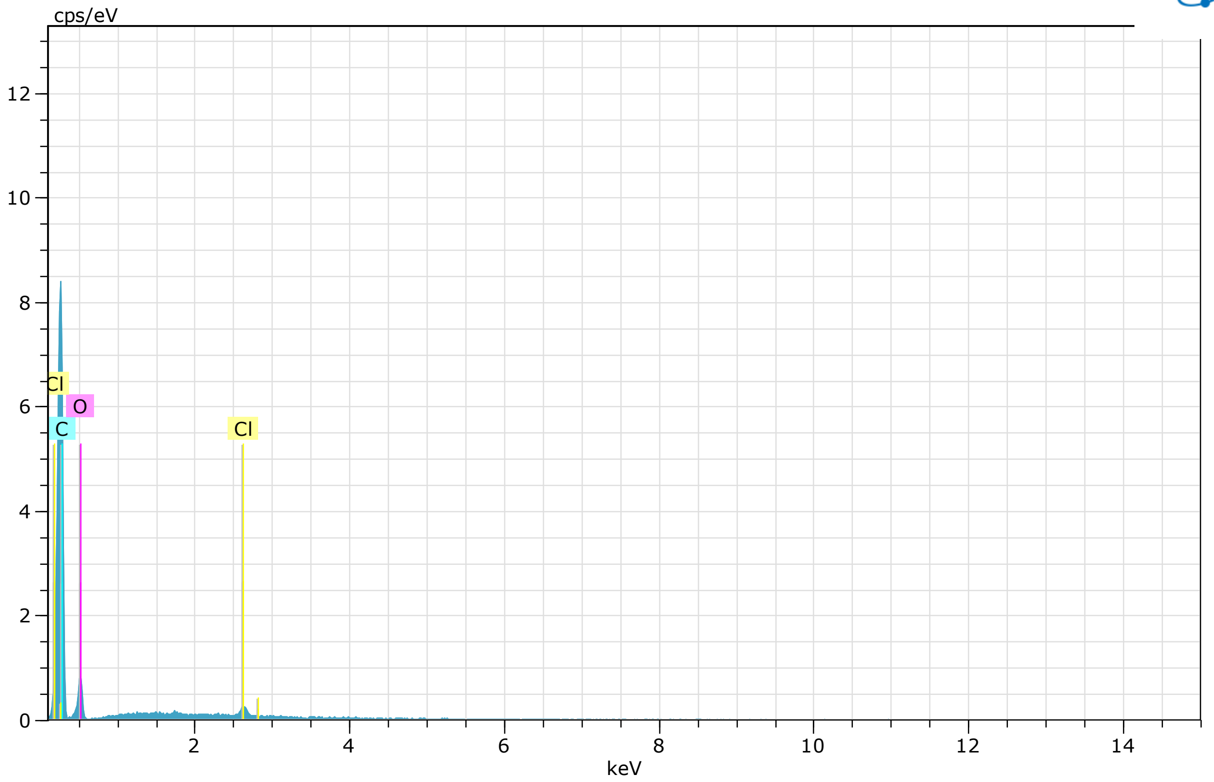

```
Spectrum:  65

El AN  Series    Net unn. C norm. C Atom. C Error (1 Sigma)
                     [wt.%]  [wt.%]  [at.%]          [wt.%]
-------------------------------------------------------------
C   6  K-series 14116  77.50   77.50   82.45          10.38
O   8  K-series  1498  21.54   21.54   17.21           4.41
Cl 17  K-series   490   0.96    0.96    0.35           0.08
-------------------------------------------------------------
                Total: 100.00  100.00  100.00
```

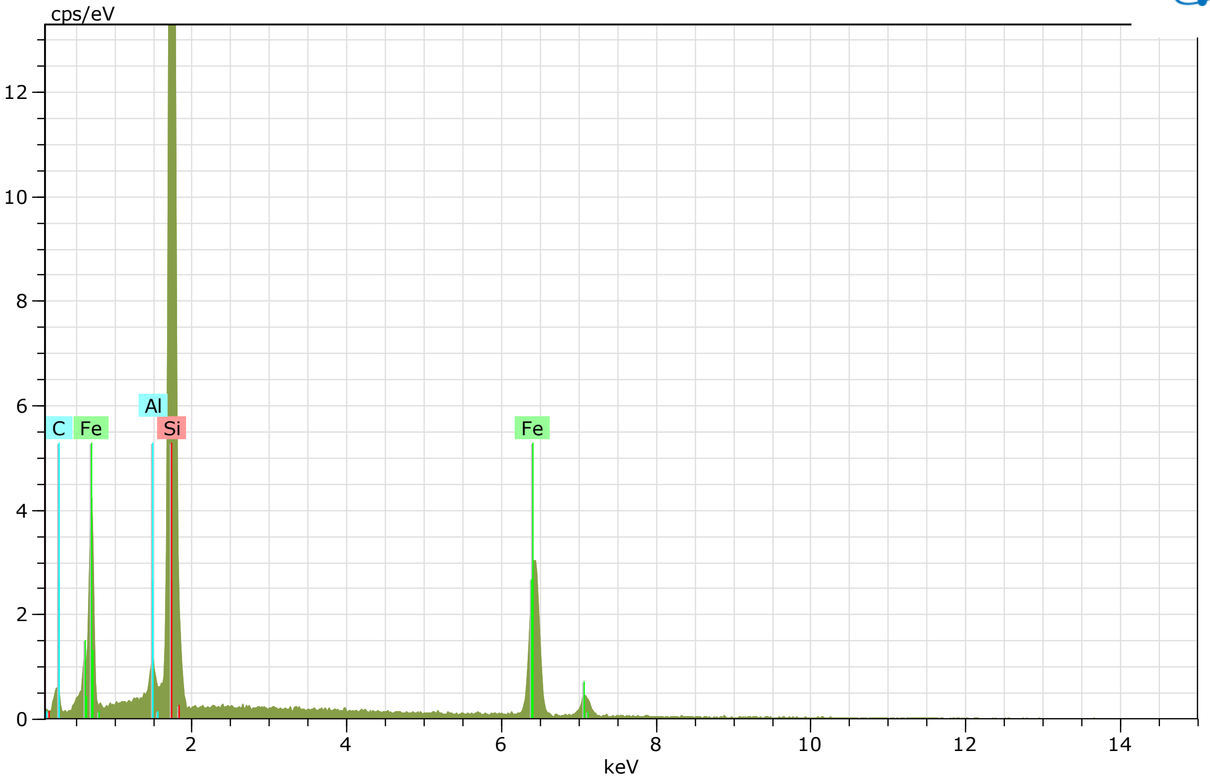

```
Spectrum:  66

El AN  Series    Net unn. C norm. C Atom. C Error (1 Sigma)
                     [wt.%]   [wt.%]   [at.%]           [wt.%]
-----------------------------------------------------------------
Si 14 K-series 72016  44.53   46.56   49.47            1.89
C   6  K-series   996  10.43   10.90   27.09            2.39
Fe 26 K-series 13041  39.50   41.30   22.07            1.25
Al 13 K-series  1749   1.19    1.24    1.37            0.09
-----------------------------------------------------------------
               Total:  95.65  100.00  100.00
```

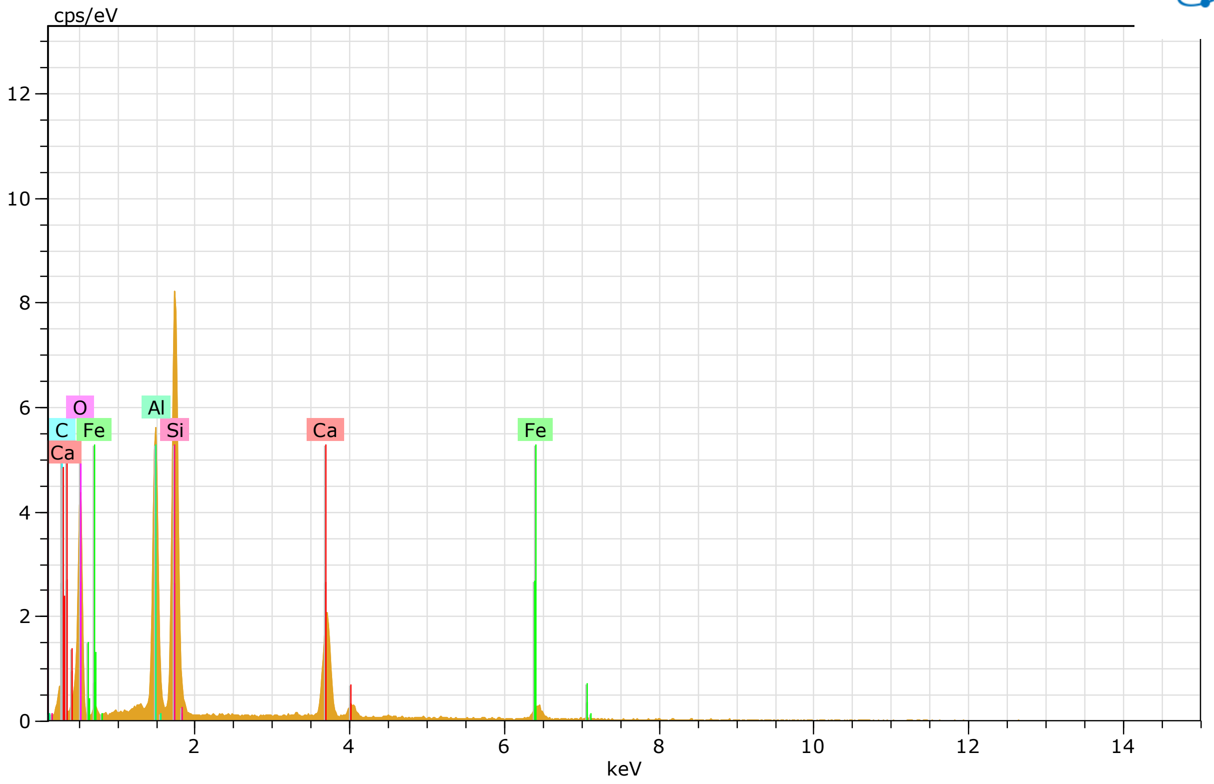

```
Spectrum:  68

El AN  Series    Net unn. C norm. C Atom. C Error (1 Sigma)
                     [wt.%]  [wt.%]  [at.%]          [wt.%]
-----------------------------------------------------------
O  8  K-series  7724  33.27   38.76   49.16            4.87
C  6  K-series   974   9.65   11.25   19.00            2.23
Si 14 K-series 20006  17.53   20.42   14.76            0.77
Al 13 K-series 12074  10.21   11.90    8.95            0.52
Ca 20 K-series  6797  10.22   11.91    6.03            0.36
Fe 26 K-series  1085   4.94    5.76    2.09            0.25
-----------------------------------------------------------
               Total:  85.82  100.00  100.00
```

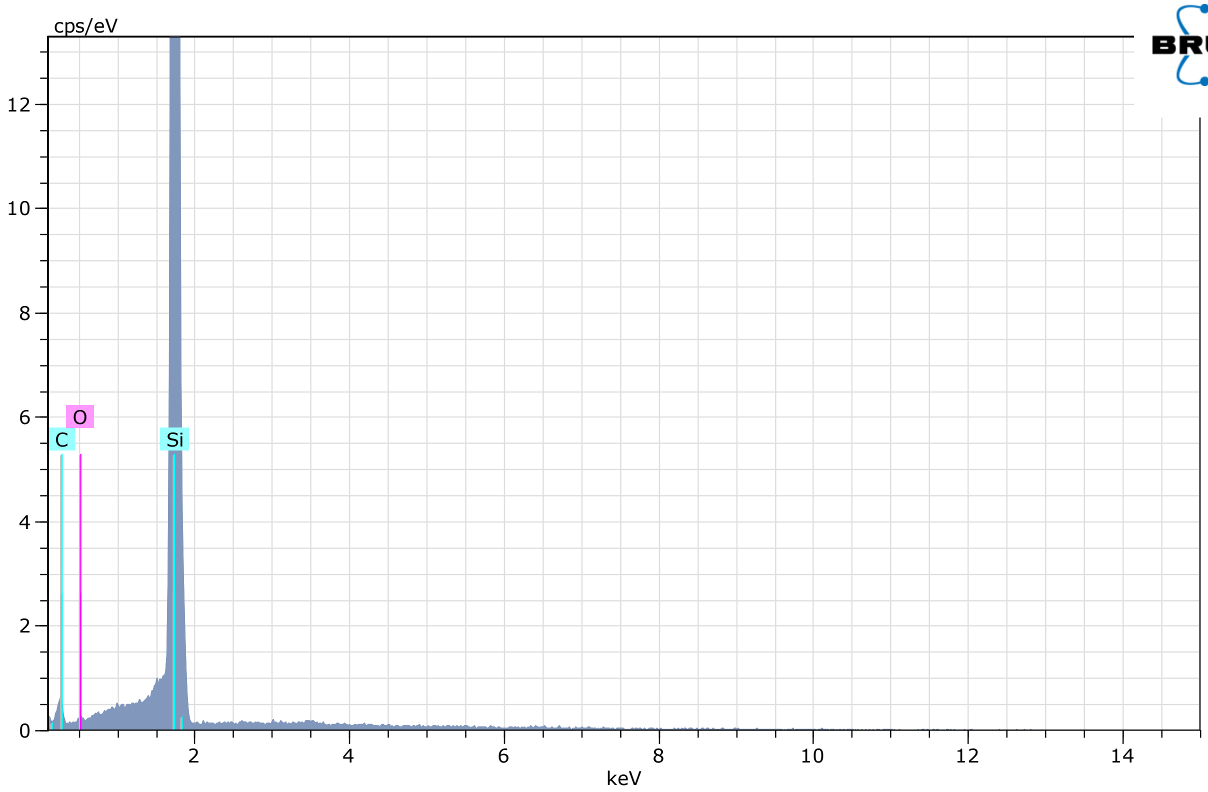

```
Spectrum:   67

El AN   Series      Net unn. C norm. C Atom. C Error (1 Sigma)
                         [wt.%]   [wt.%]   [at.%]           [wt.%]
-----------------------------------------------------------------
Si 14 K-series 163556  76.68    84.11    69.70             3.22
C   6  K-series    1051  13.55    14.86    28.80             3.05
O   8  K-series     277   0.94     1.03     1.50             0.34
-----------------------------------------------------------------
                  Total:  91.17   100.00   100.00
```

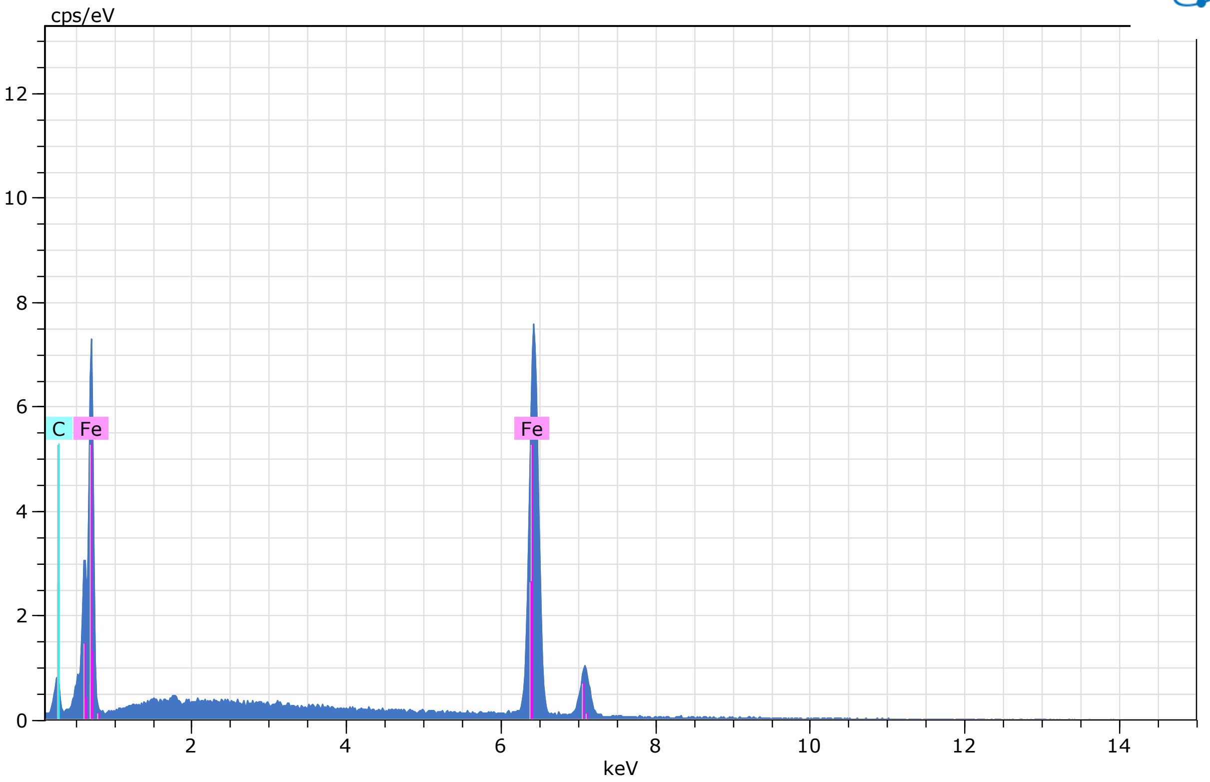

```
Spectrum:  69

El AN  Series    Net unn. C norm. C Atom. C Error (1 Sigma)
                     [wt.%]  [wt.%]  [at.%]           [wt.%]
-------------------------------------------------------------
Fe 26 K-series 31835  83.96   92.85   73.65             2.54
C   6  K-series  1232   6.46    7.15   26.35             1.41
-------------------------------------------------------------
               Total:  90.42  100.00  100.00
```

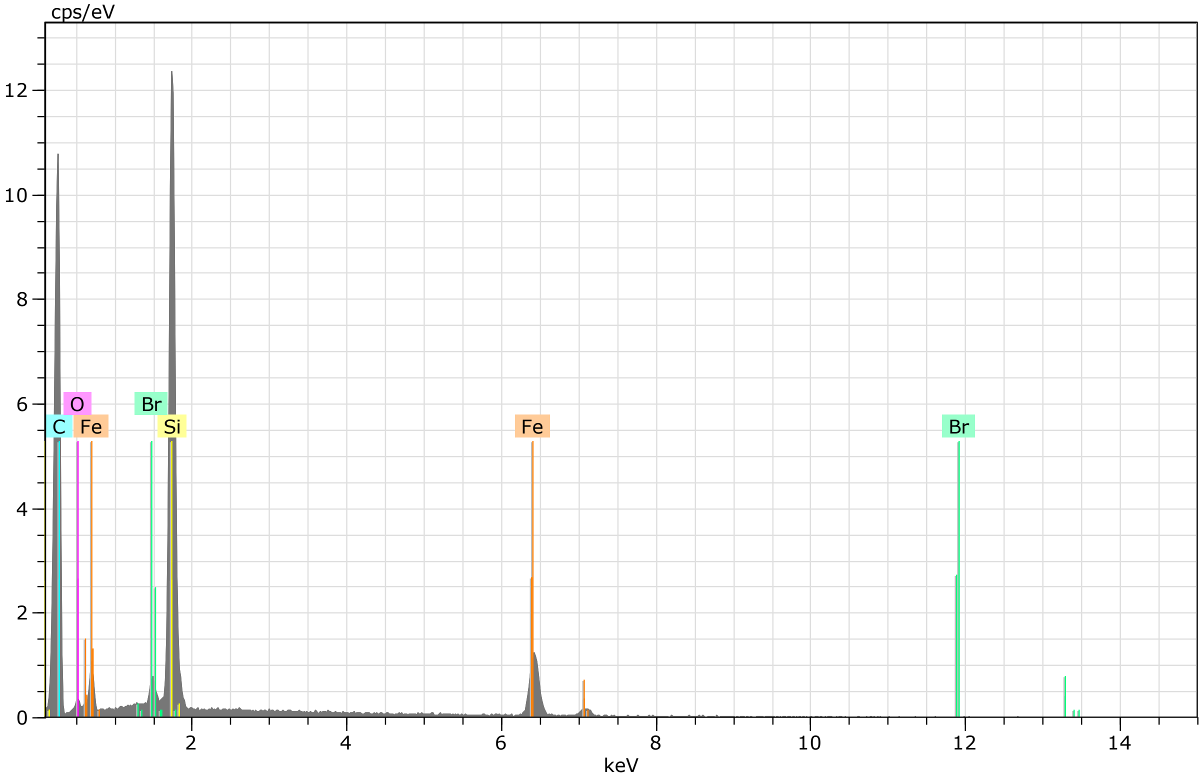

```
Spectrum:  70

El AN  Series    Net unn. C norm. C Atom. C Error (1 Sigma)
                     [wt.%]  [wt.%]  [at.%]          [wt.%]
-----------------------------------------------------------
C   6  K-series 18338  90.13   68.12   85.56          11.70
Si 14  K-series 30739  21.28   16.08    8.64           0.92
Fe 26  K-series  5123  15.82   11.96    3.23           0.56
O   8  K-series   600   3.23    2.44    2.30           0.88
Br 35  L-series  1633   1.86    1.41    0.27           0.13
-----------------------------------------------------------
               Total: 132.33  100.00  100.00
```

Slag sample 3

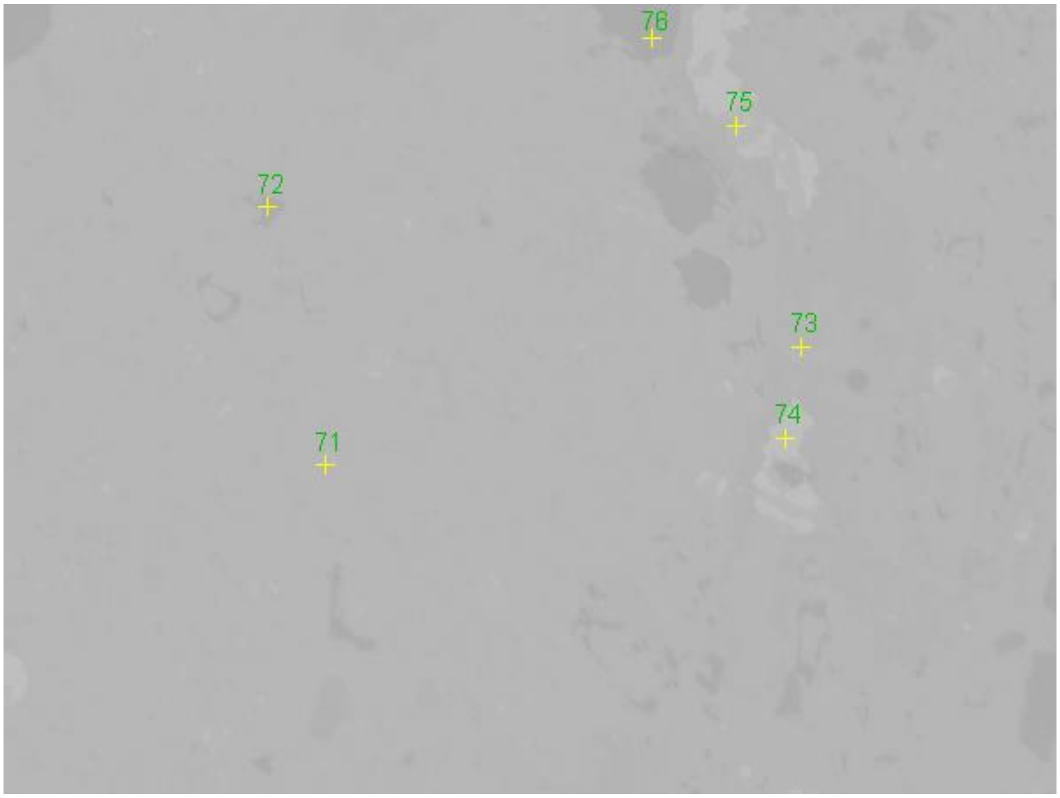

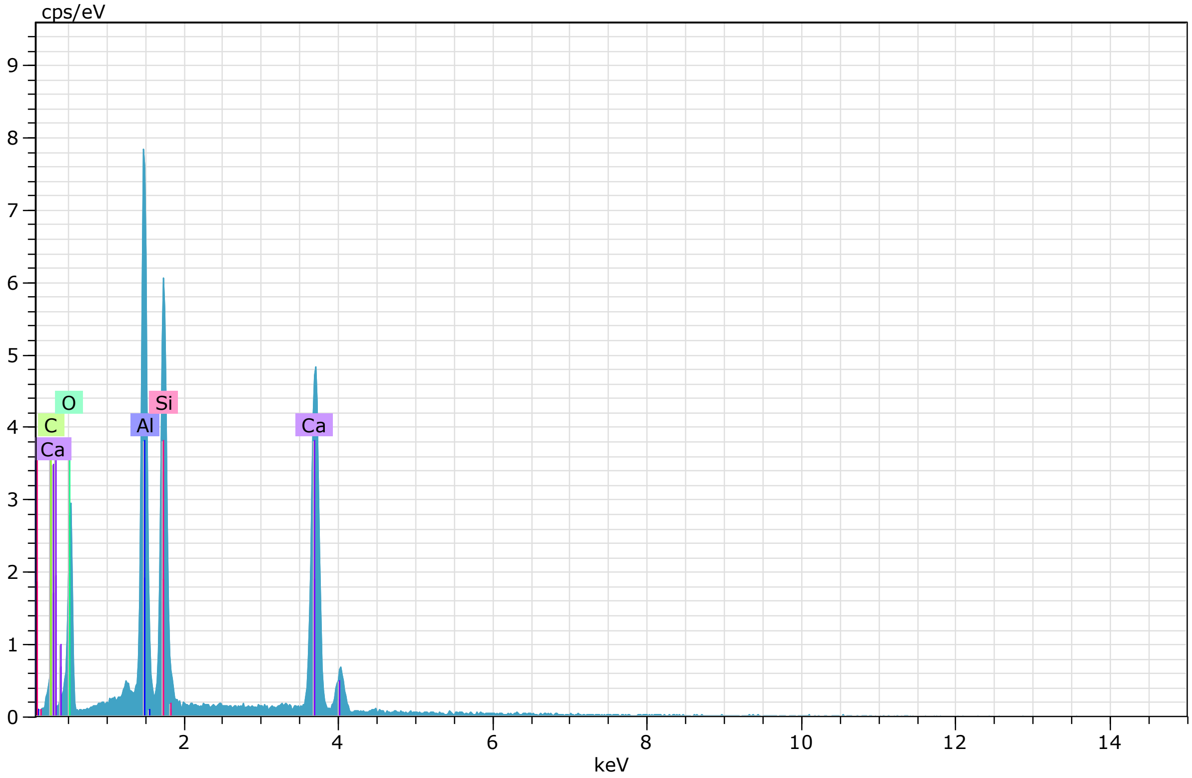

```
Spectrum:  71

El AN   Series    Net unn. C norm. C Atom. C Error (1 Sigma)
                      [wt.%]   [wt.%]   [at.%]           [wt.%]
-------------------------------------------------------------
O   8  K-series   5258  28.47   33.87   46.48             4.44
Ca  20 K-series 16867  23.31   27.74   15.19             0.75
C   6  K-series    733   6.26    7.44   13.61             1.58
Al  13 K-series 17705  13.72   16.33   13.29             0.68
Si  14 K-series 14726  12.29   14.62   11.43             0.55
-------------------------------------------------------------
               Total:   84.05  100.00  100.00
```

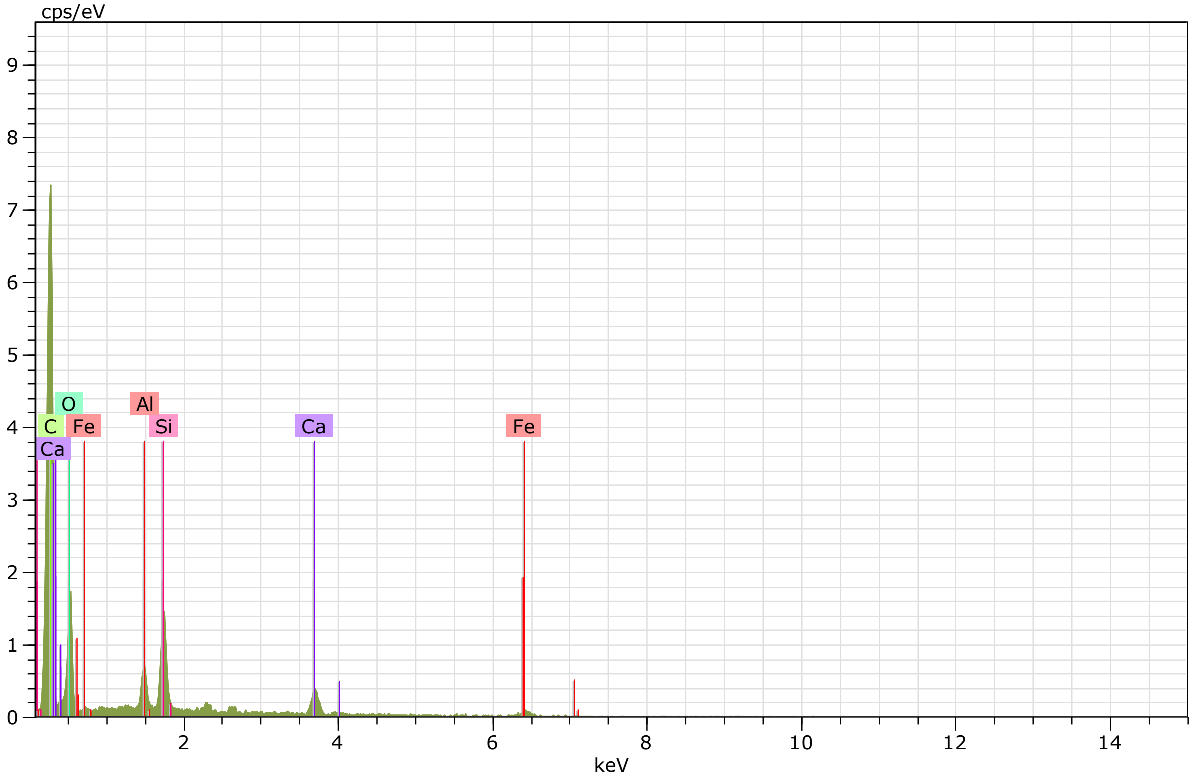

```
Spectrum:  72

El AN   Series    Net unn. C norm. C Atom. C Error (1 Sigma)
                      [wt.%]   [wt.%]  [at.%]           [wt.%]
-----------------------------------------------------------
C   6  K-series 12787  63.58    63.58   72.90             8.63
O   8  K-series  3163  27.09    27.09   23.32             4.66
Si 14  K-series  3311   3.54     3.54    1.73             0.19
Ca 20  K-series  1181   2.39     2.39    0.82             0.13
Al 13  K-series  1312   1.47     1.47    0.75             0.11
Fe 26  K-series   306   1.92     1.92    0.47             0.16
-----------------------------------------------------------
               Total: 100.00   100.00  100.00
```

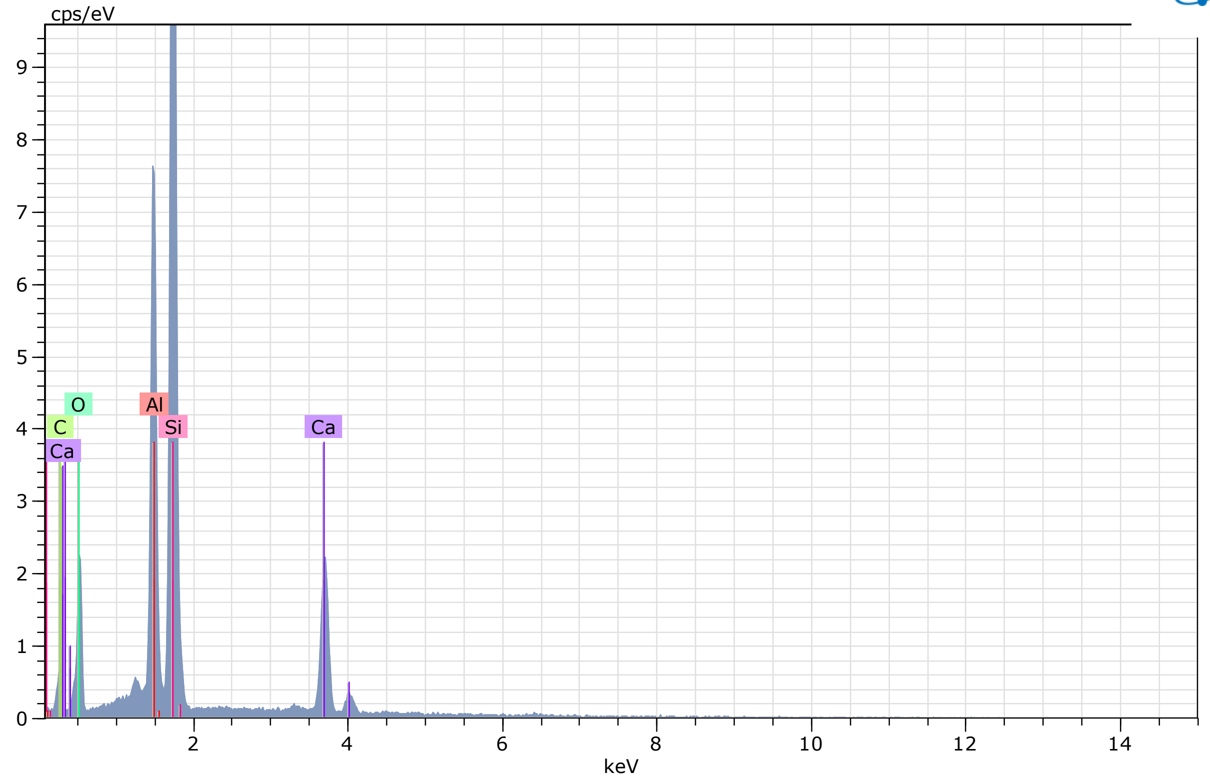

```
Spectrum:  73

El AN   Series     Net unn. C norm. C Atom. C Error (1 Sigma)
                       [wt.%]   [wt.%]   [at.%]           [wt.%]
-----------------------------------------------------------------
O   8   K-series   4068  18.46   22.48   29.85            3.03
Si  14  K-series  39801  29.99   36.53   27.63            1.29
C   6   K-series    985  11.34   13.81   24.43            2.60
Al  13  K-series  17322  11.79   14.36   11.31            0.59
Ca  20  K-series   7564  10.52   12.81    6.79            0.37
-----------------------------------------------------------------
                 Total:   82.10  100.00  100.00
```

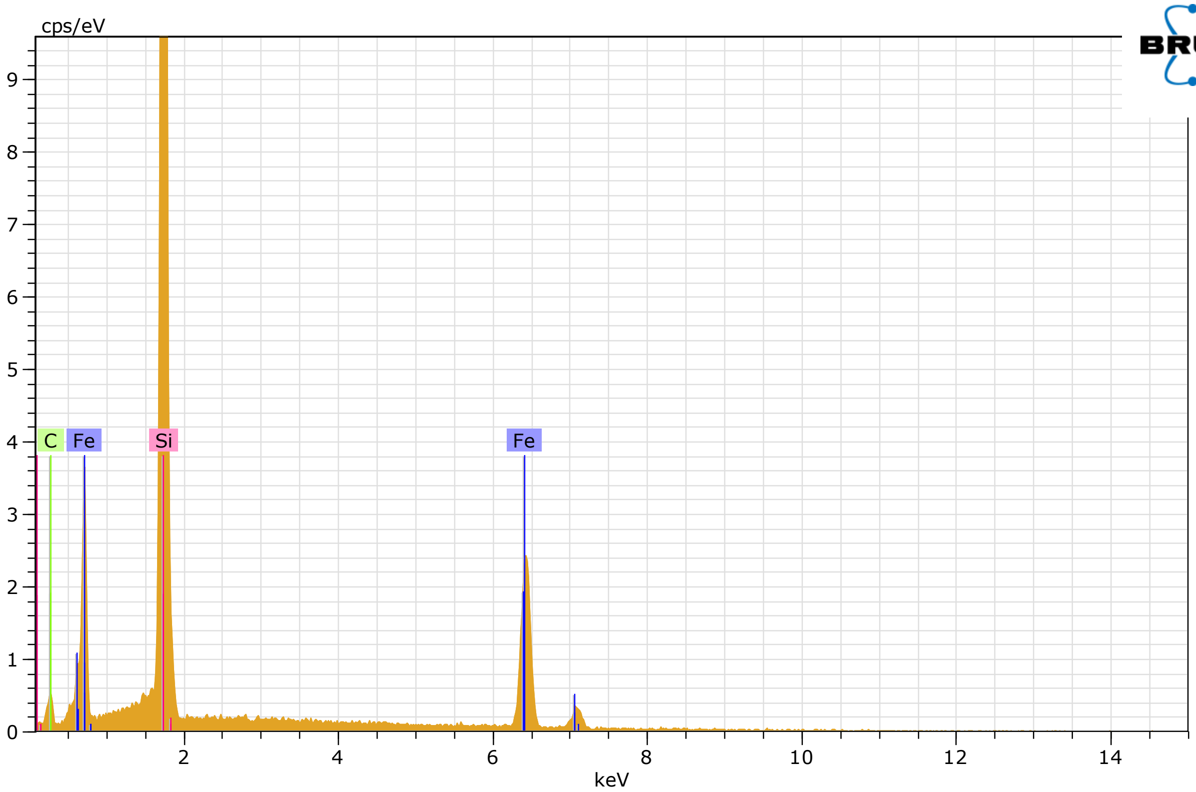

```
Spectrum:  74

El AN  Series    Net unn. C norm. C Atom. C Error (1 Sigma)
                      [wt.%]   [wt.%]   [at.%]          [wt.%]
------------------------------------------------------------
Si 14 K-series 62308  44.67    49.13    51.12            1.89
C   6  K-series   873  10.59    11.65    28.35            2.52
Fe 26 K-series 10424  35.65    39.22    20.52            1.15
------------------------------------------------------------
               Total:   90.92   100.00   100.00
```

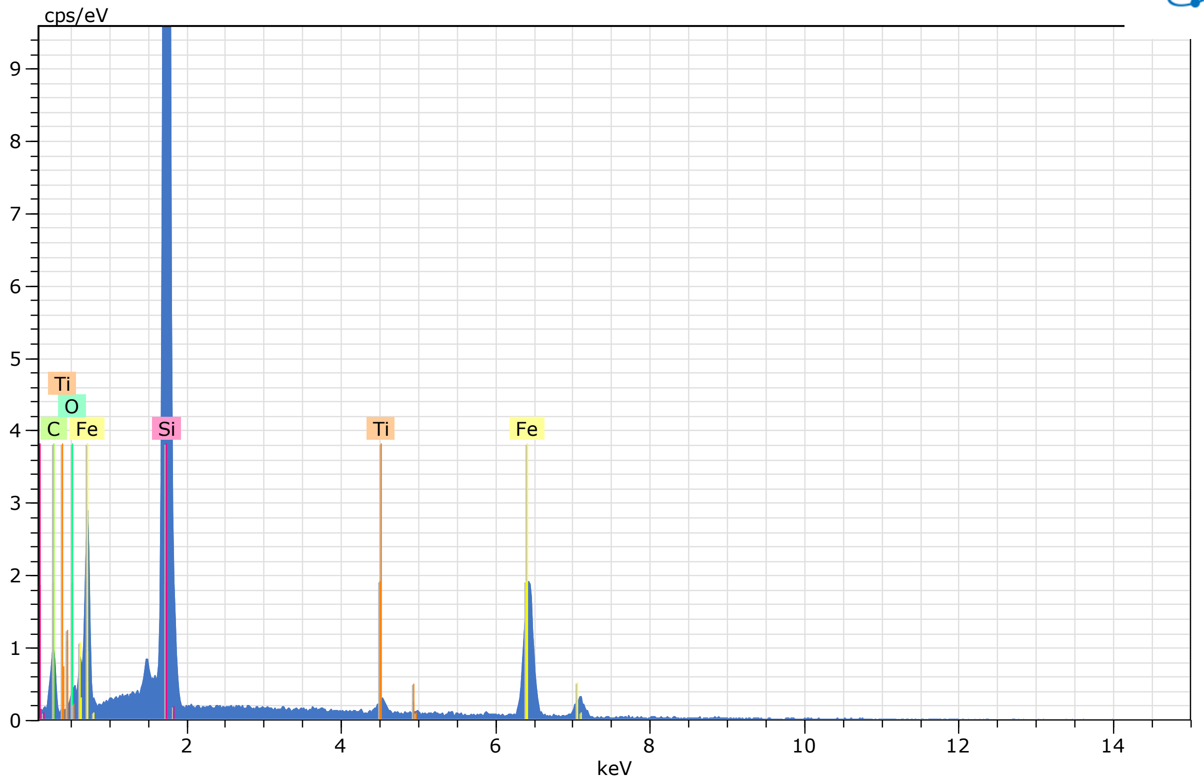

```
Spectrum:  75

El AN  Series     Net unn. C norm. C Atom. C Error (1 Sigma)
                      [wt.%]  [wt.%]  [at.%]           [wt.%]
-----------------------------------------------------------
Si 14 K-series 71008  47.06   49.39   43.63            1.99
C  6  K-series  1635  18.34   19.24   39.75            3.67
Fe 26 K-series  8205  26.65   27.97   12.43            0.88
O  8  K-series   614   2.24    2.35    3.65            0.61
Ti 22 K-series   625   1.00    1.05    0.55            0.08
-----------------------------------------------------------
               Total:  95.30  100.00  100.00
```

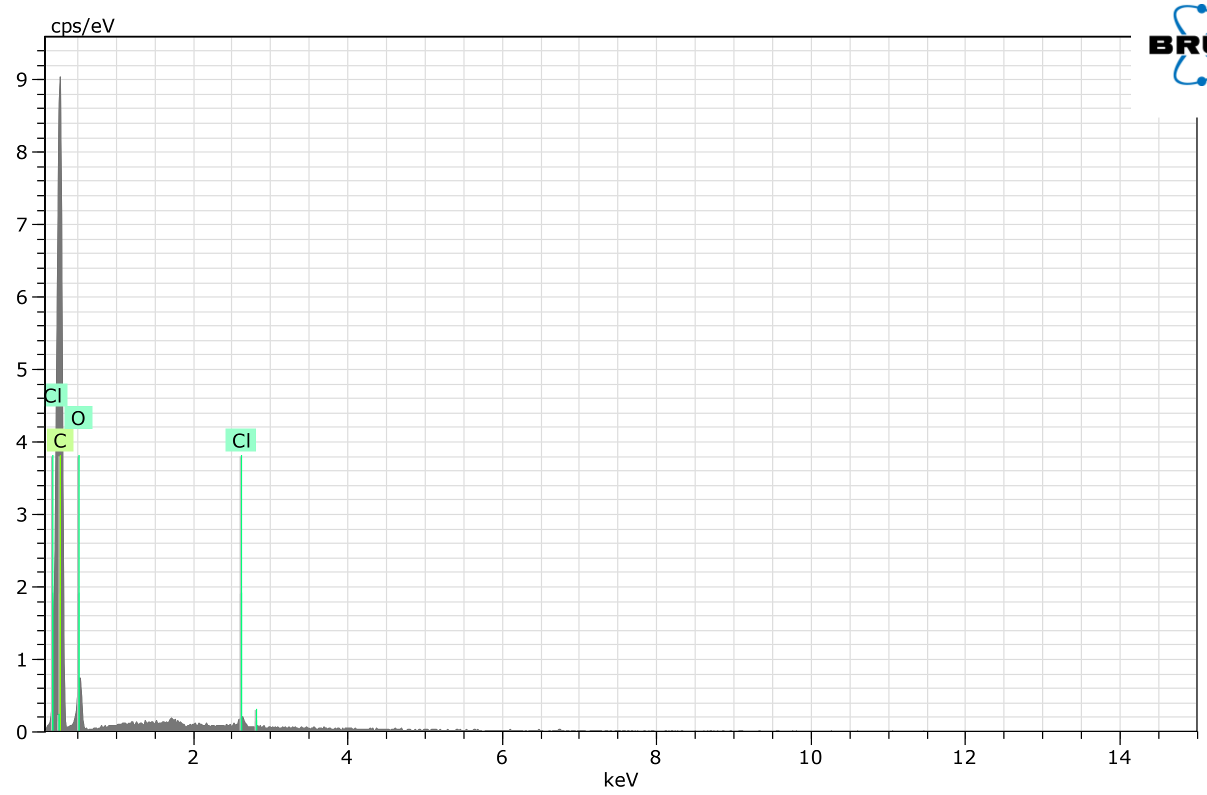

```
Spectrum:  76

El AN  Series    Net unn. C norm. C Atom. C Error (1 Sigma)
                     [wt.%]  [wt.%]  [at.%]           [wt.%]
-----------------------------------------------------------
C   6  K-series 15233  79.65   79.87   84.35           10.57
O   8  K-series  1340  19.36   19.41   15.39            4.08
Cl 17  K-series   368   0.71    0.71    0.25            0.07
-----------------------------------------------------------
               Total:  99.72  100.00  100.00
```

Slag sample 4

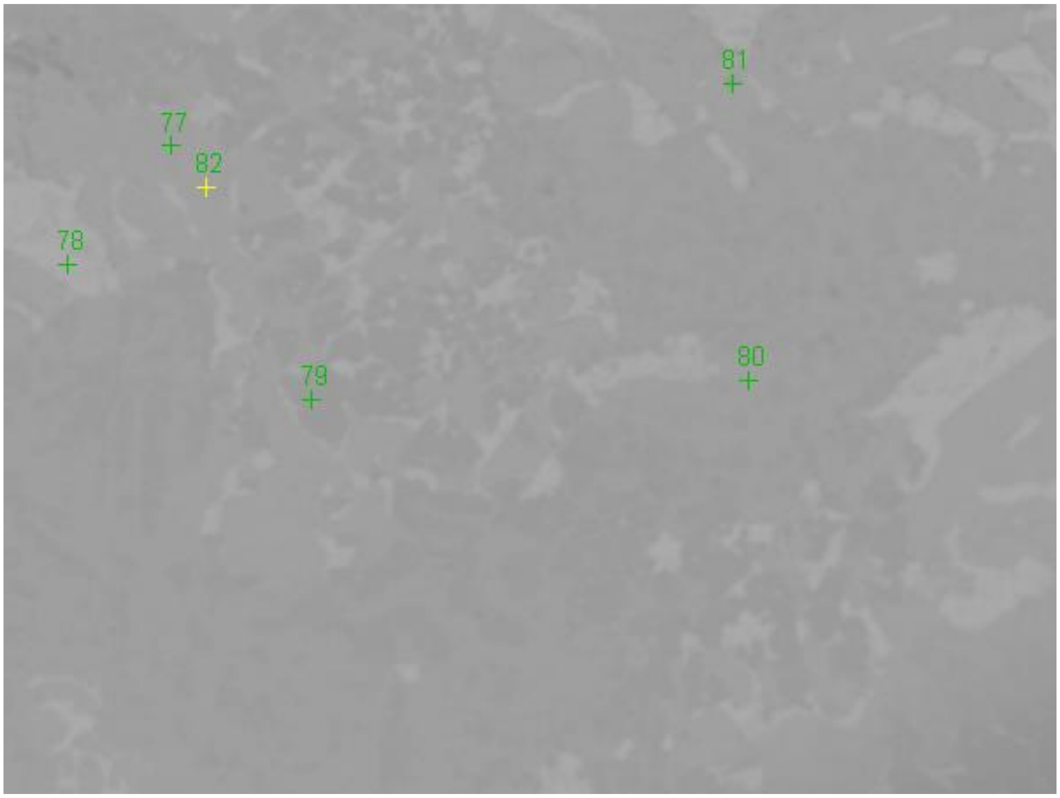

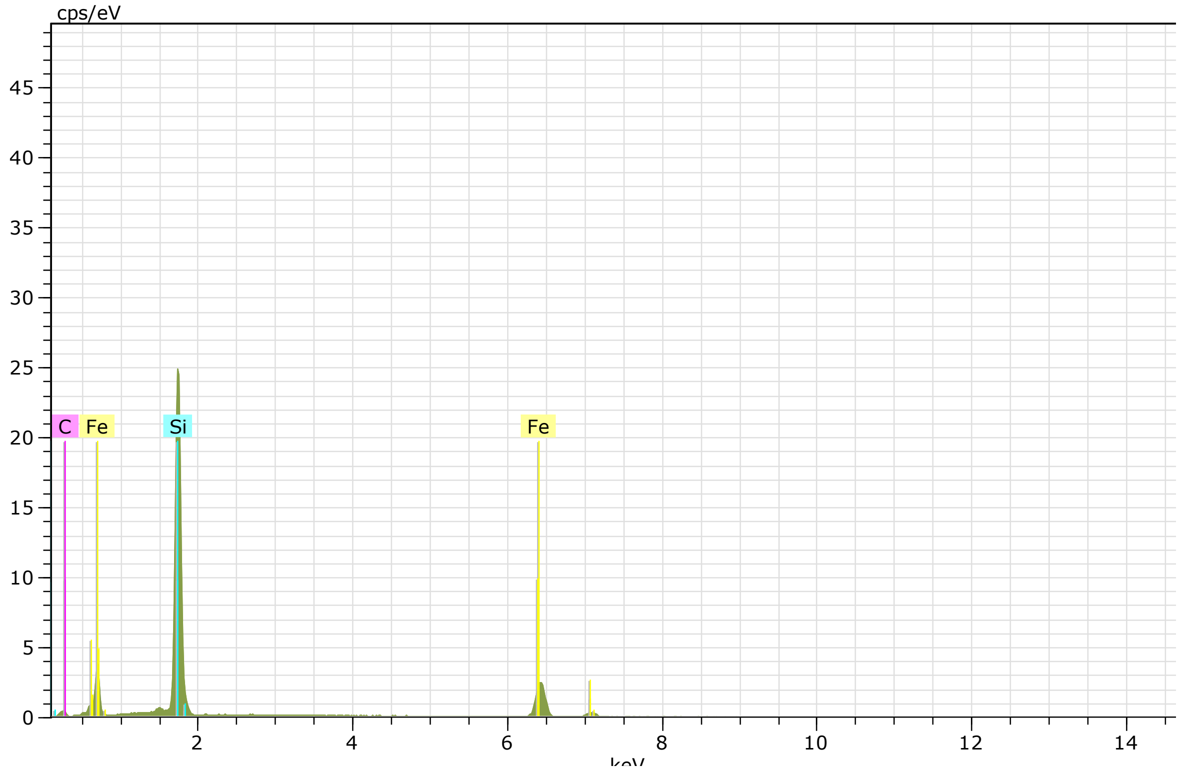

```
Spectrum:  78

El AN  Series    Net unn. C norm. C Atom. C Error (1 Sigma)
                     [wt.%]  [wt.%]  [at.%]          [wt.%]
-----------------------------------------------------------
Si 14 K-series 62879  44.66   48.75   51.08            1.89
C   6  K-series   882  10.44   11.40   27.92            2.47
Fe 26 K-series 10983  36.50   39.85   21.00            1.17
-----------------------------------------------------------
                Total:   91.60  100.00  100.00
```

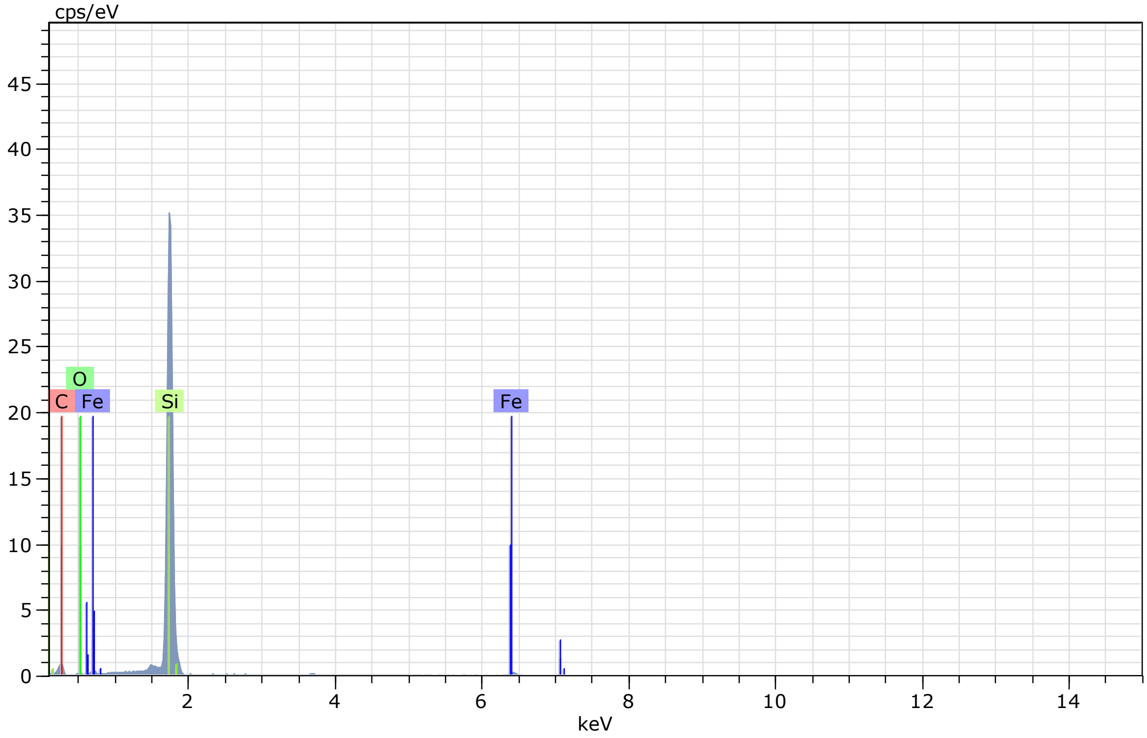

```
Spectrum:  79

El AN  Series    Net unn. C norm. C Atom. C Error (1 Sigma)
                     [wt.%]  [wt.%]  [at.%]          [wt.%]
-----------------------------------------------------------
Si 14 K-series 89106  60.11   66.94   49.29            2.53
C  6  K-series  1617  24.58   27.37   47.12            4.93
O  8  K-series   287   1.44    1.61    2.08            0.51
Fe 26 K-series   921   3.67    4.09    1.51            0.20
-----------------------------------------------------------
               Total:  89.80  100.00  100.00
```

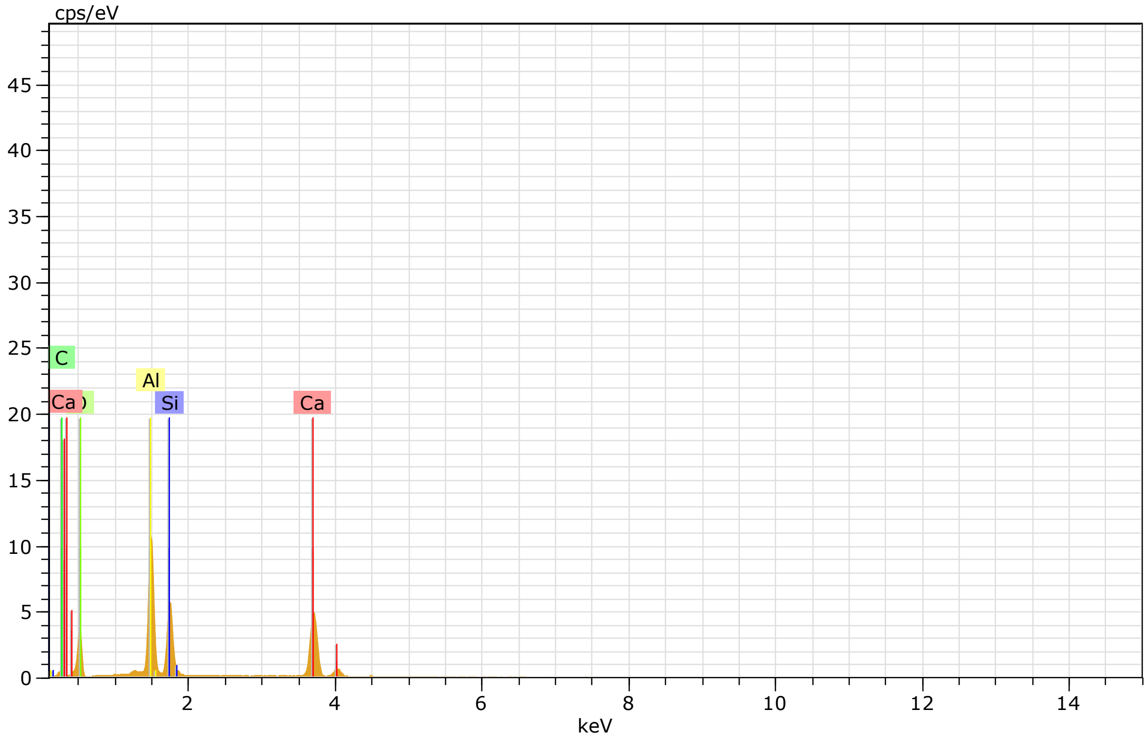

```
Spectrum:  80

El AN  Series    Net unn. C norm. C Atom. C Error (1 Sigma)
                     [wt.%]  [wt.%]  [at.%]          [wt.%]
-----------------------------------------------------------
O  8  K-series  6450  29.06   35.03   47.59            4.38
Al 13 K-series 24288  16.47   19.86   16.00            0.80
Ca 20 K-series 17267  21.03   25.35   13.75            0.68
C  6  K-series   771   5.89    7.11   12.86            1.46
Si 14 K-series 13919  10.50   12.66    9.80            0.48
-----------------------------------------------------------
               Total:  82.95  100.00  100.00
```

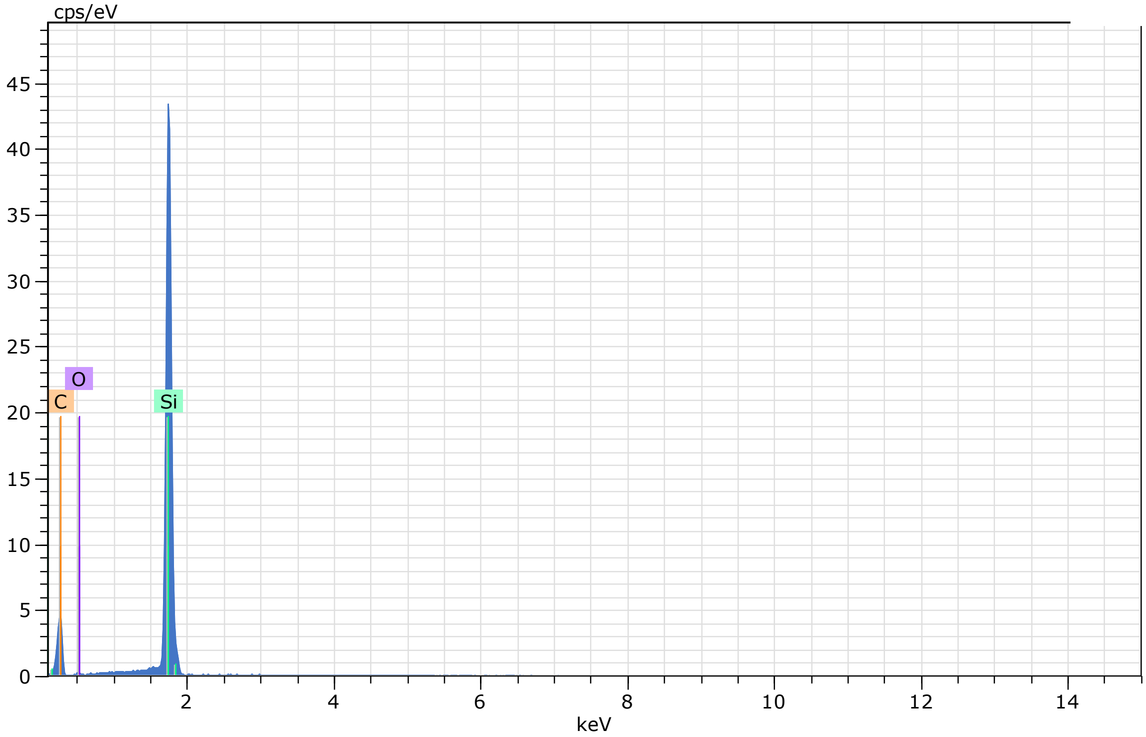

```
Spectrum:  81

El AN  Series     Net unn. C norm. C Atom. C Error (1 Sigma)
                      [wt.%]   [wt.%]   [at.%]           [wt.%]
-------------------------------------------------------------
C   6  K-series    7881  64.89   52.98   72.01             9.44
Si 14  K-series 108680  55.76   45.53   26.46             2.35
O   8  K-series     401   1.83    1.49    1.52             0.57
-------------------------------------------------------------
                Total: 122.47  100.00  100.00
```

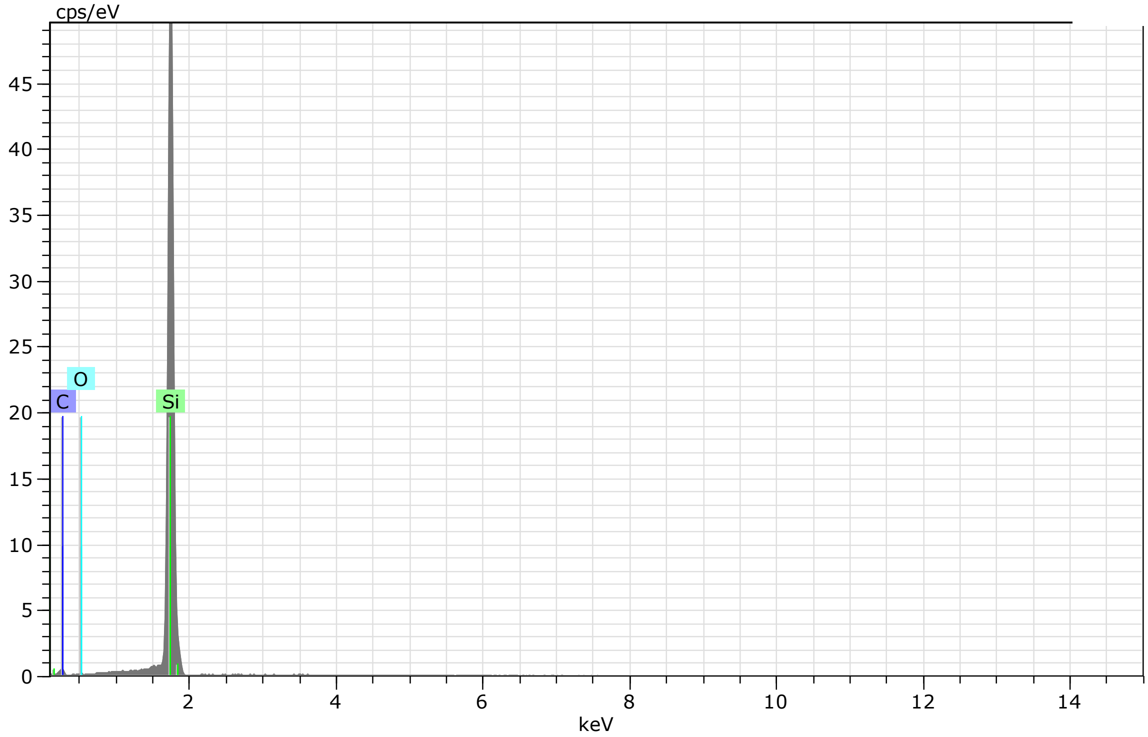

```
Spectrum:  82

El AN  Series      Net unn. C norm. C Atom. C Error (1 Sigma)
                       [wt.%]  [wt.%]  [at.%]           [wt.%]
-------------------------------------------------------------
Si 14 K-series 137960  76.66   83.58   68.96             3.22
C  6  K-series    912  13.86   15.11   29.15             3.25
O  8  K-series    298   1.20    1.31    1.89             0.42
-------------------------------------------------------------
               Total:  91.72  100.00  100.00
```

Appendix D

XRF analysis results

This chapter includes the XRF analysis done on the FeSi samples collected during the first and second campaign at Finnfjord AS.

###########
FINNFJORD AS
Results quantitative - FeSi

Selected archi FeSi
Number of re: 10

Seq.	Sample name (1-30)	Meas. date/ti	Sum	Result type	Mg	Al	Si	P	S	Ca	Ti	Cr	Mn	Fe	Ni	Cu	C
			of conc.		Mg	Al	Si	P	S	Ca	Ti	Cr	Mn	Fe	Ni	Cu	--
			(%)		(%)	(%)	(%)	(%)	(%)	(%)	(%)	(%)	(%)	(%)	(%)	(%)	(%)
1	1 180123 KL. 08.34	###########	99,971	Concentration	0,013	1,441	75,56	0,011	0,0008	0,397	0,076	0,002	0,02	22,45	0,001	0,003	0
2	2 180123 KL. 08.40	###########	100,204	Concentration	0,014	1,498	75,42	0,01	0,0009	0,413	0,077	0,001	0,019	22,75	0,001	0,003	0
3	3 180123 KL. 08.51	###########	99,391	Concentration	0,013	1,41	75,12	0,01	0,0008	0,409	0,073	0,002	0,02	22,33	0,001	0,003	0
5	2499 180123 KL. 16.40	###########	99,95	Concentration	0,01	0,971	75,8	0,01	0,0008	0,16	0,08	0,002	0,02	22,89	0,002	0,003	0
6	2499 180123 KL. 16.46	###########	99,965	Concentration	0,01	0,971	75,74	0,009	0,0007	0,166	0,081	0,002	0,02	22,96	0,001	0,003	0
7	2499 180123 KL. 16.49	###########	100,21	Concentration	0,01	1,008	76,34	0,01	0,0009	0,18	0,079	0,001	0,02	22,56	0,001	0,003	0
8	2499 180123 KL. 16.55	###########	99,947	Concentration	0,009	1,018	76,42	0,009	0,0009	0,184	0,078	0,001	0,02	22,21	0,002	0,003	0
9	2508 180124 KL. 10.11	###########	100,238	Concentration	0,01	0,981	75,62	0,01	0,0008	0,138	0,081	0,004	0,019	23,36	0,009	0,003	0
10	2509 180124 KL. 12.02	###########	100,457	Concentration	0,01	1,188	75,2	0,011	0,0009	0,228	0,082	0,003	0,02	23,71	0,008	0,003	0
				Mean Concen	0,011	1,169	75,723	0,01	0,001	0,25	0,079	0,002	0,021	22,749	0,003	0,003	0
				Min. Concentr	0,009	0,971	75,12	0,009	0,001	0,138	0,073	0,001	0,019	22,205	0,001	0,003	0
				Max. Concent	0,014	1,498	76,417	0,012	0,001	0,413	0,084	0,004	0,034	23,705	0,009	0,008	0
				RMS Concentr	0,0017	0,2119	0,4367	0,0007	0,0002	0,1114	0,0031	0,0011	0,0045	0,4899	0,0031	0,0016	0
				RMS rel. Conc	15,546	18,122	0,577	7,372	24,722	44,528	3,944	47,962	21,066	2,153	99,841	45,614	
				Used Concent	10	10	10	10	10	10	10	10	10	10	10	10	10

###########
FINNFJORD AS
Results quantitative - FeSi

Selected archi FeSi
Number of re: 12

Seq.	Sample name (1-30)	Meas. date/ti	Sum	Result type	Mg	Al	Si	P	S	Ca	Ti	Cr	Mn	Fe	Ni	Cu	C
			of conc.		Mg	Al	Si	P	S	Ca	Ti	Cr	Mn	Fe	Ni	Cu	--
			(%)		(%)	(%)	(%)	(%)	(%)	(%)	(%)	(%)	(%)	(%)	(%)	(%)	(%)
1	FS 1 180122 KL.14.38	###########	99,973	Concentration	0,013	1,227	75,73	0,01	0,0007	0,198	0,083	0,004	0,019	22,68	0,002	0,003	0
2	FS 2 180122 KL.14.42	###########	99,677	Concentration	0,013	1,223	75,82	0,011	0,0012	0,202	0,083	0,002	0,019	22,3	0,002	0,003	0
3	FS 3 180122 KL.14.48	###########	100,334	Concentration	0,012	1,238	75,91	0,01	0,0032	0,215	0,084	0,002	0,019	22,83	0,002	0,003	0
4	FS 4 180122 KL.14.51	###########	99,869	Concentration	0,012	1,242	75,58	0,01	0,0008	0,225	0,083	0,002	0,019	22,69	0,002	0,003	0
5	FS 5 180122 KL.14.58	###########	99,894	Concentration	0,012	1,228	75,67	0,01	0,004	0,197	0,084	0,003	0,019	22,66	0,005	0,003	0
6	FS 6 180122 KL.15.22	###########	100,114	Concentration	0,012	1,369	75,63	0,01	0,0013	0,215	0,081	0,003	0,019	22,76	0,006	0,003	0
7	1 180122 KL. 1300	###########	100,087	Concentration	0,013	1,241	75,78	0,01	0,0008	0,194	0,085	0,002	0,018	22,74	0,002	0,003	0
8	1 180122 KL. 17.14	###########	99,988	Concentration	0,012	1,392	75,23	0,01	0,0008	0,26	0,082	0,001	0,02	22,98	0,001	0,003	0
9	2 180122 KL. 17.19	###########	99,853	Concentration	0,012	1,406	75,01	0,01	0,0009	0,262	0,083	0,002	0,02	23,05	0,002	0,003	0
10	3 180122 KL. 17.24	###########	100,179	Concentration	0,012	1,414	75,25	0,01	0,0007	0,264	0,083	0,002	0,019	23,12	0,001	0,003	0
11	4 180122 KL. 17.30	###########	100,151	Concentration	0,012	1,41	75,2	0,01	0,0009	0,27	0,082	0,003	0,02	23,13	0,01	0,003	0
12	5 180122 KL. 17.40	###########	100,749	Concentration	0,012	1,473	75,13	0,01	0,0007	0,252	0,081	0,003	0,02	23,76	0,007	0,003	0
				Mean Concen	0,012	1,322	75,494	0,01	0,001	0,229	0,083	0,002	0,019	22,892	0,003	0,003	0
				Min. Concentr	0,012	1,223	75,005	0,01	0,001	0,194	0,081	0,001	0,018	22,3	0,001	0,003	0
				Max. Concent	0,013	1,473	75,914	0,011	0,004	0,27	0,085	0,004	0,02	23,762	0,01	0,003	0

RMS Concentr	0,0003	0,0958	0,3118	0,0005	0,0011	0,0299	0,0012	0,0007	0,0004	0,3608	0,0028	0,0002	0
RMS rel. Conc	2,171	7,244	0,413	4,868	81,444	13,047	1,477	29,989	2,312	1,576	83,584	7,78	
Used Concent	12	12	12	12	12	12	12	12	12	12	12	12	12

###########
FINNFJORD AS
Results quantitative - FeSi

Selected archi FeSi
Number of res 13

Seq.	Sample name (1-30)	Meas. date/ti	Sum	Result type	Mg	Al	Si	P	S	Ca	Ti	Cr	Mn	Fe	Ni	Cu	C
			of conc.		Mg	Al	Si	P	S	Ca	Ti	Cr	Mn	Fe	Ni	Cu	--
			(%)		(%)	(%)	(%)	(%)	(%)	(%)	(%)	(%)	(%)	(%)	(%)	(%)	(%)
1	2498 180123 KL. 14.37	###########	99,655	Concentratior	0,011	1,031	75,96	0,01	0,0007	0,225	0,075	0,002	0,019	22,32	0,001	0,003	0
2	2498 180123 KL. 14.42	###########	99,838	Concentratior	0,01	0,961	76,01	0,009	0,0007	0,179	0,076	0,001	0,019	22,56	0,001	0,003	0
3	2498 180123 KL. 14.45	###########	99,467	Concentratior	0,009	0,987	75,4	0,01	0,0008	0,181	0,079	0,002	0,02	22,77	0,001	0,003	0
4	2496 180123 KL. 10.36	###########	99,831	Concentratior	0,012	1,385	75,67	0,01	0,0007	0,386	0,072	0,001	0,02	22,27	0,001	0,003	0
5	2496 180123 KL. 10.44	###########	100,162	Concentratior	0,013	1,415	75,91	0,01	0,0006	0,397	0,072	0,003	0,019	22,31	0,008	0,003	0
6	2496 180123 KL. 10.55	###########	100,735	Concentratior	0,013	1,438	76,23	0,011	0,0008	0,407	0,076	0,002	0,019	22,53	0,008	0,003	0
7	2497 180123 KL. 12.38	###########	99,598	Concentratior	0,011	1,219	75,66	0,01	0,0014	0,295	0,076	0,002	0,02	22,3	0,002	0,003	0
8	2497 180123 KL. 12.43	###########	99,525	Concentratior	0,012	1,217	75,76	0,01	0,0008	0,296	0,077	0,002	0,02	22,13	0,001	0,003	0
9	2497 180123 KL. 12.46	###########	99,758	Concentratior	0,011	1,173	75,88	0,01	0,001	0,266	0,077	0,002	0,02	22,32	0,001	0,003	0
10	2497 180123 KL. 12.49	###########	99,901	Concentratior	0,011	1,167	76,12	0,01	0,0008	0,268	0,076	0,002	0,02	22,23	0,001	0,003	0
11	2497 180123 KL. 12.57	###########	99,935	Concentratior	0,011	1,225	76,06	0,01	0,0007	0,27	0,079	0,004	0,022	22,24	0,008	0,003	0
12	2510 180124 KL. 14.02	###########	99,905	Concentratior	0,01	1,015	74,27	0,01	0,0007	0,188	0,088	0,003	0,02	24,29	0,007	0,003	0
13	2511 180124 KL. 15.58	###########	100,824	Concentratior	0,01	0,922	75,21	0,011	0,0007	0,162	0,088	0,006	0,022	24,38	0,002	0,003	0

###########
FINNFJORD AS
Results quantitative - FeSi

Selected archi FeSi
Number of res 14

Seq.	Sample name (1-30)	Meas. date/ti	Sum	Result type	Mg	Al	Si	P	S	Ca	Ti	Cr	Mn	Fe	Ni	Cu	C
			of conc.		Mg	Al	Si	P	S	Ca	Ti	Cr	Mn	Fe	Ni	Cu	--
			(%)		(%)	(%)	(%)	(%)	(%)	(%)	(%)	(%)	(%)	(%)	(%)	(%)	(%)
1	3112 19.03 KL. 1347	###########	99,575	Concentratior	0,011	0,805	76,01	0,01	0,0008	0,178	0,068	0,001	0,021	22,47	0,001	0,003	0
2	3112 19.03 KL. 1353	###########	99,649	Concentratior	0,012	0,902	75,9	0,01	0,0006	0,267	0,066	0,002	0,021	22,46	0,001	0,002	0
3	3112 19.03 KL. 1400	###########	99,573	Concentratior	0,012	0,721	75,85	0,01	0,0006	0,127	0,069	0,001	0,023	22,75	0,001	0,003	0
4	3113 19.03 KL. 1603	###########	100,039	Concentratior	0,012	0,858	76,31	0,01	0,0006	0,158	0,067	0,001	0,021	22,59	0,001	0,003	0
5	3124 20.03 KL. 1241	###########	100,15	Concentratior	0,012	1,135	74,4	0,011	0,0006	0,272	0,069	0,003	0,021	24,21	0,008	0,003	0
6	3125 20.03 KL. 1423	###########	100,323	Concentratior	0,011	0,996	74,79	0,01	0,0006	0,219	0,069	0,003	0,023	24,19	0,008	0,003	0
7	3126 20.03 KL. 1615	###########	100,098	Concentratior	0,011	0,848	75,53	0,01	0,0007	0,155	0,07	0,002	0,022	23,45	0,002	0,004	0
8	3126 20.03 KL. 1621	###########	99,827	Concentratior	0,011	0,807	75,47	0,01	0,0006	0,151	0,071	0,001	0,021	23,28	0,001	0,004	0
9	3135 21.03 KL. 1223	###########	99,793	Concentratior	0,012	0,991	74,84	0,01	0,0006	0,228	0,071	0,001	0,021	23,61	0,001	0,003	0
10	3135 21.03 KL. 1230	###########	100,144	Concentratior	0,012	1,013	74,99	0,011	0,0006	0,214	0,07	0,002	0,021	23,81	0,001	0,003	0

11	3136 21.03 KL. 1429	###########	100,394	Concentratior	0,013	1,14	75,17	0,011	0,0006	0,308	0,069	0,004	0,02	23,65	0,009	0,004	0
12	3136 21.03 KL.1444	###########	99,833	Concentratior	0,012	1,119	74,87	0,011	0,0006	0,29	0,07	0,002	0,021	23,43	0,005	0,004	0
13	3137 21.03 KL. 1703	###########	100,847	Concentratior	0,013	1,202	75,74	0,011	0,0006	0,325	0,07	0,001	0,021	23,46	0,001	0,003	0
14	3137 21.03 KL. 1717	###########	100,768	Concentratior	0,013	1,204	75,79	0,011	0,0006	0,349	0,068	0,001	0,021	23,31	0,001	0,002	0